



**Politecnico
di Torino**

Politecnico di Torino

Master's Degree in Mechatronic Engineering

A.y. 2021/2022

Graduation Session October 2022

E-Drives Modeling and Torque Control for Electrical Vehicles

Supervisors:

Prof. Radu Bojoi

Dr. Luisa Tolosano

Candidate:

Alessandro Ionta

Contents

List of Tables	4
List of Figures	5
1 Introduction	10
1.1 State of Art in E-mobility	10
1.1.1 Parallel hybrid powertrains	11
1.1.2 Power-split powertrains	12
1.1.3 Two-mode hybrid powertrains	13
1.1.4 Series-parallel hybrid powertrains	14
1.1.5 Plug-in hybrid electric vehicles	15
1.1.6 EREV powertrains	16
1.1.7 EV powertrains	17
1.1.8 Powertrain comparisons	17
2 Elements Structure for Electric Vehicles	20
2.1 DC power source	20
2.1.1 Battery	21
2.2 Power Electronic Converter	21
2.2.1 IGBT	23
2.2.2 Two-level converter	24
2.2.3 Inverter Non-Linear Effects	25
2.2.4 Simulation of dead-time	27
2.3 e-Motors	28
3 E-Motor Modeling	34
3.1 Dynamic model in dq frame	34
3.1.1 Voltage Equation	35
3.1.2 Flux Linkage Equation	35
3.1.3 Torque Equation	36
3.1.4 Flux Maps	37
3.2 Non-circuital, inverse maps model	39
3.3 Voltage Behind Reactance model	40
3.3.1 Simscape Component	43
3.3.2 Block selection and evaluation	46
4 Torque Control Strategies for E-motors	47
4.1 DTC	48
4.1.1 Control of Stator Flux Linkage by Selecting the Proper Stator Voltage Vector	48
4.1.2 Flux-Weakening Algorithm	50
4.1.3 Modified Direct Torque Control	52
4.2 FOC	53
4.2.1 Look-Up Table Computation	53
4.2.2 Torque Control Strategies based on LUTs	56

4.2.3	Feed-Forward based Field Weakening for Fast Dynamics	60
4.2.4	Model Reference Adaptive Control	61
4.3	DFVC	63
4.3.1	Modeling of the AC Machines	64
4.3.2	Direct Flux Vector Control implementation	66
4.4	Fault Tolerance	68
4.4.1	Sensorless Torque-Control	68
4.4.2	Open-Phase Fault-Tolerant Control	70
4.4.3	Intern-Turn Fault Tolerant Control	73
4.5	Control techniques evaluation	75
4.6	4D FOC	76
4.6.1	Input signal management	76
4.6.2	Current set point generation	78
4.6.3	Control Maps	78
4.6.4	PI Controllers	84
4.6.5	Voltage reference and duty cycle computation	85
5	Simulation Results	87
5.1	VBR Model Validation	87
5.2	4D FOC validation	89
5.2.1	Control Algorithm	89
5.2.2	Input Signals Elaborations	90
5.2.3	4D FOC Control: control blocks implemented in the state GO_MOTOR	91
5.3	Matlab-Simulink simulation	94
5.3.1	Maximum Torque per Speed (MTPS)	94
5.3.2	Stress Test	97
5.3.3	Accuracy Test	98
5.4	4D FOC vs DFVC	99
5.4.1	MTPS	99
5.4.2	Stress Test	100
5.4.3	Accuracy Test	102
5.5	Fault Tolerance Analysis	102
5.5.1	Currents unbalance	102
5.5.2	Open gate Fault	104
6	Conclusion	106
7	Bibliography	107
A	C-Functions	110
A.1	Interpolation of 2D LUT	110
A.2	Phase Locked Loop	112

List of Tables

4.1	PI controllers calibration	84
5.1	Motor and Inverter parameters.	94

List of Figures

1.1	Parallel architecture block diagrams: (a)ISG/BSG parallel configuration (P1) (b)pre-trasmission parallel configuration (P2) (c)post-trasmission parallel configuration (P3) (d)parallel-through-the road configuration (P4)[22]. . .	11
1.2	(a)Toyota hybrid system (b)block diagram representation[22].	12
1.3	HSD system (a)2010 Toyota Prius Hybrid synergy drive (b)block diagram representation[22].	12
1.4	Variations of power-split systems (a)block diagram representation of the AWD drive system (b)block diagram representation of the HSD using Ravigneaux gear[22].	13
1.5	Two-mode hybrid transmission and its block diagram (a)GM two-mode Allison hybrid transmission (b)AHS block diagram[22].	13
1.6	Series-parallel hybrid powertrain configurations (a)Hyundai Sonata Hybrid (b)Honda Accord Hybrid[22].	15
1.7	Voltec 4ET50 multi-mode electric transaxle configuration[22].	16
1.8	EV powertrain configuration[22].	17
1.9	Comparison for various powertrain configurations based on vehicle classes[22].	18
1.10	Powertrain comparisons in terms of fuel economy and complexity[22]. . .	18
2.1	Elements Structure for Electric Vehicles[25].	20
2.2	Simulink symbol for the Controlled Voltage Source block.	21
2.3	Scheme of a two level three-phase inverter.	22
2.4	Comparison between the triangular carrier and duty cycle.	22
2.5	Simulink: Simscape→Electrical symbol for the IGBT block.	23
2.6	Current-Voltage curves of the IGBT[26].	23
2.7	Simscape→ Specialized Power Systems symbol for the Two-level converter block.	24
2.8	Current of phase a ($ma=0.5$).	25
2.9	Effect of dead-time[21].	26
2.10	Effect of dead-time on the sinusoidal waveform of the instantaneous average output voltage[21].	26
2.11	Duty cycles elaborated with DeltaD method ($ma=1$).	27
2.12	Phase voltage V_a ($ma=1$).	28
2.13	Rotating magnetic field explanation[25].	29
2.14	Induction motor types[25].	29
2.15	Synchronous motor types[25].	30
2.16	SPM synchronous motor[25].	30
2.17	SyR synchronous motor[25].	31
2.18	IPM synchronous motor[25].	31
2.19	Summary motor types and characteristics[25].	33
3.1	Example of (dq) rotor and $(d_s q_s)$ stator flux-linkage reference frames. . . .	34
3.2	Application of "PM-style" convention for synchronous motors[9].	35
3.3	Flux-linkage maps of IPM motor used in the simulations.	37
3.4	Flux-linkage profiles of the IPM motor used in the simulations.	38

3.5	Indirect flux maps of IPM motor used in the simulations.	39
3.6	E-Drive Simulink non circuital, discrete-time average model.	39
3.7	Equivalent circuit for the electric machine with the VBR model.	43
3.8	Simulink symbol for the Simscape component block.	43
3.9	Simulink symbol for the personalised Simscape component block.	45
3.10	Current of phase a in the motor test.	46
3.11	Detail of current of phase a in the motor test.	46
4.1	Powertrain scheme.	47
4.2	Control of the stator flux linkage[1].	49
4.3	Torque responses with DTC and current control: (a) torque response under DTC and (b) torque response under PWM current control in the rotor reference frame[1].	50
4.4	DTC scheme with flux weakening[2].	51
4.5	Tuning of the flux-weakening algorithm during the first transient. Speed variation from 75% up to 400% of the base speed. (a) Maximum torque. (b) Torque reference. (c) Flux reference. (d) Motor current[2].	52
4.6	Block diagram of the DTC-AAS drive system[3].	52
4.7	Estimated torque response and stator flux amplitude when step load torque change from no-load to full load (0-2.6Nm)[3].	53
4.8	Plug-and-Play start up method[4].	54
4.9	MTPA, MTPV, and current limit control trajectories: (a) $i_d - i_q$ plane (b) $\varphi_d - \varphi_q$ plane. The dashed lines show the results when the magnetic saturation is not taken into account (inductances correspond to the rated operating point). the black dashed curve corresponds to the constant current circle[4].	56
4.10	Torque vs speed curve generated from the reference calculation block with and without taking magnetic saturation into account[4].	56
4.11	IPMSM optimal control trajectories and regions[5].	58
4.12	LUT based current reference determination using the speed normalization concept and proposed VCT feedback strategies[5].	59
4.13	Proposed hybrid IPMSM control strategies simulation results[5].	60
4.14	Control block diagram of proposed field weakening control[6].	61
4.15	Structure of the proposed adaptive MRAC torque controller[7].	62
4.16	A comparison of dynamic results with parameter error[7].	63
4.17	Definition of reference frames for AC machines[9].	64
4.18	UDFVC control scheme[9].	66
4.19	Speed Reversal results[9].	68
4.20	Block diagram of sensorless torque control scheme based on FOC technique used in EV applications[10].	69
4.21	Experimental results for sensorless performance with 50% increase in the stator resistance and applied torque command of 10 Nm. (a) Conventional Back-EMF MRAS (b) Robust Back-EMF MRAS[10].	70
4.22	Simplified description of the system[11].	71
4.23	System with failure with fault detection and tolerance. (a) Waveform of the EMF (b) Measured currents (c) Electromagnetic torque (d) DC-link voltage (blue) and bottom capacitor voltage (orange)[11].	73
4.24	Proposed strategy for PMSM[12].	74
4.25	Fault tolerant control results[12].	75
4.26	4D FOC block scheme[5].	76
4.27	PLL scheme.	77
4.28	4D FOC block scheme part 1[5].	78
4.29	Current map computation: selection of the working quadrant.	80
4.30	Current map computation: application of the current limit.	80
4.31	Current map computation: application of the MTPA limit.	81
4.32	Current map computation: application of the MTPV limit.	81

4.33	Currents Non-normalized current Maps of IPM.	82
4.34	Currents Control Maps of IPM - Speed and Torque Normalization.	83
4.35	4D FOC block scheme part 2[5].	84
4.36	4D FOC block scheme part 3[5].	85
4.37	Min-Max modulation.	86
5.1	VBR model in Matlab/Simulink and PLECS environment.	87
5.2	Torque response of the bechmark model and VBR model in Simulink and PLECS.	88
5.3	Implemented state machine.	89
5.4	MTPS in motoring operation at rated parameters, $V_{dc} = 400V$ $T_s = 25^\circ C$	95
5.5	MTPS in generator operation at rated parameters, $V_{dc} = 400V$ $T_s = 25^\circ C$	96
5.6	MTPS power evaluation for different DC-link voltages.	96
5.7	MTPS evaluation for different DC-link voltages and different temperature of the magnets.	97
5.8	Square wave reference test at rated parameters, $V_{dc} = 400V$ $T_s = 25^\circ C$	98
5.9	Torque accuracy test, $V_{dc} = 400V$, $T_s = 25^\circ C$, 2000 rpm.	99
5.10	MTPS in motoring operation at rated parameters, $V_{dc} = 400V$ $T_s = 25^\circ C$	100
5.11	MTPS comparison in motoring operation at temperatures different from the room one.	100
5.12	Square wave reference test comparison at rated parameters, $V_{dc} = 400V$ $T_s = 25^\circ C$	101
5.13	Square wave torque reference test 4D FOC vs DFVC.	101
5.14	Torque accuracy test comparison, $V_{dc} = 400V$, $T_s = 25^\circ C$, 2000 rpm.	102
5.15	Currents unbalance simulation results.	103
5.16	Currents unbalance simulation results.	104
5.17	Open gate fault simulation results.	105
5.18	Gate signal behaviour.	105

Summary

In the automobile industry, new technologies are becoming available with a strong chance of taking over as the standard design in the future. These systems rely on an electric traction system that can work in tandem with a traditional internal combustion engine or not. Nevertheless, as e-mobility is a young technology, there is still space for progress. In a world where the development of electric cars is constantly expanding, tactics for controlling the torque of electric machines have grown to be of the utmost importance. The basic objective of all implementable control techniques is to ensure that the machine's torque regulation is maintained under all conceivable operating situations. For these reasons this thesis concerns unified torque control techniques of traction motors for electric vehicles. The thesis is carried out in the context of a research collaboration between the PEIC interdepartmental center of the Politecnico di Torino and the Punch Torino company.

The first goal is to create an accurate simulation of the electric traction of a pure electric car or hybrid electric vehicle. This electric propulsion is made up of standard components such a converter, storage system, and electrical machine. A battery is first selected as the storage system. A three-phase inverter, specifically a two-level inverter, is the converter that was chosen. The high performance Internal Permanent Magnet (IPM) motor used in the electric machine allows it to operate very close to its limitations. Simulink has been used as the simulation environment, and each component has been simulated using either pre-existing blocks or newly constructed ones. The system generated in the simulation environments is tested in comparison to a model developed in another simulation tool (PLECS), highlighting its validity. The goal of the thesis is to set up a new circuitual model of the e-Drive, valid for instantaneous simulation, and also able to consider fault conditions. The modelling approach considered for the e-Motor is the Voltage Behind Reactance (VBR) model. It represents the motor as an RLE load, with coupled inductors and controlled voltage generators imposing the back EMF voltages computed by the motor model.

The second aim of the thesis is to analyse the control method for the electric motor and generate it in the specific programming language. The Field Oriented Control (FOC) solution has been developed for the IPM motor and it is based on multiple Look-up Tables (LUTs). In this approach, the optimal current setpoints are calculated from the operating conditions of the machine and data stored in precalculated LUTs. The developed 4D LUTs FOC has been compared with an existing Direct Flux Vector Control (DFVC) solution used as benchmark. Using the VBR model developed a control comparison between 4D FOC and DFVC is done. The result obtained attest that The 4D FOC represents also a valid control solution for the efficient control of the e-Drive taken into account. Also peculiar characteristic are shown like the capability to overcome the issues due to machine electric parameters variation with temperature. The greatest drawback resides in the difficulties in the elaboration of the 4D LUTs. Nevertheless LUTs computation is an offline operation that guarantees a fast and efficient online response of the control.

The whole system developed with the powertrain circuitual model and the control represents a valid simulation environment and also a strong base for future development in the optic of Fault Tolerance thanks to the circuitual characteristics of the e-Motor model generated. Also the 4D FOC control scheme developed due to its simplicity, flexibility

and reliability can be the starting point in this field.

Chapter 1

Introduction

A revolutionary vehicle design has recently reached the market, holding forth the enormous potential of revolutionizing the world of mobility. This novel design is based on the electric traction system, which either serves as the only traction system in electric vehicles (EV) or as a complement to the conventional combustion engine in hybrid electric vehicles (HEV). Over the past few years, e-Mobility, or electric mobility, has steadily increased. The requirement of lowering pollutant emissions, driven by new rules at the European and International level, is another reason why these new technologies are growing in importance. Many automakers have made a significant effort to invest in these technologies. Clearly, electric vehicles are the way of the future in the automotive industry. Nevertheless, as e-mobility is a young technology, there is still space for progress. The prevailing design has not yet been released, and there is a raging standard war going on. In order to identify the best answer in this dynamic competition, new features and components are constantly being added.

In a world where the development of electric cars is constantly expanding, tactics for controlling the torque of electric machines have grown to be of the utmost importance. In reality, this kind of application calls for electrical drives that can effectively utilize the machine's torque capacity to achieve the optimum performance. The basic objective of all implementable control techniques is to ensure that the machine's torque regulation is maintained under all conceivable operating situations. It is easy to comprehend the operating points in depth by being aware of the maximum motor speed as well as the voltage and current restrictions. Because of this, a torque control system should be able to manage the machine's torque over its whole working range without excluding any possible operating points. In this case, having a torque control system that can be used with any kind of electric motor is a wise move, even for high-performance industrial applications.

For these reasons this thesis concerns unified torque control techniques of traction motors for electric vehicles. The thesis is carried out in the context of a research collaboration between the PEIC interdepartmental center of the Politecnico di Torino and the Punch Torino company.

1.1 State of Art in E-mobility

The center of modern transportation technology has shifted to automotive electrification, particularly in an era of growing gas prices and public concern over car pollution. Subcompact cars to heavy-duty trucks and buses have all been equipped with a variety of electrified powertrains, ranging from micro hybrid to fully electric. Following the research taken in [22] an overview of this world is done.

1.1.1 Parallel hybrid powertrains

For many manufacturers the parallel hybrid architecture has been the powertrain of choice for their first step into vehicle electrification. The parallel architecture consists of an electric machine placed in line with the Internal Combustion Engine (ICE). It is referred as a parallel configuration because the power is added up from both the ICE and the electric machine to the transmission independent of each other. Depending on the relative position of the electric machine and the engine, parallel hybrid powertrains can be categorised into four configurations, which are typically as P1 to P4, shown in Figure 1.1

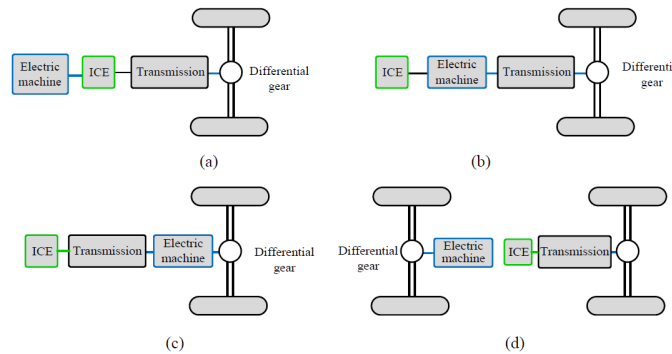


Figure 1.1: Parallel architecture block diagrams: (a)ISG/BSG parallel configuration (P1) (b)pre-transmission parallel configuration (P2) (c)post-transmission parallel configuration (P3) (d)parallel-through-the road configuration (P4)[22].

The electric machine is located before the engine in P1 configuration. The Integrated Starter Generator (ISG) or Belt Starter Generator (BSG) replaces the alternator and starter motors connected to the ICE with a single electric machine. This machine performs the task of both of these devices, acting as a starter motor for the engine and generator for powering vehicle accessories. It also allows engine to shut off when the vehicle is stopped, preventing idling and saving fuel. In addition, it can be used for limited regenerative braking during vehicle deceleration and power assistance during acceleration. This architecture is extensively used in hybrid vehicles that have relatively lower level of electrification and can be found across a broad range of vehicle classes from compact vehicles to large trucks.

In the P2 design, an electric machine is placed before the transmission. Depending on the size and capacity of the battery pack, the electric machine can aid the engine in this situation to increase acceleration and performance or it might run the car entirely on electricity. During vehicle deceleration, effective regenerative braking is also available. The machine may function as a generator if energy is needed to charge the battery, with the engine supplying power for both vehicle propulsion and battery charging.

With the exception of the electric machine being installed after the transmission and connecting to the output shaft via the differential gear ratio, the P3 arrangement is quite similar to the P2 configuration.

The P4 design either sets the electric machine on a separate axle or right next to the wheels. It directly drives the car by combining the power of the engine and the electric motor. The performance advantages of an All-Wheel Drive (AWD) powertrain and separation from the ICE are referred to as parallel performance benefits when the electric machine is on a different axle inside the P4 arrangement. The parallel powertrain's traditional operating modes are also compatible with this architecture. By exerting a braking torque on the electrically driven axle, it may also recharge the battery.

1.1.2 Power-split powertrains

The input-split hybrid power-split system uses power split components, such as planetary gear sets, at the side of the transmission that interfaces with the engines and electric machines. A mechanical path and an electric path are created from the engine power by the planetary gear set. The technology accomplishes variable output speed and torque by altering the amounts of power delivered through these two channels, enhancing vehicle fuel efficiency and lowering pollution. There are several hybrid synergy drive topologies that have been designed based on the planetary gear set architecture. The first configuration is the Toyota hybrid system (THS), which was used in the Toyota Prius prior to 2004. Figure 1.2 illustrates the THS system and its simplified block diagram.

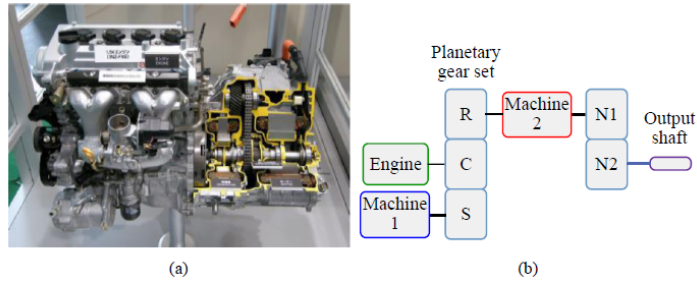


Figure 1.2: (a)Toyota hybrid system (b)block diagram representation[22].

The planet carrier is attached to the engine output shaft. With Machine 1 serving as the speed coupling, the sun gear is directly coupled to it. Together, the ring gear and Machine 2 deliver output torque and power to the car’s wheels. Machine 2 works to increase the engine’s torque, enabling the engine to run in zones of higher efficiency. The planetary gear set divides the engine’s power into an electrical path and a mechanical path as it is delivered to the transmission’s input shaft. The majority of the energy would be transferred mechanically to the final drive, while the remainder would be sent to Machine 1 operating as a generator.

Since the second generation of the Toyota Prius, the THS technology has undergone an upgrade and been dubbed hybrid synergy drive (HSD). It is widely utilized in the Toyota and Lexus hybrid lineups and has been licensed to Ford and Nissan. The second planetary gear set, where the planetary carrier is grounded to function as a fixed gear ratio, is one of the main differences between the THS and the HSD. Additionally, the THS system’s final drive’s chain coupling is gone. To increase vehicle speed, the HSD transaxles cut the overall gear ratio from the second ring gear to the differential and reduce the number of shafts from 4 to 3. Figure 1.3 illustrates the 2010 Toyota Prius HSD system its block diagram.

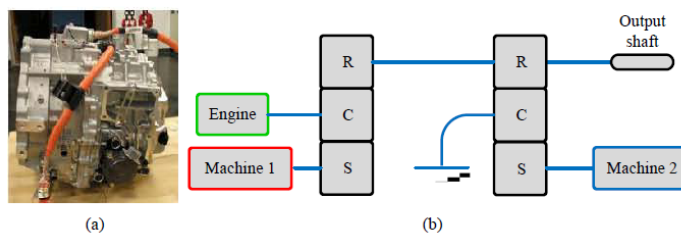


Figure 1.3: HSD system (a)2010 Toyota Prius Hybrid synergy drive (b)block diagram representation[22].

Additional power-split configurations have been developed, as illustrated in Figure 1.4. One has been applied on SUVs such as Lexus RX450h and Toyota Highlander for all-wheel drive (AWD) utilising a third electric machine (MGR) on the rear axle. The other

variation of the power-split system is to replace the second planetary gear set with a Ravigneaux (RAV) gear and two clutches so that the total gear ratio can be switched between low speed and high speed applications.

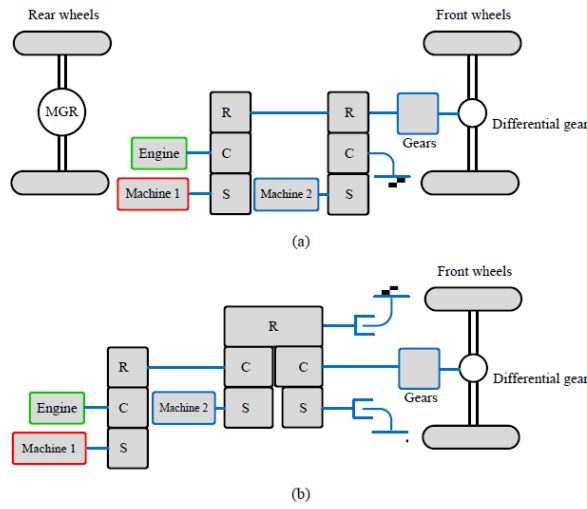


Figure 1.4: Variations of power-split systems (a)block diagram representation of the AWD drive system (b)block diagram representation of the HSD using Ravigneaux gear[22].

The power-split powertrains provide electric-only mode, engine start mode, motor assist mode, battery charge mode, and regenerative braking mode by coordinating the motor and generator output. Other driving modes, such as engine braking, uphill and downhill driving, cruising, coasting, and neutral, can also be used. In order to maximize the performance and economy of the powertrain, the electric machines are fully integrated into each driving mode. Engine torque and speed are separated from the output shaft, allowing the engine to operate within its ideal operating ranges and enhancing fuel efficiency. Greater system flexibility and performance are attained as a result of the two electric machines' dual functionality as a motor and a generator.

1.1.3 Two-mode hybrid powertrains

The two-mode hybrid incorporates the engine, electric machines, and mechanical gear sets in a compound hybrid system. Figure 1.5 illustrates GM's Allison two-mode hybrid transmission. By coordinating the two machines, clutches and brakes, this hybrid transmission provides more operating modes when compared to the power-split system. This enables the two-mode hybrid transmission to achieve improved fuel economy and uncompromised performance at both low and high vehicle speed.

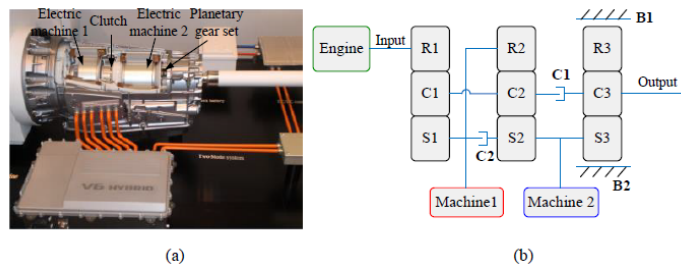


Figure 1.5: Two-mode hybrid transmission and its block diagram (a)GM two-mode Allison hybrid transmission (b)AHS block diagram[22].

Input-split mode

Engaging Brake B1 while disengaging other clutches enables input-split mode. In order to decouple the engine from the output shaft and increase engine efficiency, Machine 1 acts as a speed coupler to control engine speed and Machine 2 as a torque coupler to control engine torque. More frequently, input-split mode is employed in the relatively low-speed driving range. Increased power on the electric route due to energy conversion occurs at greater vehicle speeds, which also increases power losses.

Compound-split mode

Engaging Clutch C1 and disengaging other clutches, which are commonly employed for high-speed driving range, results in compound-split mode. All planetary gear sets work as power splitters in the compound-split mode to slice and alter the power ratio between the mechanical power stream and the electrical power path. The engine speed and torque are controlled by both electric machines, unlike the input-split mode. Due to a lower power ratio on the electric route, compound-split mode is more efficient at greater vehicle speeds.

Fixed gear ratios

GM's two-mode gearbox has the ability to go from continuously variable modes to fixed gear ratios by simultaneously activating two clutches. When Brake B1 and Clutch C2 are engaged, the first fixed gear ratio is created, which is employed to boost the output torque when high torque is needed for vehicle acceleration. By adjusting Clutch C1 and Brake B1, the second fixed gear ratio is employed as a transient mode that alternates between the input-split mode and the compound-split mode. Engaging both Clutch C1 and Clutch C2 results in a 1:1 input-output gear ratio, which is the third fixed gear ratio. Overdrive gear is the fourth fixed gear ratio. While Clutch 1 is engaged, Brake B2 locks Machine 2. It can be used in vehicle high speed operations where the engine operates in its efficient regions.

1.1.4 Series-parallel hybrid powertrains

The series-parallel architecture is an alternative to power-split designs, which divide the ICE's power flow into several routes using planetary gear sets. It varies from the traditional power split design in that it does not have the planetary gear set-based electronically continuously variable transmission (eCVT) capabilities. Instead, there is a direct mechanical link between two electric machines and the ICE. There is always a device linked to the ICE, typically referred to as the generator. During vehicle operation, it serves as a generator as well as a starting motor. A clutch separates the ICE and generator from a second electric machine. This second device provides traction power to the road and serves as the main traction motor. The powertrain modes of operation are summarised below:

- Electric-only operation: with the clutch open Machine 2 is the only torque source connected to the driveline and the road, enabling electric-only mode.
- Series operation: with clutch open, the engine is disconnected from the road but can drive Machine 1 to provide electrical energy to Machine 2. Since the engine is decoupled from the road it can be run in its greatest efficiency operating range. This mode is typically used when the vehicle is operating at low speeds with a low battery state of charge.
- Series-parallel operation: with the clutch engaged the engine provides power to the road in parallel with Machine 2. In this mode Machine 1 can also be used as a resistive torque source to force the engine to operate in its higher efficiency operating range.

There are only three commercial vehicle models available on the market to date that use the series-parallel hybrid architecture. The Hyundai Sonata Hybrid and Kia Optima Hybrid use the architecture defined in Figure 1.6(a). They use an electric machine as an integrated starter generator (ISG) and a larger traction machine for electric-only drive and hybrid operation. The other series-parallel configuration outlined above in Figure 1.6(b) is the architecture used by the Honda Accord Hybrid 2014. In the Honda Accord Hybrid architecture two larger electric machines are employed and the engine has two geared connections to each machine.

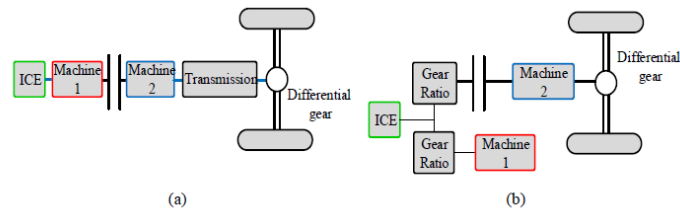


Figure 1.6: Series-parallel hybrid powertrain configurations (a)Hyundai Sonata Hybrid (b)Honda Accord Hybrid[22].

1.1.5 Plug-in hybrid electric vehicles

Plug-in hybrid electric vehicles (PHEVs) are a particular kind of hybrid electric cars, as their name indicates (HEV). The main distinctions between PHEVs and HEVs are their battery sizes and methods of charging. While a HEV is reliant on engine power, a PHEV may be charged straight from the power grid. Larger batteries in PHEVs enable them to operate entirely on battery power for a long distance, known as an all-electric driving range. This all-electric range is often made to accommodate PHEV owners' everyday driving needs, particularly those of city dwellers and suburban commuters.

Three major modes are available in PHEVs:

- Charge-depleting mode: charge-depleting (CD) mode refers to the PHEV operation mode in which the battery State-of-Charge (SOC) on average decreases while it may fluctuate along this trend.
- Charge-sustaining mode: charge-sustaining (CS) mode refers to the PHEV operation mode in which the battery SOC on average sustains a certain level while it may frequently fluctuate above and below this level. CS mode utilises both the engine and the electric machine to supply the vehicle power while keeping the SOC of the battery pack at a constant level.
- All-electric-range mode: the all-electric-range (AER) mode uses electricity exclusively as its energy source to power the vehicles.

The main goal of developing PHEVs is to boost the vehicle's electrification while decreasing pollution and fuel consumption by enabling quick journeys with charge depleting operation. PHEVs also provide additional advantages including reduced energy costs, lower maintenance costs, and grid-connected car charging. PHEVs also have the advantage over EVs in that they feature a fully working hybrid system that will run in a charge-sustaining mode, meaning the PHEV can go the same distance as a conventional car and drive like an EV for short journeys. The bigger battery does, however, raise the vehicle's weight and initial cost. An HEV would be the ideal vehicle to purchase if the owner of a PHEV only uses their car for long distance trips and the additional battery capacity is not used as much; however, if the owner uses the car for short commutes, an EV would be the greatest vehicle. A motorist who travels over a small distance and occasionally drives large distances may benefit most from a PHEV.

1.1.6 EREV powertrains

In contrast to plug-in hybrid cars, extended range electric vehicles (EREVs) have complete functionality in entirely electric mode. While an EREV will be able to operate at full capacity while using solely electricity, a PHEV may still rely on the ICE to obtain its maximum vehicle power. The basic goal of an EREV is to maintain an ICE on board while driving an all electric car in order to get around the range restriction of electric vehicles.

General Motors developed the Voltec 4ET50 Multi-Mode Electric Transaxle which has been used in the Chevrolet Volt and Cadillac ELR. The Voltec 4ET50 is a derivative of the GM 2-Mode Hybrid, with the specific goals of allowing fully capable complete EV operation. The Voltec provides four driving modes including two EV modes and two extended range (ER) modes. Figure 1.7 contains a block diagram of Voltec 4ET50 multi-mode electric transaxle configuration.

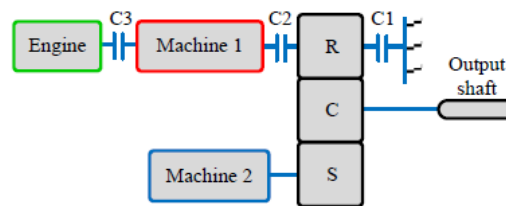


Figure 1.7: Voltec 4ET50 multi-mode electric transaxle configuration[22].

By activating Clutch 1 (C1), the speed and torque from Machine 2 may be transmitted straight to the output shaft through a reduction gear ratio, enabling the initial EV mode. The Voltec may use both of its electric engines in greater speed EV operating in the second EV mode. The Voltec utilizes a power-split ratio between the motors, distributing the speed and power between the two machines, while operating in two-motor EV mode with Clutch 2 (C2) engaged. The operating points of the machines can be moved closer to their areas of peak efficiency thanks to the control's adaptability.

The Voltec has a series mode and a power-split mode for longer range. The ICE is not mechanically connected to the wheels in series mode, when clutches C1 and C3 are engaged, unlike most other series hybrid architectures. The power flow travels from the engine via Machine 1's generator to Machine 2's electric drive motor, passing through a gear reduction on the way. In some circumstances, there are higher losses during the transition from mechanical to electrical and back to mechanical energy. This has a comparable drawback to an EV drive with a single motor because there is just one electric drive motor. The Voltec may transition to an output-split power flow, where clutches C2 and C3 are engaged, to prevent these drawbacks at specific operating conditions. The majority of the drawbacks of the series operation are eliminated by the output-split power flow, which enables the engine to apply power directly to the road. The output torque is restricted to the less powerful of the two electric motors in output-split and two-motor EV modes, which is a drawback.

When the vehicle runs as an electric vehicle, the powertrain control switches from a one-motor EV mode to a two-motor EV mode when high speed and low torque are needed, increasing economy. The Voltec changes between the two EV modes as well as the series and output-split modes when a charge has to be maintained while the vehicle is in extended range (ER) mode.

The BMW i3 is offered as another EREV. With a larger focus on operation only in EV mode, the ICE and generator are sized relatively smaller. The BMW i3 operates using a single motor and gear reduction in EV mode and when in ER operation the power flow is the same as a series hybrid.

1.1.7 EV powertrains

Electric vehicles (EVs) typically utilise simple powertrain configurations, in that they contain an electric machine, a fixed gear reduction and a mechanical differential to deliver the power to the wheels.

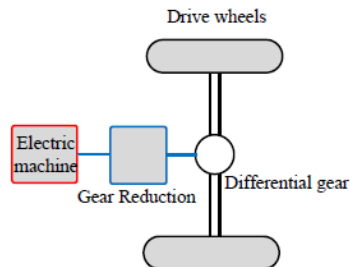


Figure 1.8: EV powertrain configuration[22].

An electric-only powertrain has the advantage of changing the motor needs to lower torque and greater speed. A single gear reduction is also strong since there are few spinning components and consistent mesh between the gears. Because there are no sliding parts, such clutches and synchronizers, a single reduction requires far less maintenance than a multi-gear gearbox. In general, EVs have prominent advantages:

- higher efficiency compared to the ICE efficiency
- zero tailpipe emissions
- low noise and smooth operation
- various energy sources for generating electricity
- less mechanical maintenance

1.1.8 Powertrain comparisons

By include additional electric components, hybrid, plug-in hybrid, and range-extended powertrains typically make the car more complicated. While two-mode hybrid drastically alters the engine architecture and increases complexity, parallel hybrids differ the least from conventional powertrains. On the other hand, an electric vehicle (EV) has the most basic setup because it has no engine or transmission gearbox other than a speed-reduction gear.

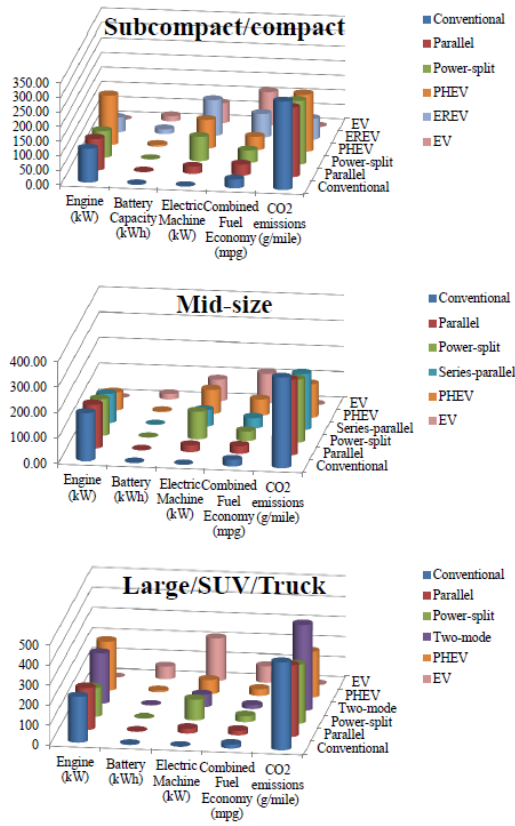


Figure 1.9: Comparison for various powertrain configurations based on vehicle classes[22].

To sum up, Figure 1.9 compares fuel economy, CO_2 emissions, and powertrain complexity of the presented electrified powertrains along with the conventional ICE powertrain. The efficiency is compared by calculating the average efficiency in each configuration, where the maximum efficiency, EV efficiency is selected as the benchmark reference, assigning the value 300 in Figure 1.9. The CO_2 emissions are converted into the same scale by using the emissions of the conventional vehicles as the reference benchmark, where the value of 300 is assigned. Finally, the powertrain complexity is calculated by adding the total component number in each configuration. The average value is taken for the cells where multiple configuration exist. The two-mode hybrid is selected as the benchmark reference because it has the maximum value

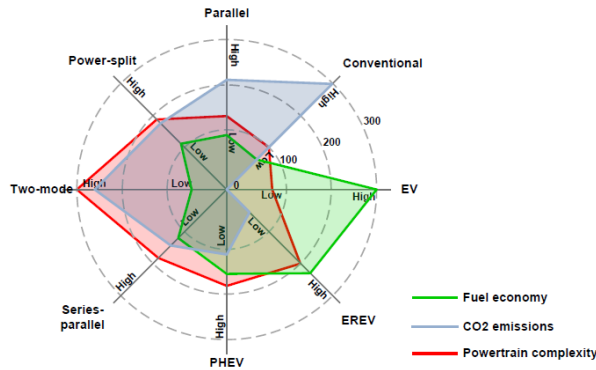


Figure 1.10: Powertrain comparisons in terms of fuel economy and complexity[22].

When comparing the powertrain designs, it can be shown that parallel hybrids increase

fuel economy and decrease emissions without significantly altering the complexity of the powertrain. They provide the most straightforward and affordable electrification option based on currently available conventional powertrains. As a result, several OEMs have employed parallel hybrids extensively. Full hybrids, including those with power-split, two-mode, and series-parallel powertrains, on the other hand, need considerable system integration and powertrain modifications in order to achieve improved fuel efficiency and fewer emissions. In terms of sales, power-split hybrids are by far the most widely used hybrid powertrains. Toyota and Ford contributed to more 70% of hybrid vehicle sales in the USA in 2014 by using power-split powertrains. Similarly, series-parallel hybrids are successfully commercialised using full hybrid configurations, which realise the balance between the system complexity and fuel improvement. As for two-mode hybrids, they were designed to achieve both performance and efficiency, especially at high speed range where the power-split powertrains typically has dropped efficiency. However, the powertrain cost and complexity are too high to justify their fuel economy gains and thus this type of powertrain has been discontinued since 2014.

In contrast, higher levels of electrification, such as those seen in EREVs, PHEVs, and EVs, result in far higher fuel economy benefits. Instead of using traditional fuels, substantially bigger batteries are often employed, and charging from external electrical connections makes this possible. In order to increase fuel efficiency and lower emissions, PHEVs and EREVs both use two different energy sources, and the drive range is not limited by the battery size. The main distinction between the two is that EREVs often have larger electric drive ranges and employ range extenders as backup and for longer ranges.

Figure 1.10 shows that EVs have the lowest powertrain complexity, the maximum fuel economy, and no emissions. However, pricing and battery limitations are where EVs reach their limit. The extra electric systems often necessitate new car platforms or significant redesigns, resulting in substantial research and production expenses. Larger battery packs are necessary because of the limited battery energy density, which adds weight and costs. Before EVs to take over the market, present disadvantages including a lengthy recharge time and battery performance degradation under high temperatures all need to be solved.

Chapter 2

Elements Structure for Electric Vehicles

The project developed in this thesis regards full Electric Vehicles (EV). The aim of this chapter is to show and analyse the model of the whole system generated for the simulation. The main elements taken into account are:

- DC power source
- Power electronic converter
- Synchronous Motor

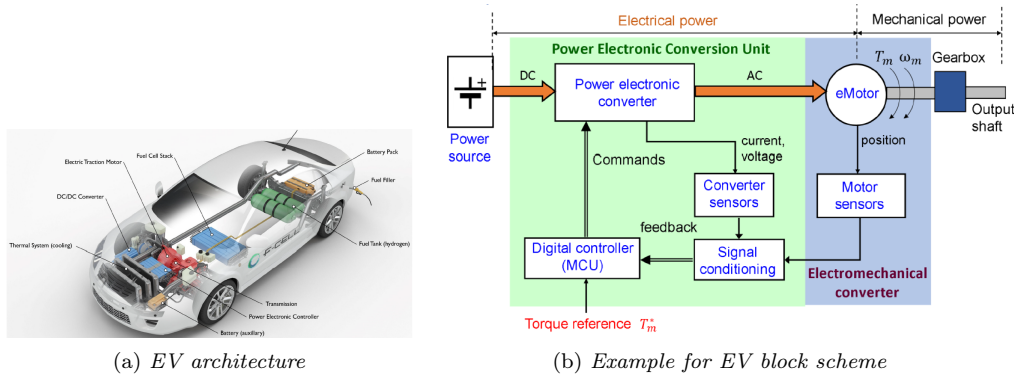


Figure 2.1: Elements Structure for Electric Vehicles[25].

2.1 DC power source

There are two types of electrochemical power source available for vehicle propulsion, namely, the secondary (or rechargeable) storage battery and the fuel cell. A storage battery consists of an assemblage of secondary cells which are chemically reversible to a degree that permits electrical recharging. A fuel cell consists of a particular fuel (hydrogen, methanol, hydrazine) and an oxidant to electricity. Power can be drawn from the cell as long as fuels are supplied and the reaction products are removed. Thus, batteries store electricity and require a plentiful supply of outside electricity to function, whereas fuel cells make electricity and require a plentiful supply of fuel. Although fuel cells have a considerable advantage over storage batteries in that they can be refueled in

a matter of minutes in much the same way as an ICE, fuel cell systems are not suitable for the high-rate, short-duration discharges needed to start and accelerate vehicles.

The technology of storage system for this electric vehicle is not strictly defined and for this reason a battery is preliminary selected. A battery consists of one or more electrochemical cells, which transform stored chemical energy directly into electrical energy. The voltage generated at the battery terminals is proportional to its State of Charge (SOC).

2.1.1 Battery

The battery is emulated with a controlled voltage source, without taking into account side effects like:

- Internal resistor in series
- Charge capacity
- Battery fade
- Thermal effects

The controlled voltage source is used to evaluate the charge dynamic, simulating a certain voltage variation due to the discharging.

Controlled Voltage Source

This block simulates an ideal voltage source that is powerful enough to maintain the requested voltage at its output regardless of the current flowing through it.

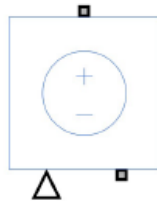


Figure 2.2: Simulink symbol for the Controlled Voltage Source block.

The requested voltage is given as Simulink signal to the signal port of the block, therefore it is possible to change it as necessary.

2.2 Power Electronic Converter

The system was simulated with different Matlab/Simulink toolbox to establish which one performs computationally better taking as a benchmark the same simulation taken with PLECS.

The converter chosen for the system under analysis is a three-phase inverter. It is a two levels inverter based on IGBT-technologies.

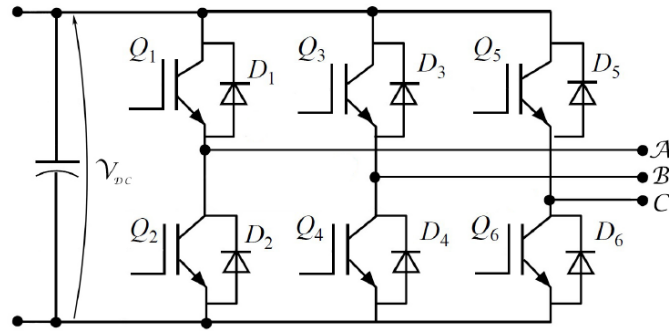


Figure 2.3: Scheme of a two level three-phase inverter.

This type of inverter has three legs, one for each phase. Every leg is constituted by two canonic cells, in turn each cell is constituted by an IGBT and a free-wheeling diode. Every IGBT is controlled by a command $Q(t)$, which is obtained by a PWM technique. This technique consist in the comparison between triangular carrier $tr(t)$ and a signal called duty cycle $d(t)$, done for each phase. The triangular carrier is symmetrical and its absolute maximum value $|\hat{V}_{tr}|$ is equal to one, as shown in Figure 2.4.

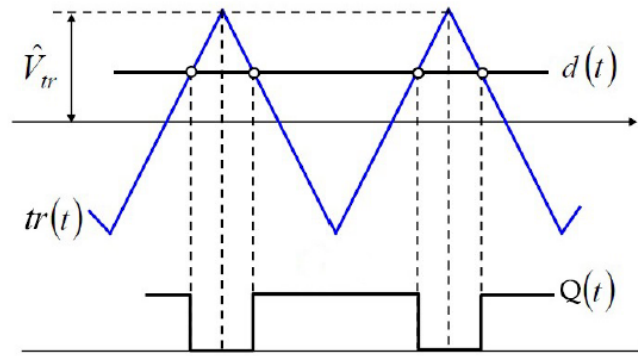


Figure 2.4: Comparison between the triangular carrier and duty cycle.

When the triangular carrier is higher than the duty cycle the command $Q(t)$ is equal to zero, while it is equal to one when the duty cycle is higher than the carrier. Three duty cycles are generated, one for each phase, thus three commands $Q(t)$ are generated for the high-side IGBT and the commands for the low side ones are equal to the negative of respective high-side one commands. Utilising a zero-sequence voltage injection, the duty cycle is evaluated for each phase as follows:

$$\begin{aligned}
 d_A &= \frac{1}{2} + \frac{v_A^*}{V_{DC}} - \frac{1}{2} \frac{v_{min}^* + v_{max}^*}{V_{DC}} \\
 d_B &= \frac{1}{2} + \frac{v_B^*}{V_{DC}} - \frac{1}{2} \frac{v_{min}^* + v_{max}^*}{V_{DC}} \\
 d_C &= \frac{1}{2} + \frac{v_C^*}{V_{DC}} - \frac{1}{2} \frac{v_{min}^* + v_{max}^*}{V_{DC}}
 \end{aligned} \tag{2.1}$$

Where:

- V_{DC} is the voltage of the DC-link capacitor;
- v_A^*, v_B^* and v_C^* are the reference voltage for each phase, namely the desired output voltage;

- v_{min}^* and v_{max}^* are respectively the minimum and the maximum reference voltage.

The output moving average voltage are equivalent to:

$$\begin{aligned} v_A &= \frac{1}{3}V_{DC}(2d_A - d_B - d_C) \\ v_B &= \frac{1}{3}V_{DC}(2d_B - d_A - d_C) \\ v_C &= \frac{1}{3}V_{DC}(2d_C - d_A - d_B) \end{aligned} \quad (2.2)$$

In order to model this inverter, there are two possibility for the simulation tool employed:

- IGBT
- Two-level converter

In PLECS is only applicable the IGBT approach. Simulink provides two different toolbox for electrical simulation:

- Simscape \rightarrow Electrical: used to employ the inverter using components representing single IGBTs.
- Simscape \rightarrow Specialized Power Systems: used to employ the inverter with a single component two-level converter.

2.2.1 IGBT

The IGBT block simulate as an insulated gate bipolar transistor with two electrical port (collector and emitter) and a command port (gate). The symbol of this block is:

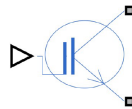


Figure 2.5: Simulink: Simscape \rightarrow Electrical symbol for the IGBT block.

A voltage is applied to the command port: if it is higher than a threshold (adjustable by the user) the IGBT moves to an ON-state, otherwise it stay in a state of interdiction (OFF-state).

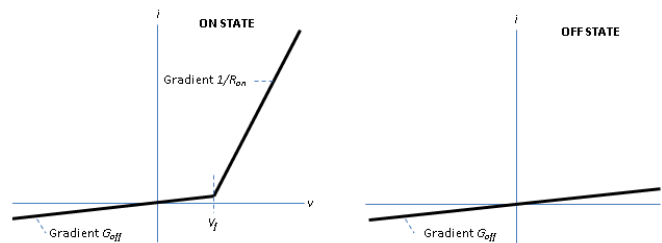


Figure 2.6: Current-Voltage curves of the IGBT[26].

where:

- V_f is the forward voltage of the IGBT in the ON-state;

- R_{ON} is the ON-state resistance, which is the internal resistance that the device offers during conduction and is represented by the slope of the device conduction characteristic;
- G_{off} is the OFF-state conductance, which is the internal resistance that the device offers during interdiction and is represented by the slope of the interdiction device characteristic.

This block has also the possibility to insert a free-wheeling diode, called "protection diode" by Simulink, whose parameters can be customize by the user. These parameters are of the same topology of the IGBT with the same properties.

In order to model the converter under study six IGBT blocks are necessary with the respective protection.

2.2.2 Two-level converter

The two level converter block implements a three-phase two-level power converter using the following modeling:

- Switching devices: the converter is modeled with IGBT/diode pairs controlled by firing pulses produced by a PWM generator.
- Switching function: the converter is modeled by a switching function controlled by firing pulses produced by a PWM generator (0/1 signals) or by firing pulses averaged over a specified period (PWM averaging: signals between 0 and 1).
- Average model (Uref-controlled): the converter is modeled using a switching-function model directly controlled by the reference voltage. A PWM generator is not required.

Technique 1 is the most accurate, while technique 3 yields to the fastest simulation. The two techniques in 2 are well-suited for real-time simulation.

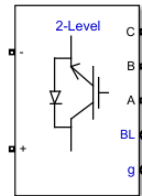
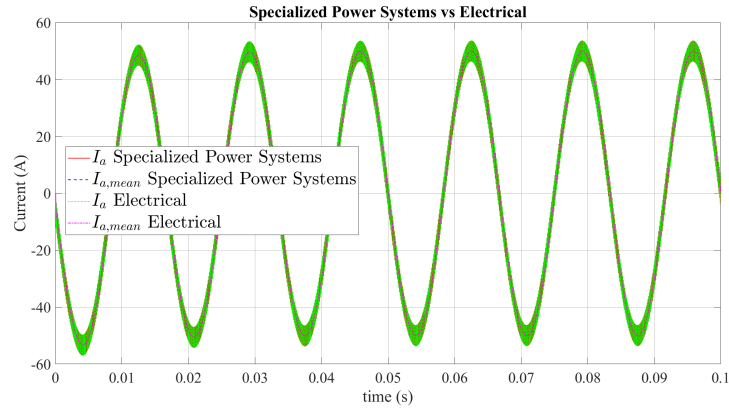


Figure 2.7: Simscape→ Specialized Power Systems symbol for the Two-level converter block.

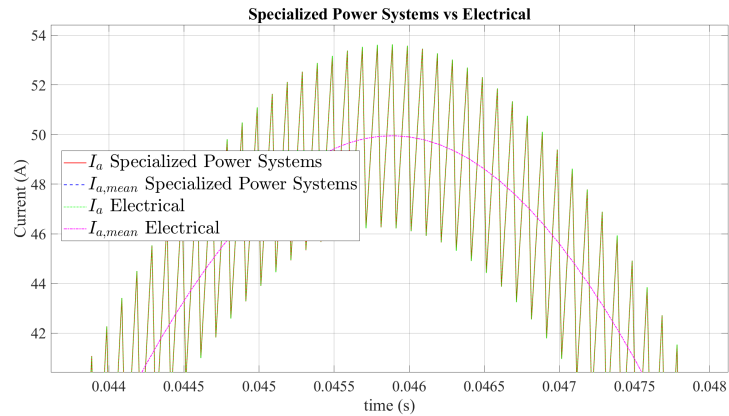
Block selection and evaluation

The two possible solutions are evaluated in order to find out the best suitable. A test to compare the two blocks has been done with the following conditions:

- V_{DC} equal to 400V
- Real IGBT with ON-state resistance equal to $1m\Omega$
- Switching frequency $f_{sw} = 10kHz$
- Three-phase load consisted of a resistor $R = 0.1\Omega$, an inductor $L = 1mH$ and electromotive force $E = 195 \cdot ma$ and frequency $f_o = 50Hz$ where ma is the Modulation Amplitude chosen.



(a) View of the current of phase a in the inverter test



(b) Detail of current of phase a in the inverter test

Figure 2.8: Current of phase a ($m_a=0.5$).

As it is possible to notice in Figure 2.8, they are exactly the same thus there is not difference between the two blocks. The only discriminating factor is the possibility to explore the inverter scheme with the IGBT block, therefore it offers the chance to test different situations, such as the short-circuit of one IGBT. Nevertheless the shorter computation time made sure to prefer the Simscape \rightarrow Specialized Power Systems Toolbox used so on for all the simulations.

2.2.3 Inverter Non-Linear Effects

The inverter modeling has been analyzed in many papers, with the aim at describing and compensating the voltage error between the command voltage and the actual motor voltage. As already known, this voltage error is produced by the following sources:

- Inverter dead-time;
- On-state voltage drops on the power switches.

Inverter dead-time

If the switching devices of one leg of the inverter are assumed to be ideal, the states of two switching devices (Q_{A+} and Q_{A-}) can be changed simultaneously from on to off and vice versa. In practice switching devices have finite turn-on and turn-off delays and there can also be differences in timing delays between the gate circuitry driving switches Q_{A+} and Q_{A-} . Therefore the turn-on of the switching devices is delayed by a few microseconds to prevent the probability of having both switches in a leg turned on at the same time for the transition period.

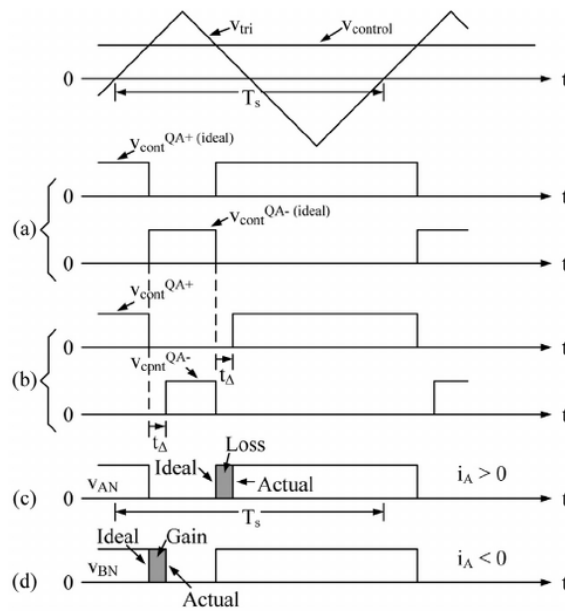


Figure 2.9: Effect of dead-time[21].

The switching instant is determined by the comparison of the triangular waveform (v_{tri}) and the control voltage ($v_{control}$), and in ideal switching devices (Q_{A+} and Q_{A-}) the change over from on to off and vice versa happens simultaneously as shown in figure 2.9(a). In practice a switching device is turned off at the instant determined by the comparison of the triangular waveform (v_{tri}) and the control voltage ($v_{control}$) but the turn-on of the other switch is delayed by a few microseconds, as shown in figure 2.9(b). This time is called Dead Time or Blanking Time (t_{Δ} where both upper and lower switches are off, and this avoid "shoot through" or cross-conduction current through the leg. The slower the switching device, the larger is the dead time needed. The dead time introduces a non-linearity which causes distortion in the output voltage and current, and therefore the smaller is the dead time the better.

Since both switches of the leg are off during the dead time the output voltage of the leg v_{AN} depends on the direction of the current i_a as shown in Figure 2.9(c) for $i_a > 0$ and in Figure 2.9(d) for $i_a < 0$. The ideal waveforms without dead time are shown for both cases in Figure 2.9(c) and (d). There is a decrease in the pulsewidth when the current is greater than zero ($i_a > 0$) as shown in Figure 2.9(c) and there is an increase in the pulsewidth when the current is less than zero ($i_a < 0$) as shown in Figure 2.9(d).

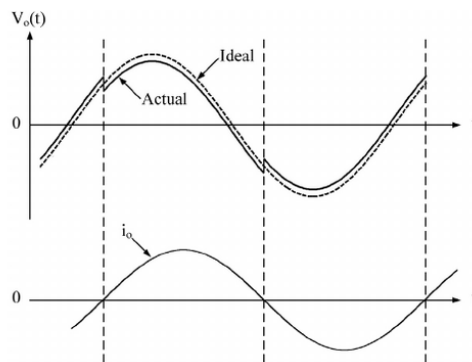


Figure 2.10: Effect of dead-time on the sinusoidal waveform of the instantaneous average output voltage[21].

Figure 2.10 shows the distortion effect of the dead time on the sinusoidal waveform of the instantaneous average output voltage $v_o(t)$, for a sinusoidal $v_{control}$ and for a load current i_o which is assumed to be sinusoidal and lagging behind $v_o(t)$, in a single phase full-bridge PWM inverter. The distortion in $v_o(t)$ at the current zero crossings causes low order harmonics such as third, fifth, seventh and so on, of the fundamental frequency in the inverter output.

As demonstrated in the literature [17], the overall inverter voltage error vector is

$$\bar{v}_{err} = \frac{4}{3}V'_{th}sign(\bar{i}) + R_d\bar{i} \quad (2.3)$$

where $V'_{th} = V_{th} + t_{df_s}V_{dc}$. The inverter nonlinear effects is represented by the equivalent term V'_{th} that includes both dead-time and on-state threshold voltage. At low current levels the power switches turn-off time increase dramatically. That is equivalent to a reduction of the term V'_{th} .

2.2.4 Simulation of dead-time

As said previously i choose to use for the further simulations the Specialized Power Sytem Toolbox utilising the Two-level converter block. This block take into account the real nature of the switches considering itself the on-state voltage drops on the power switches. That cannot be said for the dead-time which had to be added in the computation of the duty cycle. We call this technique to simulate dead-time "DeltaD method".

The DeltaD method consists of adding and subtracting to the desired duty cycle a small quantity DeltaD proportional to the amount of dead-time we want to simulate in a relation of the type:

$$DeltaD = t_{dT}\dot{f}_{sw} \quad (2.4)$$

So we obtain two new duty cycles, the higher one ($d_h = d + DeltaD$) is going to command the lower switch, the lower ($d_l = d - DeltaD$) is going to command the higher switch.

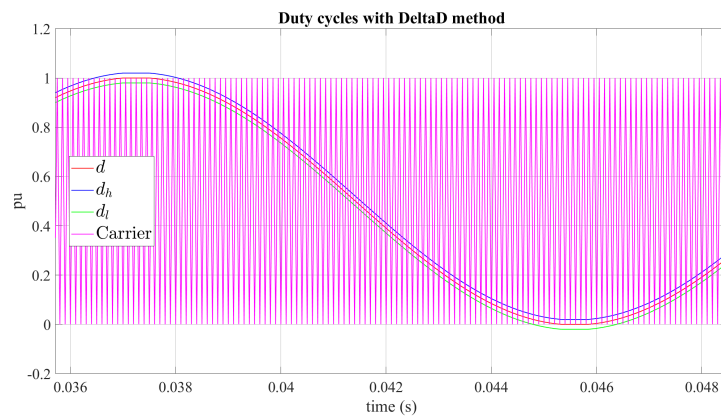
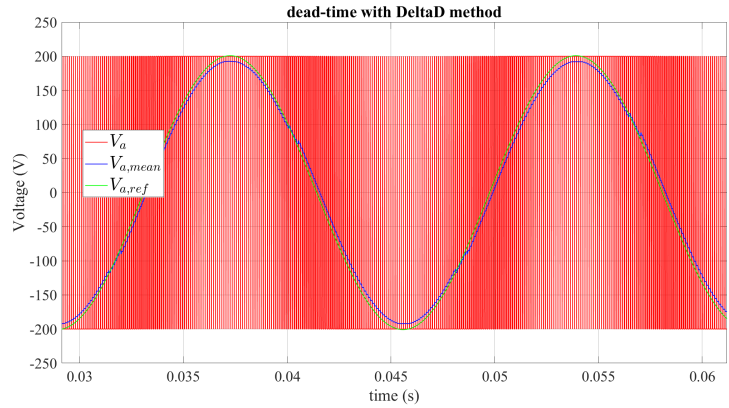
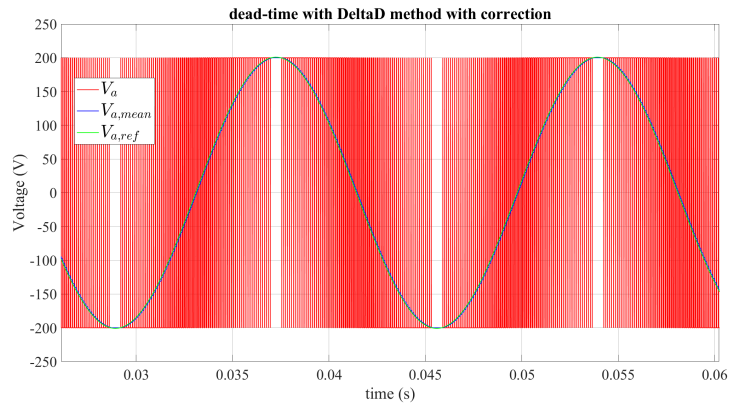


Figure 2.11: Duty cycles elaborated with DeltaD method (ma=1).

As can be noted from Figure 2.11 the new duty cycles elaborated d_h and d_l create some issues when $ma \geq 1$ or $ma = 0$ because in these situations the new duty cycles remain under the saturation limit of the duty cycle that are 0 and 1. In particular when $d = 1$ we have that $d_l = 1 - deltaD$ and that cause the inverter to continue switching instead of stop the switching when d reach the saturation limit as happens in the reality. So we need to apply a correction to the DeltaD method that forces the switches to don't switch when the real duty cycle reach the saturation limits.



(a) Phase voltage V_a when DeltaD method is applied without correction



(b) Phase voltage V_a when DeltaD method is applied with correction

Figure 2.12: Phase voltage V_a ($m_a=1$).

Figure 2.12 shows the two different behaviours of the instantaneous phase voltage V_a when the DeltaD method is applied with and without correction. In both cases can be noted the distortion effect due to the dead-time expected at current zero crossing causes by the appearance of low harmonics.

2.3 e-Motors

The main component of a e-Drive is the e-Motor. E-Motors can be divided in different categories mainly depending by their rotor configuration.

- Induction motors (IM).
- Synchronous motors:
 - Surface-mounted Permanent Magnet (SPM)
 - Internal Permanent Magnet (IPM)
 - PM-assisted Synchronous reluctance (PM-SyR)
 - Synchronous reluctance (SyR)

A 3-phase stator supplied by balanced 3-phase currents produces a magnetic field and so a magnetomotive force (MMF) rotating at the synchronous speed $\omega_s = \frac{\omega}{p}$, where $\omega = 2\pi f$ is the electrical speed and p is the number of pole pairs.

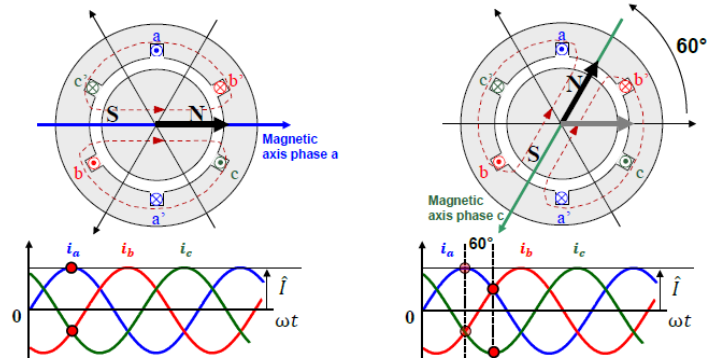


Figure 2.13: Rotating magnetic field explanation[25].

In synchronous machines the rotor speed is rigidly related to the AC frequency imposed by the inverter ($\omega_m = \frac{2\pi f}{p} = \omega_s$). In Induction machines (IM) the rotor speed "slips" with respect to the AC frequency imposed by the stator ($\omega_m < \frac{2\pi f}{p}$)

Induction Motors

The IM motor can be designed in two versions:

- Squirrel cage (the most used): the rotor contains a series of conductive bars shorted by end rings.
- Wound rotor (mainly for generators in wind turbines): 3-phase rotor winding set, requires slip rings and brushes (only when used as generator).



Figure 2.14: Induction motor types[25].

The rotor cage is equivalent to a rotating three-phase winding. As in a "rotating transformer", rotor currents are induced in the shorted rotor windings. Torque is produced by interaction of the stator field with rotor currents. The rotor tends to synchronize to the excitation field $\omega/p \rightarrow$ synchronism $\omega_m = \omega/p$ coincides with zero torque condition. Torque is non-zero only if the rotor speed slips respect to the synchronous speed.

Slip definition:

$$s = \frac{\omega_s - \omega_m}{\omega_s} \cdot 100(\%) \quad (2.5)$$

- $\omega_s = \omega/p$ is the mechanical synchronous speed (field imposed by the stator supply)
- ω_m is the rotor speed (mechanical speed)
- $s = 0 \rightarrow \omega_m = \omega_s$ coincides with no-load conditions.

The nominal slip (at rated torque) is circa 3-5%. Although the rotor slips respect to the rotating field, all electrical and magnetic quantities (including the rotor flux vector) do rotate synchronously.

Absolute position is unnecessary since the rotor is isotropic. In EVs resolver is normally adopted for position measuring. Sensorless control is also possible. Stator and rotor core must be laminated.

An IM motor needs a magnetizing stator current to create the magnetic field. The efficiency can be improved by using a copper cage (costly) and by adjusting the machine flux level according to the torque request (MTPA in vector control). In the latter case, however, the rotor cage relents the flux change dynamics. IM motors are recognized for a good flux-weakening capability, better than SyR motor competitors, and for the self-starting capability for grid connected applications.

Synchronous Motors

For synchronous machines the rotor design imposes the motor type and name. A wide number of different rotor structures are possible.

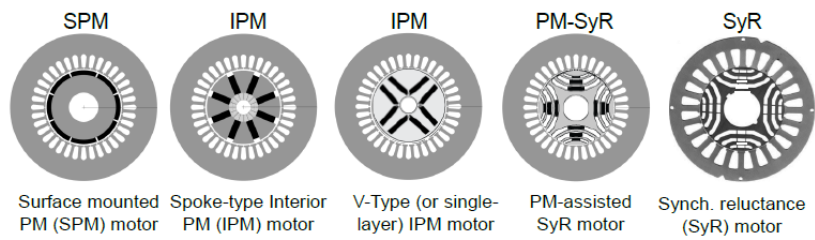


Figure 2.15: Synchronous motor types[25].

The torque produced by the synchronous motor is made by two components:

- **PM torque:** each stator current produces a torque component in association with the PM magnetic field along the airgap (Lorents law)
- **Reluctance torque:** if the rotor is anisotropic, i.e. the inductance is not constant along the airgap, the rotor reacts to the stator magnetic field and tends to follow the wave currents. In other words, the rotor tends to align with the direction of maximum inductance along the magnetic field imposed by the stator, to minimize its magnetic energy.

As an example, we consider a SPM machine (PM mounted on the surface of the stator).

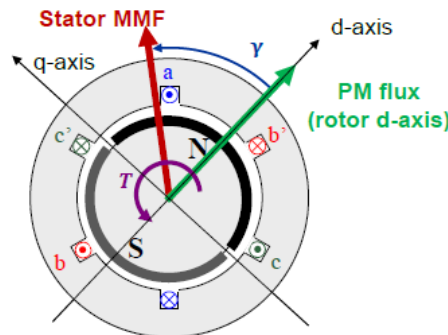


Figure 2.16: SPM synchronous motor[25].

- Since the PM have almost the same magnetic permeability of the air, the reluctance (and so the inductance) computed along any direction is constant

- The PM flux tends to align the rotor with the MMF generated by the stator, thus producing PM torque (T_{pm})
- The torque is proportional to the external product between PM flux and stator MMF (Lorentz law)
- Therefore, for a given current (and so MMF) amplitude, T_{pm} is maximized if the two vectors are orthogonal ($\gamma = 90^\circ$, i.e the current is aligned with the rotor q-axis)

We can take another example considering a SyR machine: high anisotropy rotor without PM.

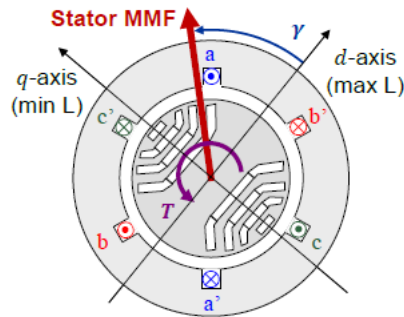


Figure 2.17: SyR synchronous motor[25].

- The rotor presents some "cuts", called flux barriers
- The magnetic permeance in the air is much lower than in the iron
- The reluctance (and so the inductance) strongly depends on the direction (or path) where it is computed
- The direction of maximum L is called d axis whereas the quadrature direction (q axis) presents minimum L. their values are called L_d and L_q
- In presence of a MMF, the rotor tends to minimize its magnetic energy by aligning the d axis with the MMF (T_{rel})
- To produce torque, both MMF components along d and q axes are necessary. In absence of magnetic saturation the optimal current angle is $\gamma = 45^\circ$

A generic PMSM may be capable of producing both torque components T_{rel} and T_{pm} . Example: Interior Permanent Magnets (IPM) synchronous motor.

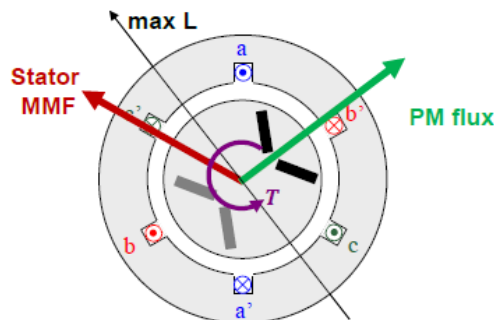


Figure 2.18: IPM synchronous motor[25].

- The PM are insert into the rotor
- The rotor is anisotropic
- Optimal current angle depends on motor parameters (PM flux, saliency ratio, magnetic saturation, required torque)

In synchronous motors the rotor position must be measured (encoder,resolver) or estimated via electrical quantities (sensorless control), for AC synchronization purposes. Stator and rotor cores must be laminated.

Synchronous motors characteristics

- Surface Mount PM machine
 - Permanent magnets (NdFeB, SmCo) mounted at the rotor surface
 - Motors with the highest possible torque density, but require a lot (costly) PM
 - Isotropic structure: the machine inductances on (d,q) axes are practically the same
 - The reluctance torque is null, only PM torque is possible
- Interna PM machine
 - Permanent magnets (NdFeB, SmCo) buried in the rotor surface
 - Normally high torque density
 - The anisotropy ratio $\psi = \frac{L_d}{L_q} = 2 - 3$
 - Both Pm and reluctance torque, $T_{pm} \gg T_{rel}$
 - The torque maximization requires coordinated control of the two current components i_d, i_q
- Synchronous Reluctance (SyR) machine
 - No PM (cost reduction), good torque density but poor power factor
 - Only reluctance torque is exploited
 - High anisotropy ratio $\psi = \frac{L_d}{L_q} = 5 - 8$
 - The torque maximization requires coordinated control of the two current components i_d, i_q
 - By definition, the d axis is the one with the maximum inductance (different from IPM)
- PM-assisted Synchronous Reluctance (PM-SyR) machine
 - Rotor structure similar to SyR, but PMs partially fill the flux barriers
 - Slightly higher cost and torque density, same anisotropy ratio, much better power factor
 - Mainlye $T_{rel} \approx 20\%$ PM torque
 - The torque maximization requires coordinated control of the two current components i_d, i_q
 - The d axis is the one with the maximum inductance (different from IPM)

	Asynchronous motors		Synchronous motors			
	Squirrel cage	Wound rotor	SPM	IPM	PM-SyR	SyR
Cost	Low	Medium-high	High	Medium	Medium-low	Low
Efficiency	Medium	Medium	High	High	High	Medium-high
T density	Medium-high	Medium-high	Very high	High	Medium-high	Medium
FW capability^(*)	Medium-high	High	Very low ^(**)	Medium	Very high	Low
Anisotropy	No	No	No	Low, $L_q > L_d$	High $L_d \gg L_q$	High $L_d \gg L_q$
PM	No	No	High (rare heart)	High (rare heart)	Low (rare hearth or ferrite)	No
d axis	Rotor flux	Rotor flux	PM direction	PM direction	Max L	Max L
Optimal γ	$0 < \gamma < \pi/2$	$0 < \gamma < \pi/2$	$\gamma = \pi/2$	$\pi/2 < \gamma < \pi$	$0 < \gamma < \pi/2$	$0 < \gamma < \pi/2$

Figure 2.19: Summary motor types and characteristics[25].

Chapter 3

E-Motor Modeling

The motor chosen for the project is the HSM1-10.18.13-D04 (BRUSA), an IPM motor rated 93 kW, 165 Nm, 12000 rpm. The model of synchronous machines are convenient to be defined in rotor (dq) coordinates to get current-to-flux relationships that do not depend on the rotor position. For this reason, (dq) models of the machine are directly reported in the following, without considering those defined in stationary ($\alpha\beta$) coordinates.

3.1 Dynamic model in dq frame

Voltage and flux linkage equation of synchronous motor can be written in both stator and rotor coordinates, as shown in Figure 3.1.

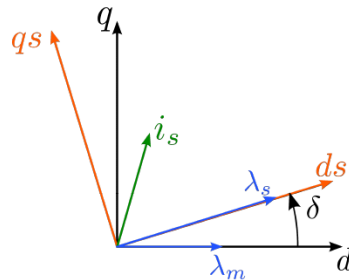


Figure 3.1: Example of (dq) rotor and ($d_s q_s$) stator flux-linkage reference frames.

The starting point for the definition of the frames is the direction of the flux linkage vector. λ_s represents the stator flux-linkage vector while λ_m represents the magnets flux-linkage vector.

Since the stator coordinates refer to the position of the stator flux-linkage vector, the definition of the ($d_s q_s$) frame is univocal. Conversely, the definition of the rotor (dq) frame depends by the adopted convention. Typically, there are two (dq) rotor frame conventions that can be adopted:

- For SPM and IPM motors, the d -axis position usually corresponds to that defined by the flux-linkage vector of the magnet. In this thesis, this convention is called "PM-style" convention. Therefore, since the permanent magnets present a non-ferromagnetic behavior, the d -axis inductance is lower than the q -axis one when using "PM-style" convention.
- For SyR motors, d -axis position is made coincident with the direction presenting the minimum magnetic reluctance. Therefore, the d -axis inductance is higher than the q -axis one when using this convention, here called "SyR-style" convention.

Although it is useful to use one convention for modeling all motors, as schematically shown in Figure 3.2.

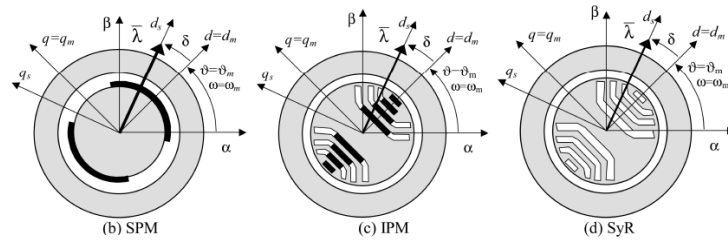


Figure 3.2: Application of "PM-style" convention for synchronous motors[9].

3.1.1 Voltage Equation

According to the literature [24], the voltage (dq) model of a synchronous machine is computed as:

$$\bar{v}_{dq} = R_s \bar{i}_{dq} + \frac{d}{dt} \bar{\lambda}_{dq} + p\omega_m J \bar{\lambda}_{dq} \quad (3.1)$$

where $J = \begin{bmatrix} 0 & -1 \\ 1 & 0 \end{bmatrix}$. Starting from the voltage equation (3.1) in (dq) frame, the two components of the equation can be retrieved as:

$$\begin{cases} v_d = R_s i_d + \frac{d}{dt} \lambda_d - p\omega_m \lambda_q \\ v_q = R_s i_q + \frac{d}{dt} \lambda_q + p\omega_m \lambda_d \end{cases} \quad (3.2)$$

In rotating stator components, (3.1) is expressed in stator ($d_s q_s$) coordinates, leading to:

$$\begin{cases} v_{ds} = R_s i_{ds} + \frac{d}{dt} |\bar{\lambda}_s| \\ v_{qs} = R_s i_{qs} + |\bar{\lambda}_s| \frac{d}{dt} \delta + p\omega_m |\bar{\lambda}_s| \end{cases} \quad (3.3)$$

3.1.2 Flux Linkage Equation

If considering an IPM motor (most generic case), the flux linkage equations representing the magnetic model is (3.4):

$$\bar{\lambda} = L \bar{i}_{dq} + \bar{\lambda}_m \quad (3.4)$$

where L is the apparent inductance matrix.

By expressing the equation above in (dq) components, the following is obtained:

$$\begin{cases} \lambda_d = L_{dd}(i_d, i_q) i_d + L_{dq}(i_d, i_q) i_q + |\bar{\lambda}_m| \\ \lambda_q = L_{qd}(i_d, i_q) i_d + L_{qq}(i_d, i_q) i_q \end{cases} \quad (3.5)$$

where L_{dd} and L_{qq} are the apparent self-inductances of the machine along the d -axis and q -axis, respectively, while L_{dq} and L_{qd} are the apparent cross-inductances of the machine along the d -axis and q -axis, respectively; these last are used to model the cross saturation phenomena. Finally λ_m represents the amplitude of the PM flux linkage vector, whose value is assumed constant and not dependent on the PM temperature for simplicity. In (3.5) the "PM-style" convention is used.

It is highlighted that SyR motors can be modeled using (3.5) by simply setting the PM flux contribution to zero.

3.1.3 Torque Equation

The electromagnetic torque equation can be retrieved by performing the power balance of the machine. Electric power in input is expressed as:

$$P_{el} = P_{stator} = \frac{3}{2} \bar{v}_s \cdot \bar{i}_s \quad (3.6)$$

By replacing (3.1) in (3.8) the following is obtained:

$$P_{el} = \frac{3}{2} R_s |\bar{i}_{dq}|^2 + \frac{3}{2} \left(\frac{d}{dt} \bar{\lambda}_{dq} \right) \cdot \bar{i}_{dq} + \frac{3}{2} (p \omega_m J \bar{\lambda}_{dq}) \cdot \bar{i}_{dq} \quad (3.7)$$

where $[\frac{3}{2} R_s |\bar{i}_{dq}|^2]$ represents the stator Joule losses, while $[\frac{3}{2} (\frac{d}{dt} \bar{\lambda}_{dq}) \bar{i}_{dq}]$ is the magnetizing power that becomes zero in steady-state conditions. Therefore the mechanic power of the machine is:

$$P_{mecc} = \frac{3}{2} (p \omega_m J \bar{\lambda}_{dq}) \cdot \bar{i}_{dq} \quad (3.8)$$

leading to the following expression of the electromagnetic torque:

$$T = \frac{P_{mecc}}{\omega_m} = \frac{3}{2} (p J \bar{\lambda}_{dq}) \cdot \bar{i}_{dq} \quad (3.9)$$

that is equivalent to:

$$T = \frac{3}{2} p (\bar{\lambda}_{dq} \wedge \bar{i}_{dq}) \quad (3.10)$$

Different expression of the torque equation can be obtained as:

- Using (dq) rotor reference frame leads to (3.11) in which the machine torque is proportional to the outer product between the stator flux linkage vector and stator current vector. Therefore, it depends only on the shift angle between the two vectors regardless of the considered reference frame:

$$T = \frac{3}{2} p (\lambda_d i_q - \lambda_q i_d) \quad (3.11)$$

Using (3.5) in (3.11), the PM and reluctance to the torque production are put in evidence (for simplicity the cross saturation terms in (3.5) are neglected):

$$T = \frac{3}{2} p [(L_{dd} i_d + |\bar{\lambda}_m|) i_q - (L_{qq} i_q) i_d] = \frac{3}{2} p [(L_{dd} - L_{qq}) i_d i_q + |\bar{\lambda}_m| i_q] \quad (3.12)$$

The first term is the reluctance torque of the machine, proportional to the product of the current components, while the second term represents the torque produced by the magnets.

- Using $(d_s q_s)$ stator flux reference frame the torque expression is:

$$T = \frac{3}{2} p (\bar{\lambda}_{dqs} \wedge \bar{i}_{dqs}) = \frac{3}{2} p \lambda i_{qs} \quad (3.13)$$

This is useful when it is necessary to correlate the torque to the stator flux linkage.

3.1.4 Flux Maps

Following the experimental identification procedure of the magnetic model of synchronous motor reported in [13] and [15], the flux maps of the motor adopted have been generated. This maps can be generally described by the flux linkage equation (3.5) that consider both the contribute of permanent magnets motor inductances. In Figure 3.3 the flux-linkage maps of the IPM machine is shown.

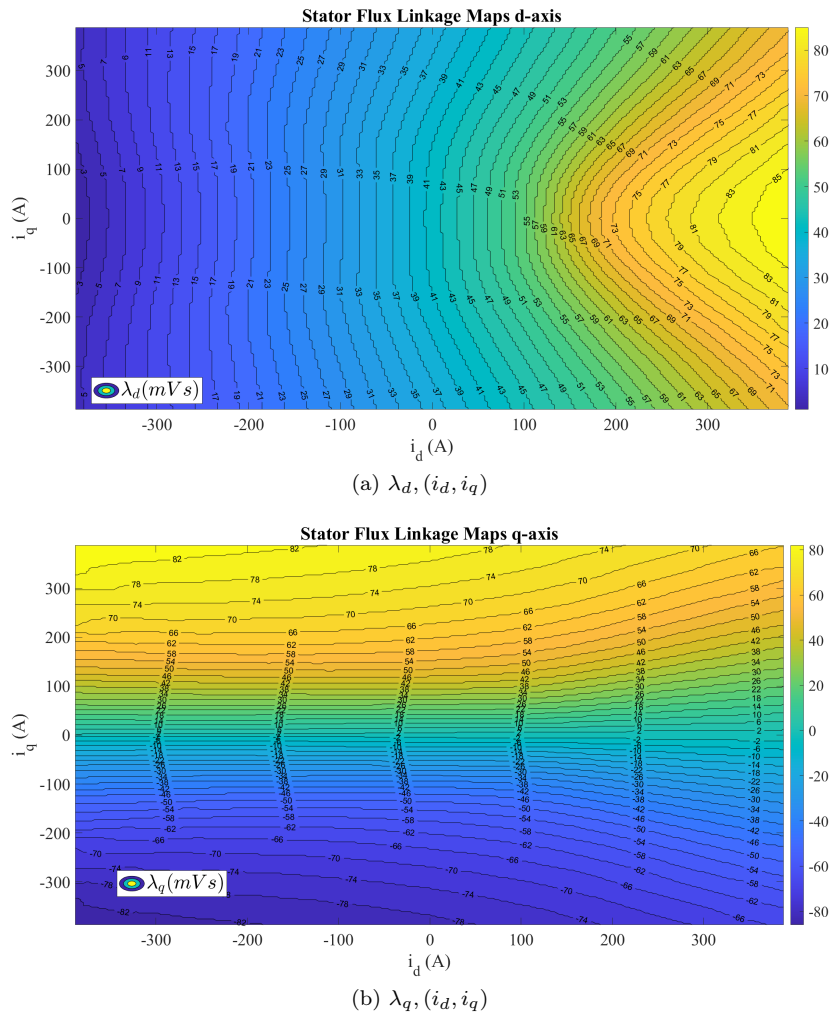


Figure 3.3: Flux-linkage maps of IPM motor used in the simulations.

To provide a clearer representation of the magnetic behavior of each motor under consideration, the profiles on the flux linkage maps are reported in Figure 3.4 using the "PM-style" axes convention.

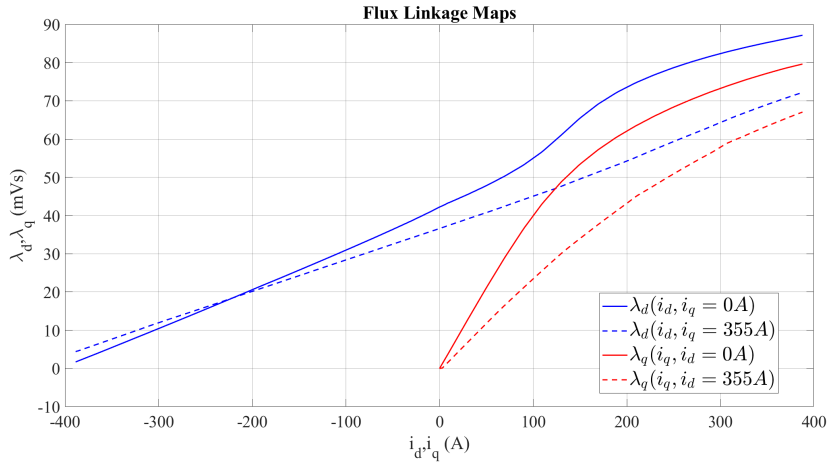


Figure 3.4: Flux-linkage profiles of the IPM motor used in the simulations.

For IPM motors the d -axis profiles are shifted from the origin ($i_D = 0A, i_q = 0A$) due to the presence of the PM flux ("PM-style" convention). The motor moreover, presents an evident saturated behaviour along the q -axis. This means that the values of the differential inductances strongly depends on the motor's operating points. Therefore, if the torque controller is based on inner current loops, like in Field Oriented Control (FOC) or in Direct Flux Vector Control (DFVC) schemes, demanding tuning process of the related current regulator is necessary.

Starting from the flux linkage maps, the flux-to-current maps can be obtained since they are useful for the computation of the (Maximum Torque per Volt) MTPV locus and are also necessary to model the e-Drive using a mathematical, non circuital, discrete-time average model. In Figure 3.5 the inverse flux-linkage maps of the motors under consideration are shown.

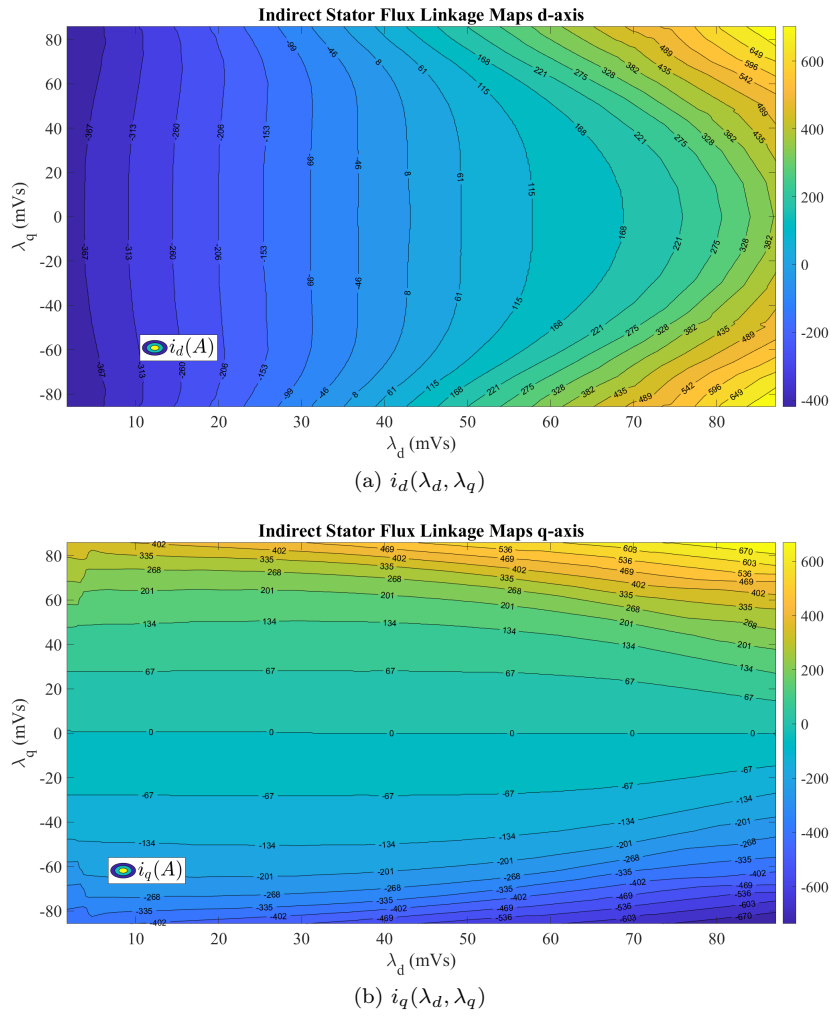


Figure 3.5: Indirect flux maps of IPM motor used in the simulations.

3.2 Non-circuital, inverse maps model

The starting point of the e-Drive modeling is a non circuital, discrete-time average model, used as benchmark and shown in Figure 3.6

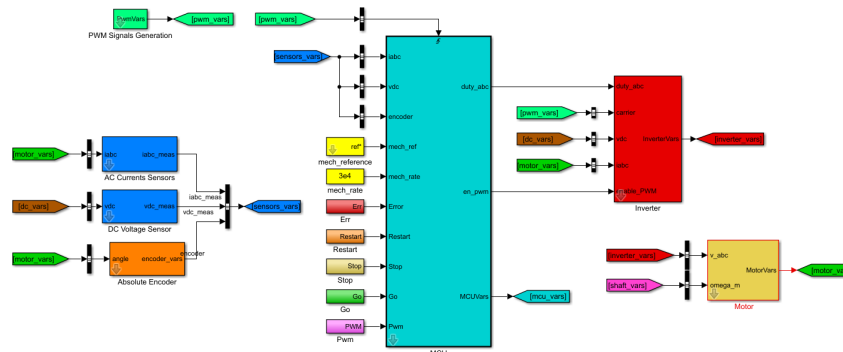


Figure 3.6: E-Drive Simulink non circuital, discrete-time average model.

The following main blocks have been implemented.

- Signal measurement with current, voltage and position sensors, (blue and orange blocks). Voltage and current sensors (blue blocks) can implement all the non-idealities often encountered in practice, e.g. offsets and channel gains. Concerning the position sensor (orange block), it emulates a real incremental encoder, thus allowing to set its resolution.
- The digital controller (light blue block) simulates the digital controller. Therefore, the motor control algorithm is implemented in this block. The developed C code has been used by means of Simulink S-function.

In addition, in this block the discretization of inputs and outputs has been implemented. In detail, both feedback and duty cycles for the converter have been discretizing using 12 bits as often happens in practice.

- The inverter (red block), receives the duty cycles and the PWM enable signals from the digital controller. The output of the inverter can consists of both PWM or average phase voltages of the motor, depending on the choice of the user. In the inverter block, non-idealities like voltage errors introduced by dead-times have been implemented.
- The motor model (light yellow block) simulates the motor under test (MUT). The inputs of this block are the phase voltages and the mechanical speed, while the main outputs consist of phase currents, mechanical torque, and rotor mechanical position. The model have been implemented in rotating (dq) coordinates using the flux maps and the inverse flux maps obtained from the magnetic model identification procedures performed on the real motor.
- The driving machine (purple block) emulates a prime mover, thus imposing the time evolution of the motor speed as desired by the user.

3.3 Voltage Behind Reactance model

The Voltage-Behind-Reactance (VBR) formulation decouples the synchronous machine model into stator and rotor subsystems. The rotor subsystem is expressed in dq rotor reference frame, with the flux linkages used as the independent variables. The rotor dynamic equations are expressed explicitly in state model form while the stator equations are described in circuit form. The model is computationally efficient and it is flexible with regard to the stator winding configuration, and it is compatible with circuit-based and differential-equation-based simulation approaches.

For this purpose some manipulation to the machine equations are necessary. Starting from 3.1, the flux derivative can be written as:

$$\frac{d\bar{\lambda}_{dq}}{dt} = \frac{\partial \bar{\lambda}_{dq}}{\partial \bar{i}_{dq}} \cdot \frac{d\bar{i}_{dq}}{dt} \quad (3.14)$$

where the partial derivative of flux with respect to current is defined as incremental inductance, thus generating inductance tensor:

$$l_{dd} = \frac{\partial \lambda_d}{\partial i_d} \quad l_{dq} = \frac{\partial \lambda_d}{\partial i_q} \quad l_{qd} = \frac{\partial \lambda_q}{\partial i_d} \quad l_{qq} = \frac{\partial \lambda_q}{\partial i_q} \quad (3.15)$$

$$[L_{inc,dq}] = \begin{bmatrix} l_{dd} & l_{dq} \\ l_{qd} & l_{qq} \end{bmatrix} \quad (3.16)$$

This incremental inductances vary with the working point according to currents. Therefore, the equation 3.1 can be written as:

$$v_{dq} = R i_{dq} + [L_{inc,dq}] \frac{d i_{dq}}{dt} + J \omega \lambda_{dq} \quad (3.17)$$

The rotational transform is applied in order to write the equation 3.17 in $\alpha\beta$ -axes:

$$v_{dq} \cdot A(-\theta) = A(-\theta)R_s i_{dq} + A(-\theta) \cdot [L_{inc,dq}] \frac{di_{dq}}{dt} + A(-\theta) \cdot J\omega\lambda_{dq} \quad (3.18)$$

$$v_{\alpha\beta} = R_s i_{\alpha\beta} + A(-\theta) \cdot [L_{inc,dq}] \frac{di_{dq}}{dt} + A(-\theta) \cdot J\omega\lambda_{dq} \quad (3.19)$$

Considering only the second term, characterized by the current derivative, it can be transformed in:

$$\begin{aligned} A(-\theta) \cdot [L_{inc,dq}] \frac{d}{dt} i_{dq} &= A(-\theta) \cdot [L_{inc,dq}] \frac{d}{dt} (A(\theta)) \cdot i_{\alpha\beta} = \\ &= A(-\theta) \cdot [L_{inc,dq}] \cdot A(\theta) \frac{d}{dt} i_{\alpha\beta} + A(-\theta) \cdot [L_{inc,dq}] \frac{d}{dt} (A(\theta)) i_{\alpha\beta} \end{aligned} \quad (3.20)$$

The first part is equivalent to the tensor of incremental inductance in $\alpha\beta$ -axes as shown in 3.21.

$$[L_{inc,\alpha\beta}] = A(-\theta) \cdot [L_{inc,dq}] \cdot A(\theta) \quad (3.21)$$

Each component of this tensor can be calculated as:

$$[L_{inc,\alpha\beta}] = \begin{bmatrix} l_{\alpha\alpha} & l_{\alpha\beta} \\ l_{\beta\alpha} & l_{\beta\beta} \end{bmatrix} = \begin{bmatrix} \cos(\theta) & -\sin(\theta) \\ \sin(\theta) & \cos(\theta) \end{bmatrix} \cdot \begin{bmatrix} l_{dd} & l_{dq} \\ l_{qd} & l_{qq} \end{bmatrix} \cdot \begin{bmatrix} \cos(\theta) & \sin(\theta) \\ -\sin(\theta) & \cos(\theta) \end{bmatrix} \quad (3.22)$$

$$\begin{aligned} l_{\alpha\alpha} &= l_{dd} \cos^2(\theta) + l_{qq} \sin^2(\theta) - 2l_{dq} \cos(\theta) \sin(\theta) \\ l_{\alpha\beta} &= l_{dq} (\cos^2(\theta) - \sin^2(\theta)) + l_{dd} \cos(\theta) \sin(\theta) - l_{qq} \cos(\theta) \sin(\theta) \\ l_{\beta\beta} &= l_{qq} \cos^2(\theta) + l_{dd} \sin^2(\theta) + 2l_{dq} \cos(\theta) \sin(\theta) \end{aligned} \quad (3.23)$$

Taking into account that:

$$\begin{aligned} \cos(2\theta) &= \cos^2(\theta) - \sin^2(\theta) = 1 - 2\sin^2(\theta) = 2\cos^2(\theta) - 1 \\ \sin(2\theta) &= 2\cos(\theta) \sin(\theta) \end{aligned} \quad (3.24)$$

Substituting in 3.23, the tensor of incremental inductances in $\alpha\beta$ -axes can be written as:

$$[L_{inc,\alpha\beta}] = \begin{bmatrix} l_{avg} + l_{\Delta} \cos(2\theta) - l_{dq} \sin(2\theta) & l_{dq} \cos(2\theta) + l_{\Delta} \sin(2\theta) \\ l_{dq} \cos(2\theta) + l_{\Delta} \sin(2\theta) & l_{avg} - l_{\Delta} \cos(2\theta) + l_{dq} \sin(2\theta) \end{bmatrix} \quad (3.25)$$

where:

$$l_{avg} = \frac{l_{dd} + l_{qq}}{2} \quad l_{\Delta} = \frac{l_{dd} - l_{qq}}{2} \quad (3.26)$$

Returning back to 3.20, the second term can be evaluated calculating the derivative of the rotational transform matrix:

$$\frac{d}{dt} (A(\theta)) = -\omega \begin{bmatrix} \sin(\theta) & -\cos(\theta) \\ \cos(\theta) & \sin(\theta) \end{bmatrix} \quad (3.27)$$

where ω is the electrical rotational speed.

$$A(-\theta) \cdot [L_{inc,dq}] \frac{d}{dt} (A(\theta)) i_{\alpha\beta} = A(-\theta) \cdot [L_{inc,dq}] (-\omega) \begin{bmatrix} \sin(\theta) & -\cos(\theta) \\ \cos(\theta) & \sin(\theta) \end{bmatrix} i_{\alpha\beta} \quad (3.28)$$

Considering that $i_{\alpha\beta} = A(\theta)i_{dq}$, it is possible to write 3.28 as:

$$A(-\theta) \cdot [L_{inc,dq}](-\omega) \begin{bmatrix} \sin(\theta) & -\cos(\theta) \\ \cos(\theta) & \sin(\theta) \end{bmatrix} \begin{bmatrix} \cos(\theta) & -\sin(\theta) \\ \sin(\theta) & \cos(\theta) \end{bmatrix} i_{dq} = A(-\theta) \cdot [L_{inc,dq}](-\omega) J i_{dq} \quad (3.29)$$

Therefore, the stator equation $\alpha\beta$ -axes are written as:

$$\begin{aligned} v_{\alpha\beta} &= R_s i_{\alpha\beta} + [L_{inc,\alpha\beta}] \frac{di_{\alpha\beta}}{dt} + A(-\theta) \cdot [L_{inc,dq}](-\omega) J i_{dq} + A(-\theta) \cdot J \omega \lambda_{dq} = \\ &= R_s i_{\alpha\beta} + [L_{inc,\alpha\beta}] \frac{di_{\alpha\beta}}{dt} + A(-\theta) \cdot [[L_{inc,dq}](-\omega) J i_{dq} + J \omega \lambda_{dq}] \end{aligned} \quad (3.30)$$

The last term in brackets is equivalent to the electromotive force in dq -axes, which multiplied for the rotational transform $A(\theta)$, is equal to the electromotive force in $\alpha\beta$ -axes:

$$e_{\alpha\beta} = A(-\theta) \cdot [[L_{inc,dq}](-\omega) J i_{dq} + J \omega \lambda_{dq}] \quad (3.31)$$

$$v_{\alpha\beta} = R_s i_{\alpha\beta} + [L_{inc,\alpha\beta}] \frac{di_{\alpha\beta}}{dt} + e_{\alpha\beta} \quad (3.32)$$

In order to transform equation 3.32 in abc frame, the inverse Park transform $[T]^{-1}$ is applied:

$$[T]^{-1} \cdot v_{\alpha\beta} = R_s [T]^{-1} \cdot i_{\alpha\beta} + [T]^{-1} \cdot [L_{inc,\alpha\beta}] \frac{di_{\alpha\beta}}{dt} + [T]^{-1} \cdot e_{\alpha\beta} \quad (3.33)$$

Consequently, the equation 3.33 is equal to:

$$v_{abc} = R_s i_{abc} + [T]^{-1} \cdot [L_{inc,\alpha\beta}] \frac{di_{\alpha\beta}}{dt} + e_{abc} \quad (3.34)$$

Taking in account that $i_{\alpha\beta} = [T] \cdot i_{abc}$ and the Park transform is time-independent, the previous equation can be written as:

$$v_{abc} = R_s i_{abc} + [T]^{-1} \cdot [L_{inc,\alpha\beta}] [T] \frac{di_{abc}}{dt} + e_{abc} \quad (3.35)$$

where

$$L_{abc} = \begin{bmatrix} l_{aa} & l_{ab} & l_{ac} \\ l_{ba} & l_{bb} & l_{bc} \\ l_{ca} & l_{cb} & l_{cc} \end{bmatrix} = [T]^{-1} \cdot [L_{inc,\alpha\beta}] \cdot [T] \quad (3.36)$$

In order to evaluate this product among matrices the tensor of incremental inductances in $\alpha\beta$ -axes must have three rows and three columns, thus one row and column of zeros have been added to it. Therefore, the terms of the tensor of incremental inductances are equivalent to:

$$\begin{aligned}
 l_{aa} &= \frac{2}{3}l_{\alpha\alpha} \\
 l_{ab} = l_{ba} &= \frac{1}{3} \left[-l_{\alpha\alpha} + \sqrt{3}l_{\alpha\beta} \right] \\
 l_{ac} = l_{ca} &= \frac{1}{3} \left[-l_{\alpha\alpha} - \sqrt{3}l_{\alpha\beta} \right] \\
 l_{bb} &= \frac{1}{3} \left[\frac{l_{\alpha\alpha}}{2} + \frac{3}{2}l_{\beta\beta} - \sqrt{3}l_{\alpha\beta} \right] \\
 l_{bc} = l_{cb} &= \frac{1}{3} \left[\frac{l_{\alpha\alpha}}{2} - \frac{3}{2}l_{\beta\beta} \right] \\
 l_{cc} &= \frac{1}{3} \left[\frac{l_{\alpha\alpha}}{2} + \frac{3}{2}l_{\beta\beta} + \sqrt{3}l_{\alpha\beta} \right]
 \end{aligned} \tag{3.37}$$

Moreover, it is possible to add the contribution of leakage inductances to the equation 3.35, obtaining:

$$v_{abc} = R_s i_{abc} + L_{ls} \frac{di_{abc}}{dt} + [L_{inc,abc}] \frac{di_{abc}}{dt} + e_{abc} \tag{3.38}$$

In contrast to the tensor of incremental inductances, the leakage inductances are not variable.

Considering the equation 3.38, the equivalent circuit for the electric machine is the following:

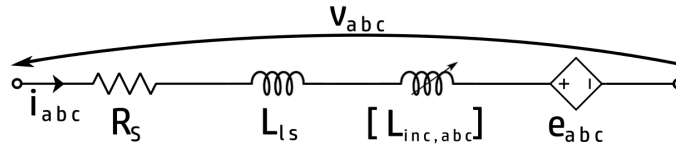


Figure 3.7: Equivalent circuit for the electric machine with the VBR model.

The circuit is an electric equivalent of the electrical machine, thus mechanical behaviour is not considered. For this reason the torque is evaluated through equation 3.10, utilising fluxes coming from LUT and currents measured.

In order to replicate this circuit (Figure 3.7) in Simscape Simulink the block "Simscape Component" is necessary. It is employed to model the back-emf in *abc*-frame, the stator resistances, the leakage inductances and the matrix of incremental inductances in *abc*-frame all in one component.

3.3.1 Simscape Component

The Simscape Component block lets the user generate a Simscape block directly from a textual component file, skipping the library build process. The symbol of this block is:



Figure 3.8: Simulink symbol for the Simscape component block.

As it is possible to notice, it has no specification because a component file has not been deployed in it yet. In order to do this, a file with the *.ssc* has to be created and filled

with the code necessary to make the block follow the desired behaviour. In this case, this block is utilized to model the stator resistor, the leakage stator inductor, the back-emf in *abc*-frame and the matrix of incremental inductances. The first three elements can be model using standard blocks, while for the third one there is not a suitable block. This block should behave as a three-phase inductor, with auto mutual coupling, and there should be the possibility to give as input the inductances values because they are variable currents. Because of this, a personal code has been developed to simulate this behaviour and inserted in the Simscape component. This code is divided in different parts that perform different tasks:

1. Definition of nodes:

```
nodes
    pa_in= foundation.electrical.electrical; % a:left
    pb_in= foundation.electrical.electrical; % b:left
    pc_in= foundation.electrical.electrical; % c:left
    pa_out= foundation.electrical.electrical; % a:right
    pb_out= foundation.electrical.electrical; % b:right
    pc_out= foundation.electrical.electrical; % c:right
end
```

In this section the input and output nodes are defined. All of these nodes are defined as electrical ones in order to be connected to other Simscape blocks of the same type. Since it is a three-phase element there are three input nodes and three output ones. The final comments in green are still part of the code and they are used to place physically the nodes on the block mask.

2. Definition of inputs:

```
inputs
    L= {[0 0 0 0 0 0 0 0 0], 'H'}; % L:left
    Ldisp= {0, 'H'}; % Lls:left
    R= {0, 'Ohm'}; % R:left
    E={ [0 0 0], 'V'}; % Eabc:left
end
```

In this part the variables that are given as logic input are defined. The logic input is a port as the electrical one but is employed to insert in the block the parameter necessary for equations. Firstly the tensor of inductances is defined and it is given as a vector of nine elements. Then the leakage inductances and the resistance are defined as single values. Finally the back-emf in *abc*-frame, calculated starting from equation 3.31 and then transformed in *abc*-frame. Moreover the initial value and the unit of measurement are defined for every inputs. Again the final comments in green are used to place physically the input logic ports.

3. Definition of variables:

```
variables
    ia= {0, 'A'}; % Current phase a
    ib= {0, 'A'}; % Current phase b
    ic= {0, 'A'}; % Current phase c
    va= {0, 'V'}; % Voltage phase a
    vb= {0, 'V'}; % Voltage phase b
    vc= {0, 'V'}; % Voltage phase c
end
```

In this section the variables used in the equations inside the block are defined. They are the currents flowing the three branches and the voltage drops across the three elements modelled. There is the possibility to define their unit of measurement and set their initial values through the block mask.

4. Definition of branches:

```
branches
    ia: pa_in.i ->pa_out.i; % Current phase a through
        from node pa_in to node pa_out
    ib: pb_in.i ->pb_out.i; % Current phase b through
        from node pb_in to node pb_out
    ic: pc_in.i ->pc_out.i; % Current phase c through
        from node pc_in to node pc_out
end
```

In this portion of code the path of currents is defined. In this case there are not particular necessities thus every phase current flows from the own input node to the respective output one.

5. Definition equations:

```
equations
    va== pa_in.v-pa_out.v;
    vb== pb_in.v-pb_out.v;
    vc== pc_in.v-pc_out.v;
    va== L(1)*ia.der+L(2)*ib.der+L(3)*ic.der+Ldisp*ia.der
        +R*ia+E(1);
    vb== L(4)*ia.der+L(5)*ib.der+L(6)*ic.der+Ldisp*ib.der
        +R*ib+E(2);
    vc== L(7)*ia.der+L(8)*ib.der+L(9)*ic.der+Ldisp*ic.der
        +R*ic+E(3);
end
```

In this final part equation that regulate the block behaviour are defined. As it is possible to notice they are based on 3.35 equation.

The final aspect of the block Simscape component, after having deployed the personal code in it, is the following:

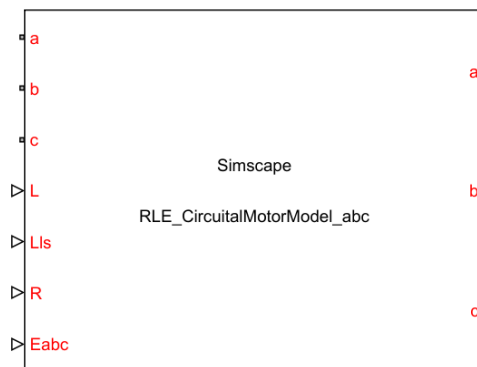


Figure 3.9: Simulink symbol for the personalised Simscape component block.

3.3.2 Block selection and evaluation

In order to evaluate this built model, it has been compared to an equal and tested model built in another simulation tool: PLECS. It has been done a comparison test using the same flux maps for the two simulation tools.

The comparison is done observing the a -phase current. The currents obtained are the following:

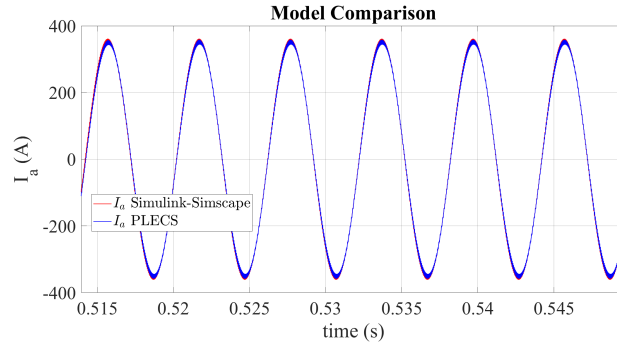


Figure 3.10: Current of phase a in the motor test.

The results obtained are in line with the expected one. Furthermore, the results of the two simulation tools are exactly the same, apart from slight differences caused by the different solver, as it is possible to notice in Figure 3.11.

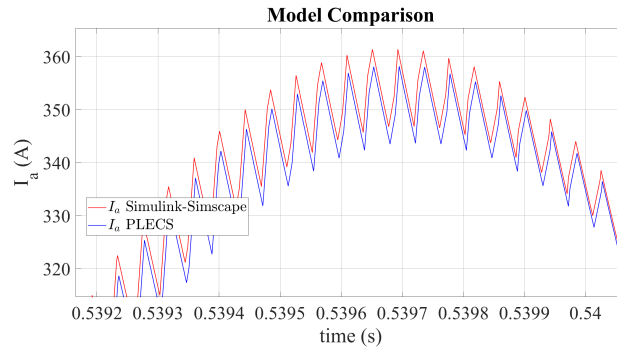


Figure 3.11: Detail of current of phase a in the motor test.

Chapter 4

Torque Control Strategies for E-motors

The next step of this thesis consist in the development of the torque control for the e-Motor and starts with the study of the actual state of art of control strategies of traction motors. In the optic of the torque control of e-Motors, the e-Motor for a traction e-Drive can be seen as a torque generator, the speed response depends on the vehicle. The torque control is implemented by the MCU (Motor Control Unit).

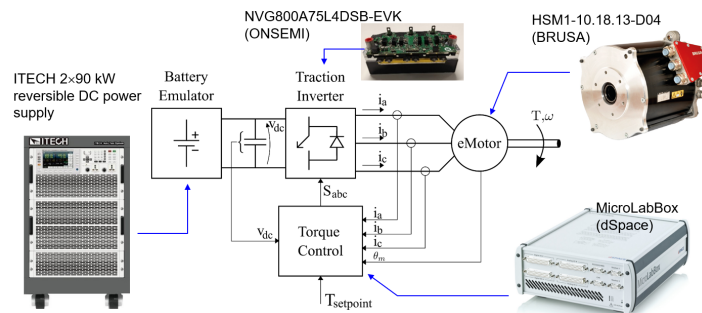


Figure 4.1: Powertrain scheme.

Figure 4.1 shows the scheme of a powertrain for an electric vehicle. At every block is associated its real component used in the testing platform. The parameters of the defined inverter and motor are taken as reference in the models used in the simulations.

Starting from a torque external reference T_m^* and using electrical and mechanical feedback, the MCU generates proper commands for the power converter using a torque control algorithm. All 3-phase AC motor drives (IM and Synchronous) fall under the scope of variable-frequency vector control. Several control algorithms can be adopted:

- Ac Motor Control
 - Scalar Control $\rightarrow \mathbf{V/f}$
 - Vector Control
 - * Open Loop $\rightarrow \mathbf{I-f}$
 - * Closed Loop
 - **FOC**
 - **DFVC**
 - **DTC**

We will focus on closed loop algorithm. All the vector control techniques are different methods to obtain the desired torque from the AC motor drive (torque control). The

torque control strategy depends on the e-motor type and normally requires the knowledge of machine electrical and magnetic parameters (e.g inductance, resistance, PM flux,...), so Motor modelling is necessary. The torque control loop generates the reference voltages v_{abc}^* following the desired T^* , they are the digital signals computed by the motor control algorithm. The Voltage Source Inverter (VSI) converts the v_{abc}^* into the correspondent phase voltages v_{abc} that are the phase voltages physically imposed to the motor by the inverter. The VSI generates the phase voltages following the desired one. The non-ideal behaviour of this voltage actuator must be taken into account properly in the development of the control code to compensate for the voltage error introduced. The inverter can be seen as a voltage actuator.

If a speed control is required an outer controller (speed loop) is added in cascade to the torque control loop.

- The speed control defines the torque T^* required to obtain the desired w^* = reference mechanical speed.
- A further outer controller (position loop) may be added in cascade if position control is required

The drives for electrical vehicles are always torque controlled because T^* is directly set by the user acting on the accelerator pedal.

The state of the art of the torque control strategies available in the literature is now presented.

4.1 DTC

Direct torque control (DTC) is of great interest for motor drives because of its simplicity, independence of motor parameters, high reliability and improved dynamic response. However, the main disadvantage of DTC is the large flux and torque ripple compared to FOC. Another disadvantage of traditional DTCs is that the inverter switching frequency is not constant, it varies with load torque, rotor speed, and hysteresis controller bandwidth. Many attempts have been made to overcome these limitations.

Direct selection of stator voltage vectors in accordance with discrepancies between reference and real torque and stator flux linkage is the fundamental tenet of DTC. The characteristics of the motor, with the exception of the stator resistance, are not employed in DTC systems, nor is the current controller followed by a pulse width modulation (PWM) comparator.

Synchronous Motors are used in many applications that require rapid torque response and high-performance operation. For high performance, the current control is normally executed in the rotor dq reference frame that rotates with the synchronous speed. In this frame, the armature inductances and magnet flux linkage are constant if the back Electro-Motive Force (EMF) and variation of inductances are sinusoidal. With the appearance of high-speed digital signal processor a control methods called direct torque control has become popular in electrical motor drives.

4.1.1 Control of Stator Flux Linkage by Selecting the Proper Stator Voltage Vector

By maintaining the stator flux linkage's amplitude constant and accelerating its rotation as quickly as feasible, the variation in torque can be managed. By choosing the appropriate stator voltage vectors, it is possible to regulate the amplitude and rotational speed of the stator flux linkage. When the primary windings are fed by an inverter, the primary voltages v_a, v_b and v_c are determined by the status of the three switches S_a, S_b and S_c . v_a is connected to V_{dc} if S_a is one, otherwise is connected to zero, similar for v_b and v_c . Therefore there are six non-zero voltage vectors and two zero voltage vectors. The

six non-zero voltage vectors are 60° apart from each other as in Figure 4.2. These eight voltage vectors can be expressed as:

$$v_s(S_a, S_b, S_c) = \frac{2}{3}V_{dc}(S_a + S_b e^{j(2/3)\pi} + S_c e^{j(4/3)\pi}) \quad (4.1)$$

where V_{dc} is the dc-link voltage and $2/3$ is the factor of Park Transformation.

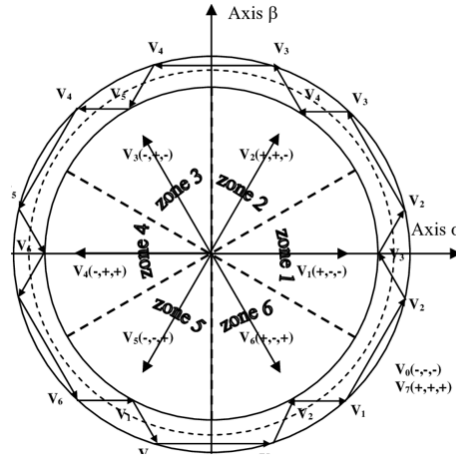


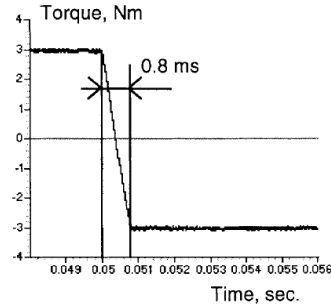
Figure 4.2: Control of the stator flux linkage[1].

Figure 4.2 shows also how to select the voltage vectors for controlling the amplitude of the stator flux linkage (φ_s), the voltage vector plane is divided into six regions. In each region, two adjacent voltage vectors, which give the minimum switching frequency, are selected to increase or decrease the amplitude of φ_s , respectively. In this way, φ_s can be controlled to be kept within a hysteresis band when it is rotating counter-clockwise direction.

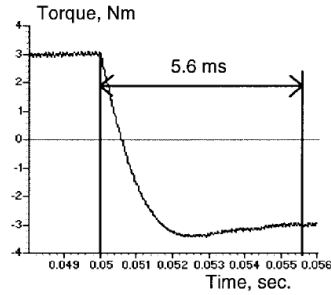
If the actual torque for counterclockwise operation is less than the reference torque, the voltage vectors that maintain φ_s rotating in the same direction are chosen. Both the angle and the actual torque rise as quickly as they can. The voltage vectors that maintain φ_s rotating in the opposite direction are chosen in place of the zero voltage vectors after the actual torque exceeds the reference. The torque similarly diminishes as the angle δ does. By choosing the voltage vectors in this manner, φ_s is rotated continuously, and the output of the hysteresis controller for the torque determines the rotational direction of φ_s . The reference torque is limited at a certain value with respect to a given reference flux linkage, which guarantees the stator current not to exceed the limit value.

The simulation results obtained in [1] reveal one important difficulty in implementing the DTC for the PMSM. If the stator flux linkage φ_s is small, as in the case with low-voltage, high-speed motors, the low value of stator flux linkage implies that the sampling interval must be very small. With DTC, the stator voltage vector changes every sampling time instead of every switching time as in PWM current-controlled drive. If the sampling interval is not small enough, the change of flux linkage in each sampling time will exceed the bandwidth of the hysteresis controller.

As shown in Figure 4.3 the torque response with DTC is seven time faster than with current control.



(a)



(b)

Figure 4.3: Torque responses with DTC and current control: (a) torque response under DTC and (b) torque response under PWM current control in the rotor reference frame[1].

4.1.2 Flux-Weakening Algorithm

At low speeds, electrical drives must produce a constant torque, but middle and high speeds call for a torque reduction at a constant power. It is crucial to choose the flux reference and base speed (the speed that corresponds to the start of the flux-weakening process). Due to the inverter current limit, lowering the flux reference below the ideal level causes a roughly proportionate fall in the torque capacity. On the other hand, increasing the flux reference level too much causes the back-emf value to rise. Because of this, the maximum current for a predetermined DC-link voltage cannot be reached, and the torque capability may once again decline.

In flux-weakening operation of DTC the flux reference is adjusted on the basis of the torque error behaviour. The flux-weakening scheme proposed in [2] self-regulates the stator flux reference without the need of machine parameters, allowing a satisfying operation in the whole speed range.

The DTC method commonly uses direct configurations and zero vectors to keep the torque within the hysteresis band in the high speed range when the motor back emf is less than the stator voltage limit. The zero vectors are employed when the torque need is met, but the direct configurations are used to increase the torque. Due to its inherent qualities, the DTC algorithm prioritizes flux tracking over torque tracking in the high speed range. The flux still stays inside the corresponding hysteresis band as the back emf approaches the stator voltage limit, but the torque demand might not be met. In this instance, the DTC algorithm repeatedly fails to drive the torque inside the hysteresis zone, causing the torque to fall.

In other words, the DTC algorithm continuously tries to raise the torque by direct setups, but it fails. Based on the foregoing factors, it may be possible to determine whether the motor is approaching the base speed, or the speed corresponding to the start of the flux weakening zone, by performing a proper analysis of the output of the torque hysteresis comparator. An important factor in establishing whether or not the motor is inside the flux-weakening area is the frequency of successive direct voltage vector applications. A N-cycle analysis of the motor behavior is performed. The control algorithm considers that the flux level is too high for the actual operating circumstances if

the output of the torque hysteresis comparator is always one throughout this time frame, meaning that only active vectors are supplied to the motor and the torque demand is never met. The flux reference is then somewhat reduced after that. The torque demand is fulfilled and the control algorithm tries to enhance the flux reference if, on the other hand, the DTC algorithm applies at least one zero or inverse configuration over the N cycle periods. Finding the highest flux level that guarantees the torque instruction is carried out is the fundamental tenet of the control algorithm. Of course, the flux cannot become lower than a minimum value or greater than the rated value.

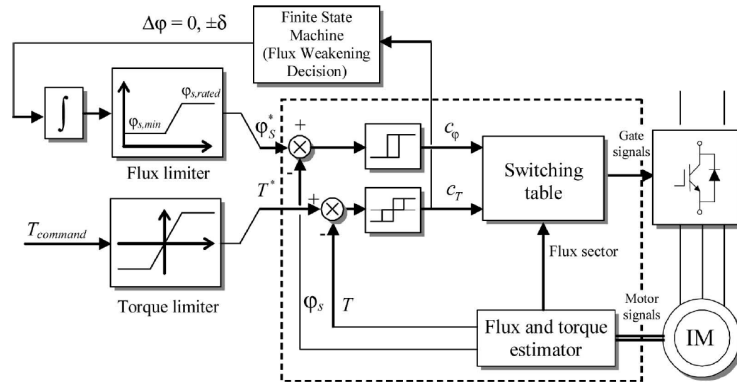


Figure 4.4: DTC scheme with flux weakening[2].

These basic principles ensure the correct control of the flux reference over the whole speed range and also a smooth transition between the constant flux region and the flux-weakening region, without the need of flux reference calculations and knowledge of the parameters.

Figure 4.5 shows the experimental results obtained in [2] where a transient from 75% up to 400% of the base speed has been considered during experimental tests. As the torque reference exceeds the maximum torque, the torque request cannot be satisfied, and the estimated torque rapidly decreases. The flux weakening algorithm reduces the flux reference, without improvements in the torque behaviour. As consequence, also the estimated torque decreases. Once the maximum torque is determined during the first transient, the drive is perfectly tuned, and the estimation algorithm is no more used.

The experimental results obtained in [3] show that the torque and stator flux ripple is small noticeably. This ripple level is drastically reduced when compared with the previous works.

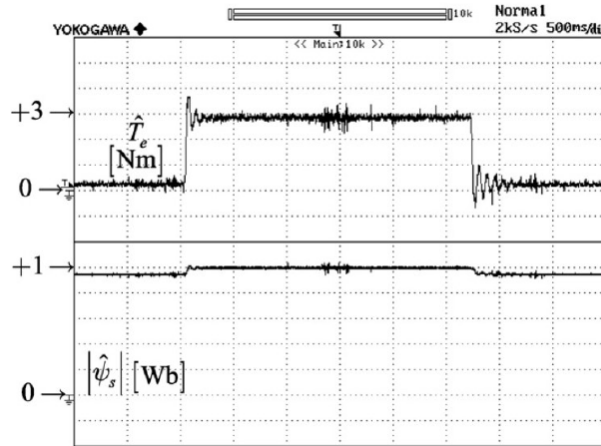


Figure 4.7: Estimated torque response and stator flux amplitude when step load torque change from no-load to full load (0-2.6Nm)[3].

The Figure 4.7 shows the torque transient during step load changes from no load to full load and from full load to no load. The stator flux amplitude changes little, as can be observed. The rapid reaction is maintained while the predicted torque ripple is considerably minimized. This method has a lot of benefits, including less torque ripple, less flux droop during sector changes, no issues when operating at low speeds, simple control with just one PI torque controller, decoupling operation between stator flux amplitude and stator flux angle, and constant switching frequency. However, as this method depends on an exact rotor speed measurement, a high resolution speed measurement is necessary.

4.2 FOC

In comparison to DTC, Field Oriented Control (FOC) gives better dynamic control. Additionally, the voltages, currents, and magnetic flux space vectors' amplitude, location, and frequency may all be adjusted. High-speed operation is compatible with FOC, and sensorless control can be used. Comparing FOC to DTC methods, torque ripple is decreased. The control method is dependent on the motor's parameters and speed, reducing the robustness of the control mechanism. However, it necessitates computationally intensive online transformations and calculations.

4.2.1 Look-Up Table Computation

When controlling PMSM using FOC, the torque reference is chosen based on the machine speed, using the Maximum Torque per Ampere (MTPA) for low speed values and the (Maximum Torque per Volt) MTPV for high speed values. A function of the reference torque and operating speed should be used to identify the best current (or flux linkage) references for this purpose. The look-up tables (LUTs) produced by this computation are normally performed offline and then used in the online control approach.

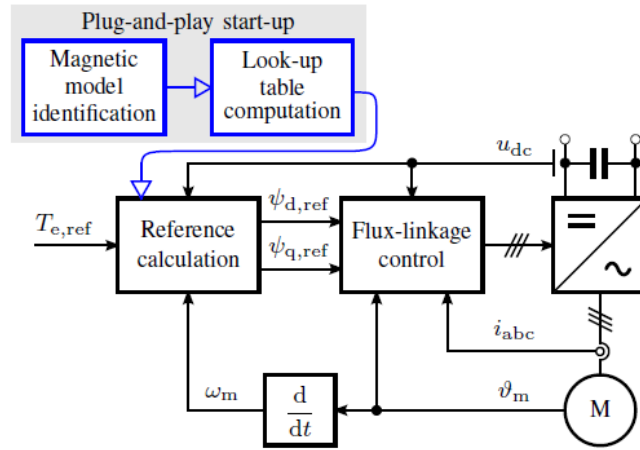


Figure 4.8: Plug-and-Play start up method[4].

A plug-and-play method for the optimal torque control of synchronous motor is presented in [4]. The overall structure of the proposed approach is shown in Figure 4.8. The proposed look-up table computation method can run in the embedded processor of the drive during the start-up, after the magnetic model of the motor has been identified.

Control Scheme

The torque reference is the input to a look-up table whose output is the ideal MTPA flux magnitude. The highest available voltage is used to restrict the MTPA flux, producing the ideal flux magnitude under the voltage limitation. The observed DC-link voltage is used to compute the maximum voltage. The torque T_{max} corresponding to the total MTPV and current limit limits the torque reference, resulting in the limited torque reference. The look-up table, whose input is the ideal flux magnitude, is used to read the maximum limit, T_{max} . Based on the ideal reference $\varphi_{s,ref}$ and torque reference, $\varphi_{d,ref}$ is calculated using a two-dimensional look-up table. The Pythagorean theorem may be used to determine the value of the q-axis flux component $\varphi_{q,ref}$ from the interpolated result $\varphi_{d,ref}$. Finally, if needed, the flux references can be transformed into the current references using the algebraic magnetic model.

Computation method is divided into four stages:

MTPA For creating a look-up table, a list of L equally-spaced current magnitudes is defined. For each current magnitude i_s , the maximum torque T_{mtpa} and the corresponding argument $i_{d,mtpa}$ are obtained by solving the optimization problem:

$$T_{mtpa} = \max_{i_d \in [-i_s, 0]} T_e(i_d) \quad (4.2)$$

where the torque is expressed as a function of i_d :

$$T_e(i_d) = \frac{3}{2} p [\varphi_d(i_d, i_q) \cdot i_q(i_d) - \varphi_q(i_d, i_q) \cdot i_d] \quad (4.3)$$

$$i_q(i_d) = \sqrt{i_s^2 - i_d^2} \quad (4.4)$$

and the search interval is $-i_s \leq i_d \leq 0$. The flux components φ_d and φ_q corresponding to i_d and i_q are calculated by numerically inverting the algebraic magnetic model. The procedure is repeated in a loop for each element of the list. The inputs for the MTPA computation stage are the number of points L to be computed, the maximum current $i_{s,max}$ and the parameters of the magnetic model.

MTPV For creating the look-up table, a list of M equally-spaced stator flux magnitudes is defined, where the maximum flux magnitude $\varphi_{s,max} = \varphi_{s,mtpv}(L)$ is the result from the last step of the MTPA computation. For each flux magnitude φ_s , the maximum torque T_{mtpv} is obtained by solving:

$$T_{mtpv} = \max_{\varphi_d \in [-\varphi_s, 0]} T_e(\varphi_d) \quad (4.5)$$

where the torque is expressed as

$$T_e(\varphi_d) = \frac{3}{2} p [\varphi_d \cdot i_q(\varphi_d, \varphi_q) - \varphi_q(\varphi_d) \cdot i_d(\varphi_d, \varphi_q)] \quad (4.6)$$

$$\varphi_q(\varphi_d) = \sqrt{\varphi_s^2 - \varphi_d^2} \quad (4.7)$$

It is highlighted that no magnetic model inversion is needed in this stage. The problem is solved for each element $\varphi_s(m)$ of the list.

Maximum Current Limit The already defined input list of the flux magnitudes is considered. For each flux magnitude $\varphi_s(m)$, the d-component $\varphi_{d,lim}$ of the flux corresponding to the maximum current $i_{s,max}$ is solved

$$\varphi_{d,lim} = \underset{\varphi_d \in [\varphi_{d,mtpv}, \varphi_{d,max}]}{\text{solve}} \{i_s^2(\varphi_d) = i_{s,max}^2\} \quad (4.8)$$

After 4.8 has been solved, the corresponding torque T_{lim} is obtained from 4.6.

The MTPV and current limit can be easily merged into one limit

$$T_{max} = \min(T_{mtpv}, T_{lim}) \quad (4.9)$$

Two-Dimensional Reference Look-Up Table For given flux magnitude and torque reference the d-component $\varphi_{d,ref}$ is solved

$$\varphi_{d,ref} = \underset{\varphi_d \in [\varphi_{d,mtpv}, \varphi_s]}{\text{solve}} \{T_{e,ref} = T_e(\varphi_d)\} \quad (4.10)$$

For creating the look-up table equation 4.10, can be solved in two nested *for* loops. As an input to one loop the list of the flux magnitudes $\varphi_s(m)$ is used. In the other loop, the already calculated MTPV torque values can be used as an input $T_{e,ref}(n) = T_{mtpv}(m)$. This selection not only defines the maximum torque which can be generated (under the MTPV limit) but also explicitly gives the lower bound $\varphi_{d,mtpv}$ for each $\varphi_{d,ref}$. If the maximum current is fixed $T_{e,ref}(n) = T_{max}(m)$ can be used instead. The look-up table for the control system is created from the resulting table $\varphi_{d,ref}(m, n)$.

This approach may be applied in the drive's commissioning phase and has to be used once throughout the entire drive's lifespan. It is emphasized how crucial it is to factor in magnetic saturation when determining the state reference. After the references have been determined, the magnetic saturation cannot be taken into account. Constant inductances would cause the voltage ellipses and torque hyperbolas to distort, leading to a selection of non-ideal working locations. Calculating the state references using the suggested approach correctly accounts for magnetic saturation.

Figures 4.9 and 4.10 show the results obtained in [4].

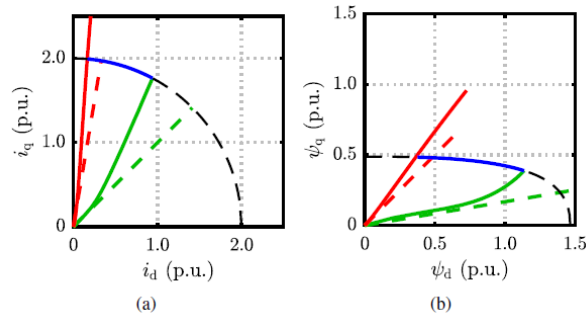


Figure 4.9: MTPA, MTPV, and current limit control trajectories: (a) $i_d - i_q$ plane (b) $\psi_d - \psi_q$ plane. The dashed lines show the results when the magnetic saturation is not taken into account (inductances correspond to the rated operating point). the black dashed curve corresponds to the constant current circle[4].

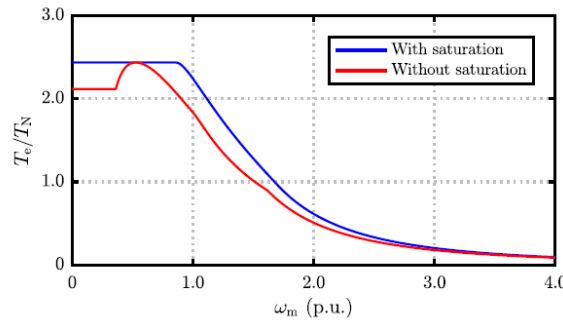


Figure 4.10: Torque vs speed curve generated from the reference calculation block with and without taking magnetic saturation into account[4].

4.2.2 Torque Control Strategies based on LUTs

One of the most used torque control solutions is Look-up-Table (LUT) based Field Oriented Control (FOC). These methods involve little computing effort and are quite easy to apply. However the LUT approach has the following drawbacks:

- LUTs can require a relatively high amount of memory, depending on their size and number of dimensions.
- Machine electric parameters may vary due to manufacturing tolerances, machine ageing or temperature variations. Thus, the torque control may be affected by irregularities and unconsciousness during operation, leading to possible instabilities in the Field Weakening (FW) region.

In order to assure controllability under electrical parameter variations and/or resolver offset determination mistakes, a solution must be found. In order to guarantee that the system stays within the maximum voltage restriction in the field weakening zone, two innovative Voltage-Constraint-Tracking (VCT) based feedback techniques are provided in [5].

Due to inverter ratings and available DC-link voltage restrictions, synchronous motor drives are subject to speed and torque limitations. This constraints can be represented with the following mathematical expressions:

$$\sqrt{i_d^2 + i_q^2} \leq I_{max} \quad (4.11)$$

$$L_d^2(i_d + \frac{\varphi_{pm}}{L_d})^2 + L_q^2 i_q^2 \leq (\frac{V_{max}}{w_e})^2 \quad (4.12)$$

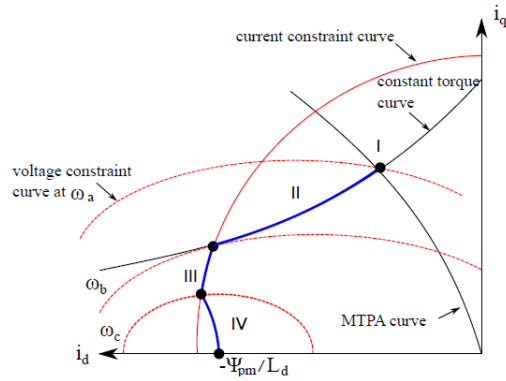
The current limit curve produces a circumference of radius I_{max} in the stator current dq plane. Similarly, the voltage constraint, produces ellipses whose radius decreases when the electrical machine speed increases. The machine must be controlled such as the dq plane current vector lies simultaneously within the current constraint circumference and voltage constraint ellipse. According to this constraints and considering an arbitrary torque inferior to the maximum one, four operation regions can be distinguished (4.11)

MTPA Ensures a maximum torque per applied current modulus. Minimum ohmic losses are obtained if this curve is tracked.

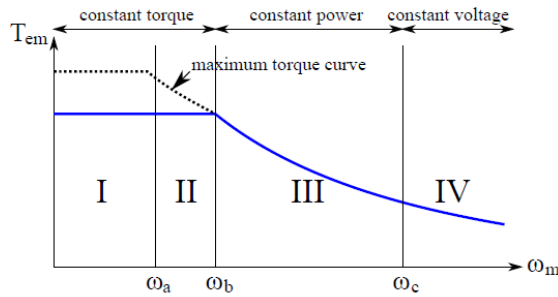
Field weakening region without torque reduction In order to extend the speed operation region, the control strategy consists of reducing the i_d current. In a given region, this is achieved without losing torque capability, as i_q^* can be recalculated to maintain the reference torque. This region can be extended until the speed w_b is reached, where the speed and current limit curves intersect with each other.

Field weakening region with torque reduction When current constraint circumference is reached, the torque capability is reduced in field weakening operation. In order to achieve maximum torque in this region the current set point vector must be positioned in the intersection between the voltage and current constraint curves.

MTPV The torque production capability is maximized for a constant stator voltage value. The MTPV region exists only for a given IPMSM if $\varphi_{pm}/L_d \leq I_{max}$ condition is fulfilled, and can be mathematically determined.



(a) Optimal trajectory of the stator currents in the dq plane taking into account the current and voltage constraints



(b) IPMSM optimum operation region for an arbitrary torque $T_{em} < T_{em,max}$: MTPA (I), field weakening (II), field weakening with torque reduction (III), MTPV (IV)

Figure 4.11: IPMSM optimal control trajectories and regions[5].

VCT Feedback Strategies

The field weakening and MTPV areas might become unstable in LUT-based control schemes because the current trajectories contained in these LUTs depend on a specific set of electric machine characteristics. In order to mitigate these parameter uncertainties, it is interesting to integrate an online field weakening control loop. The proposed control strategies reported in [5] are composed of two main blocks:

- **Speed normalization block, including security margin:** The speed is normalized in order to avoid the dependance between the LUTs and the DC-link voltage variations. An addition security margin is applied multiplying the measured $V_{dc}/\sqrt{3}$ by a parameter k_v (in per unit), that is chosen to ensure that the voltage limit is never reached.
- **VCT Field weakening block:** The normalized speed is controlled according to the actual value of the stator voltage (Vs) and the DC-link voltage multiplies by the security margin k_v . Instead of using a PI controller, whose gain adjustment is not straightforward, two VCT solutions have been adopted:
 - Flowchart based normalized speed control
 - Integration based normalized speed control

The VCT strategies aim to maintain the operating point close to the voltage limit in both FW and MTPV regions. A parameter defining the VCT voltage error, Δ_v , is included in

both methods:

$$\Delta_v = \frac{V_{DC}k_v}{\sqrt{3}} - V_s \quad (4.13)$$

where V_s is the actual value of the stator voltage, commanded by the inverter.

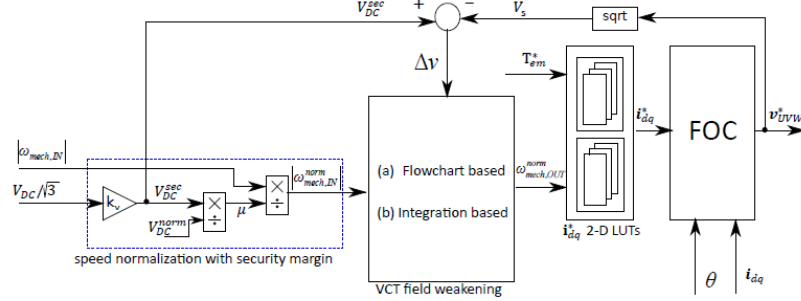


Figure 4.12: LUT based current reference determination using the speed normalization concept and proposed VCT feedback strategies[5].

Flowchart based normalized speed control At the beginning the flowchart checks whether V_s is higher or lower than the voltage limit, checks the sign of Δ_v . If $\Delta_v < 0$, variable *status* is set to 0 to indicate VCT strategy should be activated. In normal operation region (*status* = 1), no VCT strategy is activated: thus the output speed remains invariable. As for FW process the flowchart is divided into two branches, by checking again the sign of Δ_v . If the voltage is not saturated "A" branch will be selected. Otherwise, "B" branch will be activated. In "A", the normalized speed needs to be increased. On the other hand, when "B" branch is activated, the normalized speed should be reduced. If the calculated normalized speed is smaller than the reference normalized speed the flowchart assumes that VCT operation should be stopped.

Integration based normalized speed control The integration based voltage closed loop algorithm can be defined as:

$$|w_{mech,OUT}^{norm}(k)| = |w_{mech,IN}^{norm}(k)| + \delta w(k) \quad (4.14)$$

where

$$\delta w(k) = \begin{cases} 0 & \text{if } \delta w(k) \leq 0 \\ \delta w(k) & \text{if } 0 < \delta w(k) \leq \delta w_{max} \\ \delta w_{max} & \text{if } \delta w(k) > \delta w_{max} \end{cases} \quad (4.15)$$

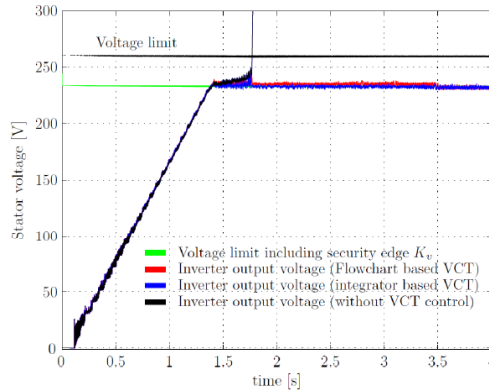
By modifying the normalized speed to be inserted in the 2D LUT and adjusting its magnitude across the $\delta w(k)$ term, this strategy alters the speed. The normalized speed corrector term usually has a negative value when the inverter output voltage is not saturated. Due to the saturation effect described in 4.15, $\delta w(k)$ is only allowed to take on positive values, therefore this corrector doesn't change the normalized speed's magnitude. The speed output therefore remains constant in cases when no voltage limit is met. In order to bring the stator voltage back within the voltage limit and prevent control instability, the normalized speed must be raised if the inverter output voltage exceeds the voltage limit. Due to the Δv polarity in this case, the speed corrector has a tendency to turn positive.

Simulation results obtained in [5] are reported. It can be seen in Figure 4.13 that when VCT control is not active in the loop, the voltage limit is exceeded and the system becomes unstable due to the electrical parameter variations. However, an effective VCT control is achieved when using both proposed strategies. A proper torque control is achieved despite the introduced parameter variation. In order to analyse and compare

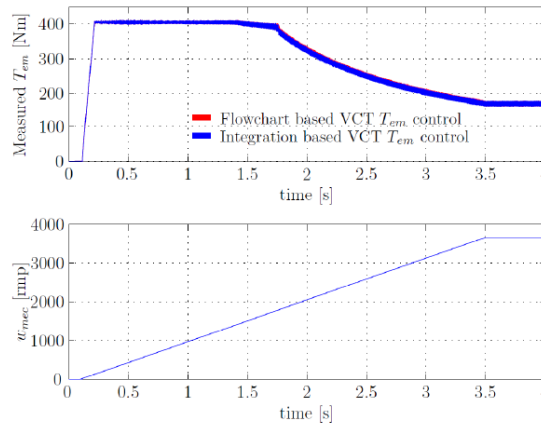
the system's performance using the proposed strategies, performance indices have been adopted in [5], being the system optimum when the index reaches a minimum value. The performance index used is the Integral of the Square of the Error (ISE), defined as:

$$ISE = \int_0^T e^2(t) dt \quad (4.16)$$

Integrator based VCT technique minimizes the ISE index. While the flowchart based method implementation requires two parameters to set, only one parameter to be adjusted is needed in the integration based one.



(a) VCT voltage control results of the proposed hybrid control strategies



(b) VCT torque control results of the proposed hybrid control strategies

Figure 4.13: Proposed hybrid IPMSM control strategies simulation results[5].

4.2.3 Feed-Forward based Field Weakening for Fast Dynamics

When traction drive systems are powered by batteries, the battery voltage fluctuation necessitates quick dynamics for the field weakening. The dynamic response of the traditional feedback-based field weakening approaches is not satisfying for these kind of applications. In [6], a novel field weakening approach is suggested in order to achieve quick torque control dynamics. It is based on feed-forward control, and the torque and flux reference are used to instantly determine the d- and q-axis current reference. Tables that are generated from the measured data can be used to derive the current references.

The required flux level may be quickly dynamically modified using the feed-forward control. The manufacturing tolerance or temperature, however, can alter the magnetic

properties. Along with the back-EMF voltage, the machine voltage also includes components for resistance drop and core loss. As a result, the closed-loop control is introduced, and the proportional integral (PI) regulator compares the output machine voltage to the reference voltage.

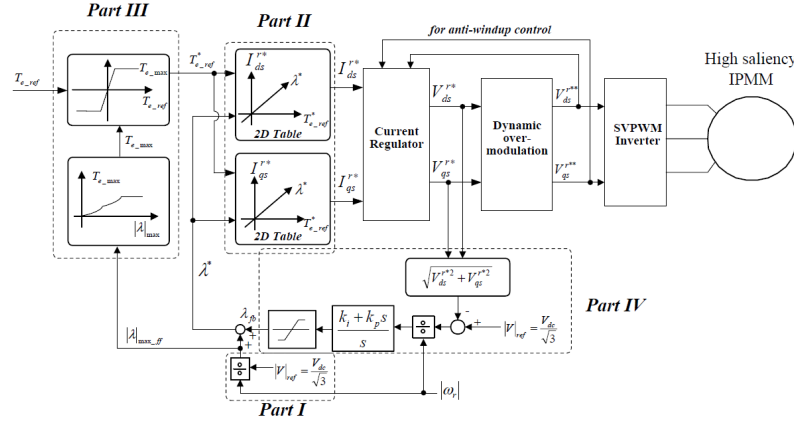


Figure 4.14: Control block diagram of proposed field weakening control[6].

The motor speed and dc link voltage are used in part I to determine the flux restriction.

The tables in Part II carry out two tasks at once. The first function is to create current references for open-loop control using flux and torque references as a starting point, and the second function is to linearize the current references in relation to the output feedback controller.

In order to ensure consistent mechanical power when speed rose above the machine's base speed, Part III restricts the highest permissible command torque. The feedback control loop is added utilizing the machine voltage in Part IV. This feedback control loop gives the machine's characteristics, such the stator resistance and inductances, resilience to uncertainty and variation. This block allows for the retrieval of flux references, and consequently torque, given the available voltage and the current machine speed.

4.2.4 Model Reference Adaptive Control

To ensure a good performance and effective functioning of the vehicle, a high degree of torque control precision is needed.

From the perspective of controller design, the best d-q axes reference currents for the Interior Permanent Magnet Synchronous Motor (IPMSM) produced by the controller depend on the motor's specifications as well as the desired torque and operating speed. In fact, there might be a significant disparity between the output torque response and the torque reference due to fluctuations in motor parameters brought on by temperature changes and magnetic saturation. For high performance drive applications, the Model Reference Adaptive Control (MRAC), a direct adaptive strategy, has been acknowledged as a viable control approach. When compared to a traditional fixed-gain PI controller technique, the MRAC approach can manage a system with parameter uncertainty and can give superior dynamic performance with reduced parameter sensitivity.

A controller, a controlled plant, a reference model, and an adjustment mechanism make up the MRAC system in general. In order for the plant response to converge and match the response of the reference model, the notion of MRAC is to adaptively update the controller's parameters depending on the difference between the output of the plant and the intended response from the reference model. Therefore, the loss function J is a function of independent adjustable positive parameters $(\theta_1, \theta_2, \dots, \theta_i)$:

$$J(\theta_1, \theta_2, \dots, \theta_i) = \frac{1}{2}(y - y_m)^2 = \frac{1}{2}e^2 \quad (4.17)$$

where y, y_m and e are the output of the plant, the output of the reference model, and the difference between these outputs.

To make the loss function small it is necessary to change the adjustable parameters in the direction of the negative gradient of J :

$$\frac{d\theta_i}{dt} = -\gamma \frac{dJ}{d\theta_i} = -\gamma e \frac{\partial e}{\partial \theta_i} \quad (4.18)$$

where γ is the adaptive rate parameter, $\partial e / \partial \theta_i$ is the sensitivity derivative of the system with respect to θ_i .

The change of the adjustable parameters is assumed to be significantly slower than the change of the plant output. Consider that the plant and reference models are of first orders:

$$\dot{y}(t) = -ay(t) + bu(t) \quad (4.19)$$

$$\dot{y}_m(t) = -a_m y_m(t) + b_m u_c(t) \quad (4.20)$$

where a_m and b_m are the parameter of the reference model, a and b are the parameters of the plant known approximately or slowly varying, u_c is the control input of the reference model, u is the control input of the plant.

Assume that the plant control input signal consists of the adjustable reference model input signal and adjustable negative plant feedback:

$$u(t) = \theta_1 u_c(t) - \theta_2 y(t) \quad (4.21)$$

Thus, the transfer function which relates y and u_c is:

$$y = \frac{b\theta_1}{s + a + b\theta_2} u_c \quad (4.22)$$

Finally the adjustable parameters are obtained as

$$\theta_1 = -\frac{\gamma}{s} \left(e \left(\frac{a_m}{s + a_m} u_c \right) \right) \quad (4.23)$$

$$\theta_2 = \frac{\gamma}{s} \left(e \left(\frac{a_m}{s + a_m} y \right) \right) \quad (4.24)$$

The constant parameter γ is chosen via iterative simulations to provide the required dynamics of the plant and convergence rate.

[7] proposes an adaptive torque control system that consists of an adaptive MRAC torque controller, the low-pass filter based torque estimator, and provides the combined Maximum Torque Per Ampere (MTPA) and Maximum Efficiency (ME) control strategy.

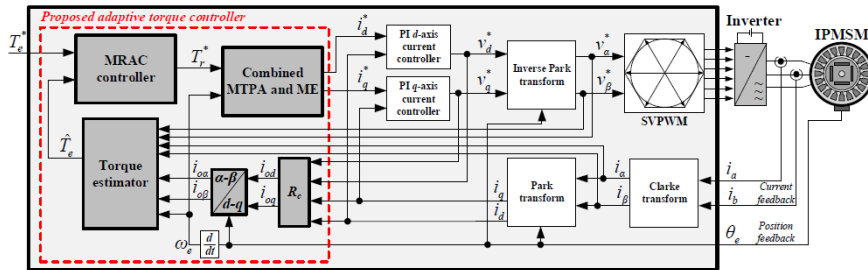


Figure 4.15: Structure of the proposed adaptive MRAC torque controller[7].

The best d-q axis reference currents are produced using the combined MTPA and ME control technique. The idea behind the combined MTPA and ME control technique is to

seamlessly coordinate the ideal IPMSM reference stator currents based on the system's operating circumstances. The combined method approaches the MTPA control to extract the maximum output torque for lower command torques. The combined approach is more similar to ME technology in terms of power consumption reduction for greater command torques. Based on the fictitious electrical power loss (P_f) can be defined as:

$$P_F = P_{Cu} + \beta P_{Fe} \quad (4.25)$$

where β is a control parameter ($0 \leq \beta \leq 1$), and is defined as a ratio between the command torque and the rated motor torque.

The performance analysis taken in [7] is shown in Figure 4.19 that presents a comparison of dynamic torque responses between the proposed adaptive torque control system and the open-loop torque control system with $T_e^* = T_r^*$ as independent control reference when several cases of motor parameter variations are considered. The torque estimator can accurately estimate the motor torque during load disturbances and parameter fluctuations, and at the same time, the MRAC torque controller can create the reference torque for the combined MTPA and ME control scheme. Since the value of motor stator resistance is generally low, it can be shown that resistance change has little impact on torque fluctuation and inaccuracy. The differences in L_d and L_q inductances have a significant influence on the dynamics performance for the open-loop system. The suggested approach considerably improves control performance in steady-state and dynamics over the full operating range, and it can achieve output torque response steady-state error of zero in every situation where motor parameter fluctuations occur.

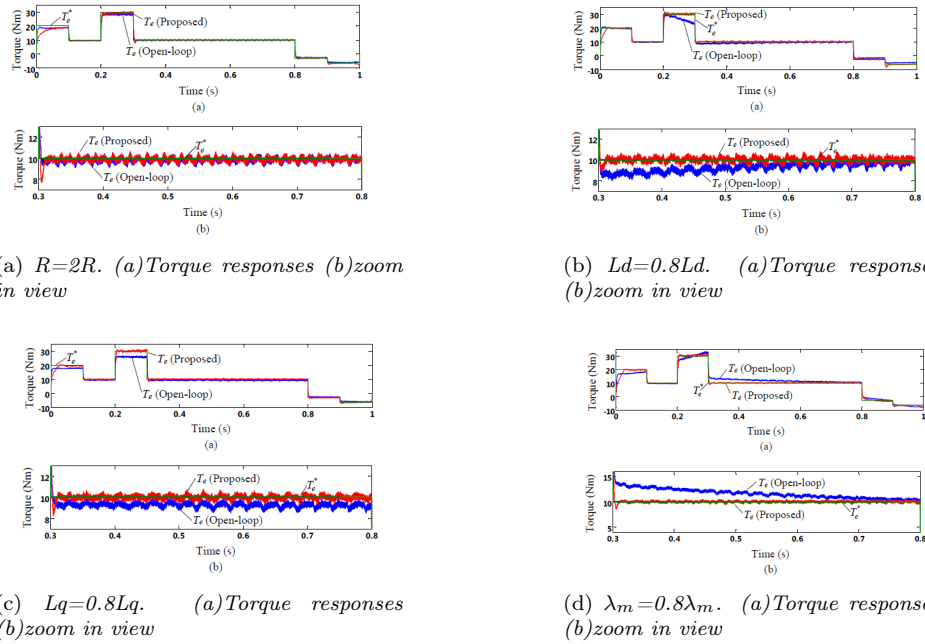


Figure 4.16: A comparison of dynamic results with parameter error[7].

4.3 DFVC

The Direct Flux Vector Control (DFVC) controls the torque by adjusting the quadrature current component, while the stator flux amplitude is directly controlled by the direct voltage component. The DFVC is especially useful when flux-weakening is necessary since it can easily ensure maximum torque generation while adhering to current and voltage restrictions. Maximum torque output is ensured for all motor types in flux-weakening,

and even in the situation of changing DC-link voltage, the inverter voltage and current restrictions are completely used with no effect from the motor characteristics.

4.3.1 Modeling of the AC Machines

The adopted reference frame are defined in Figure 4.17, for all the considered machines: stationary frame (α, β) , rotor frame (d_m, q_m) , rotor flux frame (d, q) and stator flux frame (d_s, q_s) . The axis alignment chose for the SyR motor is unconventional because the d-axis is along the minimum permeance axis and not along the maximum permeance as usual in literature. This choice permits to adopt a unified magnetic model of the three considered synchronous machines (SyR, IPM, SPM).

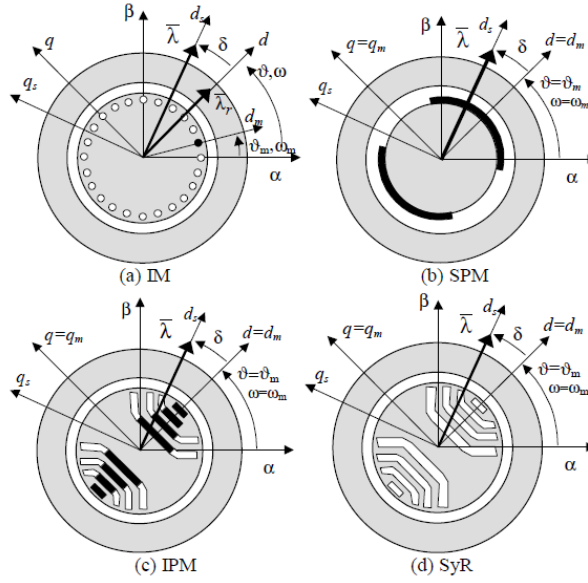


Figure 4.17: Definition of reference frames for AC machines[9].

The voltage model and torque equation are common to all the machines also in the stator flux frame as

$$\bar{v}_{dq_s} = R_s \cdot \bar{i}_{dq_s} + \frac{d}{dt} \cdot \begin{bmatrix} \lambda \\ 0 \end{bmatrix} + \lambda \cdot \begin{bmatrix} 0 \\ \omega + \frac{d\delta}{dt} \end{bmatrix} \quad (4.26)$$

$$T = \frac{3}{2} \cdot p \cdot \lambda \cdot i_{q_s} \quad (4.27)$$

where ω is the rotor synchronous speed and δ is the load angle the phase angle of the stator flux with respect to the rotor flux (IM) or with respect to the d-axis (SyR, SPM, IPM).

The stator flux amplitude λ can be regulated by means of the d_s -axis voltage, while the load angle can be controlled by means of the q_s -axis voltage for regulating the electromagnetic torque.

The q_s -axis current equation for an IPM motor is:

$$L_d \frac{di_{q_s}}{dt} = -R_s i_{q_s} + k(v_{d_s} - R_s i_{d_s}) + b(v_{q_s} - \omega \lambda) \quad (4.28)$$

Where the two factors k and b vary according to the type of motor:

$$\begin{cases} k_{IPM}(\delta) = \frac{1}{2} \left(1 - \frac{L_d}{L_q} \right) \sin(2\delta) \\ b_{IPM}(\lambda, \delta) = - \left(1 - \frac{L_d}{L_q} \right) \cos(2\delta) + \frac{\lambda_m}{\lambda} \cos(\delta) \end{cases} \quad (4.29)$$

The SyR motor model is obtained from the IPM model with the magnet flux λ_m equal to zero in the b factor, while the k factor is the same.

$$\begin{cases} k_{SyR}(\delta) = k_{IPM}(\delta) \\ b_{SyR}(\lambda, \delta) = -\left(1 - \frac{L_d}{L_q}\right) \cos(2\delta) \end{cases} \quad (4.30)$$

The SPM motor has k equal to zero and a simplified expression of b :

$$\begin{cases} k_{SPM}(\delta) = 0 \\ b_{SPM}(\lambda, \delta) = \frac{\lambda_m}{\lambda} \cos(\delta) \end{cases} \quad (4.31)$$

b factor is representative of the torque derivative with respect to the load angle δ

$$b = \frac{L_d}{\lambda^2} \frac{\partial T}{\partial \delta} \quad (4.32)$$

From the machines state-space models, it follows that:

- The stator flux can be controlled by means of the d_s voltage with high bandwidth, regardless of magnetic saturation, while the torque can be regulated with the closed-loop control of the q_s -current component through the q_s -axis voltage.
- For IPM and SyR motors, the i_{qs} equation shows a cross-coupling with the direct axis. Such control disturbance depends of the term $k(\delta)$ and has effect during flux regulation transients only. The closed-loop control of i_{qs} rejects the effects of such moderate cross-coupling.
- For the synchronous motors the i_{qs} control is stable in the operating region where $b(\lambda, \delta) > 0$, while it becomes unstable where $b < 0$ according to 4.28. $b = 0$ boundary coincides with the MTPV trajectory. MTPV operation is achieved in the proposed control by limiting the flux phase angle δ to a proper value, that is typical of each motor type. The respect of the MTPV constraint also ensures the control stability over the entire speed range. Moreover, the implemented MTPV strategy keeps the i_{qs} control stable also in case the stability boundary $b = 0$ is eventually crossed.

The torque derivative with respect to δ is:

$$\frac{\partial T}{\partial \delta} = \frac{3}{2} \frac{p}{L_d} \left(-\frac{L_q - L_d}{L_q} \lambda^2 \cos(2\delta) + \lambda_m \lambda \cos(\delta) \right) \quad (4.33)$$

The MTPV load angle condition is obtained by imposing that 4.33 is zero:

$$\frac{L_q - L_d}{L_q} \lambda^2 \cos(2\delta) = \lambda_m \lambda \cos(\delta) \quad (4.34)$$

For the SyR and SPM motors, equation 4.34 has an easy solution:

$$\delta_{max, SyR} = 135^\circ \quad (4.35)$$

$$\delta_{max, SPM} = 90^\circ \quad (4.36)$$

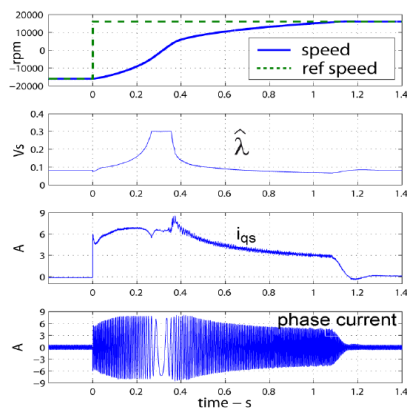
Dealing with the IPM motor, the solution of 4.34 depends of the relationship between the motor saliency, represented by the $(L_q - L_d)/L_q$ term, and the PM flux, that is different from the motor to motor since many different design types are included in the IPM category. In any case, the solution of 4.34 lead to a δ_{max} in the middle between 4.36 and 4.35

$$90^\circ < \delta_{max, IPM} < 135^\circ \quad (4.37)$$

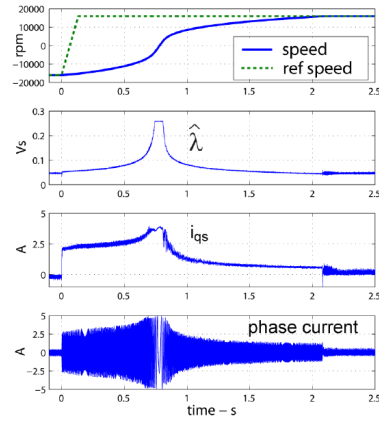
Maximum torque per voltage (MTPV) current limitation The MTPV operation may be achieved by restricting the load angle to a maximum value δ_{max} , which depends on the motor type. The i_{qs} current component and the load angle δ are closely related. The limitation of the load angle is specifically caused by the i_{qs} current limit. In order to achieve control in the MTPV operation, the i_{qs} current reference is limited in accordance with the measured load angle. This additional current limitation is carried out by the same saturation block and results in a decrease of the current amplitude below the inverter limit, as demanded by the MTPV constraint, because the previously mentioned I_{max} saturation keeps the current inside the inverter limit. A proportional-integral regulator (PI) is used in the unified i_{qs} limitation approach to limit the i_{qs} reference in accordance with the observed load angle and further lower the i_{qs}^* maximum value if the δ_{max} set point is surpassed. With any δ_{max} set-point, properly chosen or not, it can be shown that the PI-based δ_{max} control solves the instability issues of (λ, i_{qs}) control.

Experimental Results

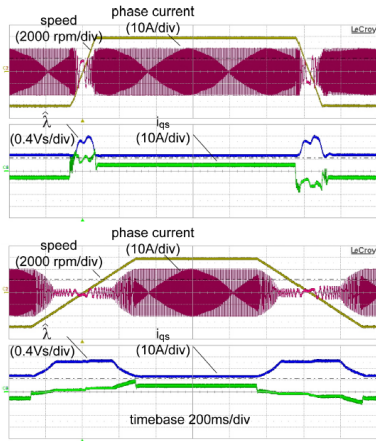
Speed reversal reported in [9] are shown in Figure 4.19 for the all the machines tested (IM, IPM, SPM and SyR). The reported signals are the measured speed, the controlled variables λ and i_{qs} and one phase current. The inverter current limit is set to 8 A peak, and the IM speed reversal is shown between negative and positive 16000 rpm. The maximum current constraint sets a limit of 8 A on the phase current in the low speed band. The MTPV control block limits the qs component to lower the phase current outside of this time window. The motor losses (copper and iron) contribute to deceleration, and the greater dc-link voltage (caused by motor braking, which charges the DC link capacitor) enables getting a higher flux reference, thus the deceleration is quicker than the acceleration. Similar features may be seen in the IPM motor's speed reversal, which has a maximum current limit set at 5 A peak. Due to the MTPV constraint, the phase current amplitude is often less than 5 A, and maximum current operation is only seen at low speeds. The SPM motor's ability to reverse speed is demonstrated between 600 rpm in the negative and positive directions using two distinct ramps, with a 20 A peak inverter current limit. The quick ramp demonstrates that the i_{qs} current required for fast acceleration is substantially lower than the current required for de-magnetization at 6000 rpm, no load. The SyR motor's speed reversal is shown between -6000 and +6000 rpm, with a maximum peak inverter current of 5 A. The motor torque is heavily limited by the MTPV above 4000 rpm and results in a very limited speed range in flux weakening. However, such limitation is typical of the SyR motor type, while the control fully exploits the torque capability of the drive.



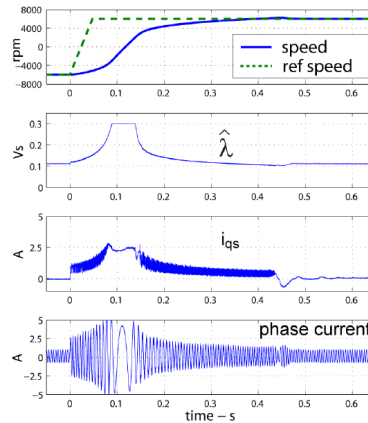
(a) IM speed reversal
(-16000rpm ÷ 16000rpm)



(b) IPM speed reversal
(-16000rpm ÷ 16000rpm)



(c) SPM speed reversal
(-6000rpm ÷ 6000rpm) with two different
ramp slopes: 12000rpm/s (top) and
20000rpm/s (bottom)



(d) SyR speed reversal
(-6000rpm ÷ 6000rpm)

Figure 4.19: Speed Reversal results[9].

4.4 Fault Tolerance

A system's ability to maintain normal operation in the event that one or more of its components fail is known as fault tolerance. In contrast to a system that is naively constructed, where even a tiny failure might result in catastrophic collapse, if its operational quality reduces at all, the reduction is proportionate to the degree of the failure. The type of common faults arising in a motor are: the open-phase fault, intern-turn fault, speed sensor fault and the limp-home fault.

4.4.1 Sensorless Torque-Control

The need for safety rises along with the adoption of EVs. Speed sensor failure is one of the problems EVs are having. This may cause the electric motor driving system of the EV to become paralyzed and enter standstill mode. Therefore, having a driving system that is fault resistant to speed sensor failure is crucial. According to the notion of a fault-tolerant drive, the drive can continue to function properly even when a failure or fault occurs. For the rotor flux angle computation in FOC, sensorless speed estimate is necessary in the absence of a mechanical sensor. Due to the simplicity and minimal

processing cost of the resultant approach, Model Reference Adaptive Techniques (MRAS) are used. The solution proposed in [10] regards a robust back-EMF MRAS scheme for the purpose of fault tolerant operation for EV applications.

Conventional Back-EMF MRAS Scheme

The conventional Back-EMF MRAS consists of a reference model, an adjustable model and an adaptation mechanism. The reference model takes in the stator voltage and current components, in the stationary reference frame, and in return provides two reference back-EMF components.

$$\bar{e}_m = \bar{v}_s - R_s \bar{i}_s - L_s \sigma p \bar{i}_s \quad (4.40)$$

Where \bar{v}_s and \bar{i}_s are stator voltage and current vectors in the stationary reference frame, respectively. R_s and L_s are stator resistance and inductance, respectively, $p = \frac{d}{dt}$ is the differential operator, and $\sigma = 1 - (\frac{L_m^2}{L_s L_r})$ is the leakage coefficient. The adjustable model expressed in the stationary reference frame, is derived from the rotor voltage equation of IM, can be written as:

$$\bar{e}_m = \frac{L_m}{L_r} p \bar{\psi}_r = \frac{L_m}{L_r} \frac{(L_m \bar{i}_s - \bar{\psi}_r + j \omega_r T_r \bar{\psi}_r)}{T_r} \quad (4.41)$$

Where $T_r = \frac{L_r}{R_r}$ is the rotor time constant.

The rotor angular velocity estimate is obtained from a PI controller (adaptation mechanism) as:

$$\hat{\omega}_r = \left(k_p + \frac{K_i}{p} \right) (\hat{e}_m \times \bar{e}_m) \quad (4.42)$$

Robust Back-EMF MRAS Scheme

The solution proposed in [10] takes advantage of combining two back-EMF reference values which are based on the current and the voltage models of the IM. This compensates for the stator resistance and stator inductance variations and hence results in reliable speed estimation.

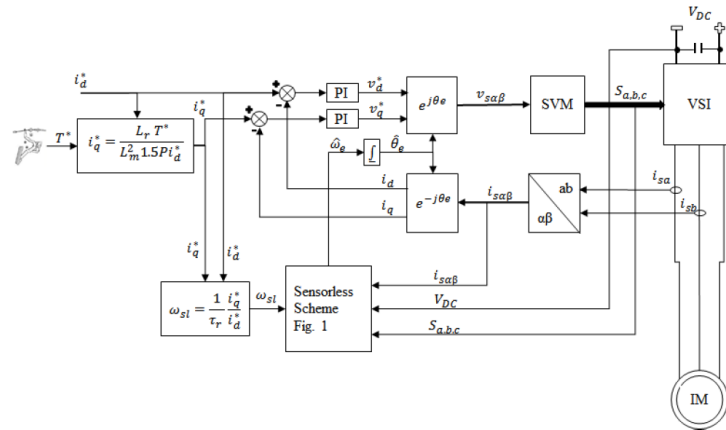


Figure 4.20: Block diagram of sensorless torque control scheme based on FOC technique used in EV applications[10].

The stator resistance fluctuation is known to affect speed estimators based on back-EMF MRAS, especially at zero and low speeds. This is a result of the reference model's reference model's significantly huge voltage loss over the stator resistance. It is anticipated that this approach will be insensitive to the stator resistance fluctuation since the reference model includes compensating terms for the stator resistance variation. Figure 4.21, taken

from the experimental results of [10], clearly illustrates that the conventional scheme is highly sensitive to variations in the stator resistance. However, the scheme was consistent at starting from standstill regardless of the stator resistance variation.

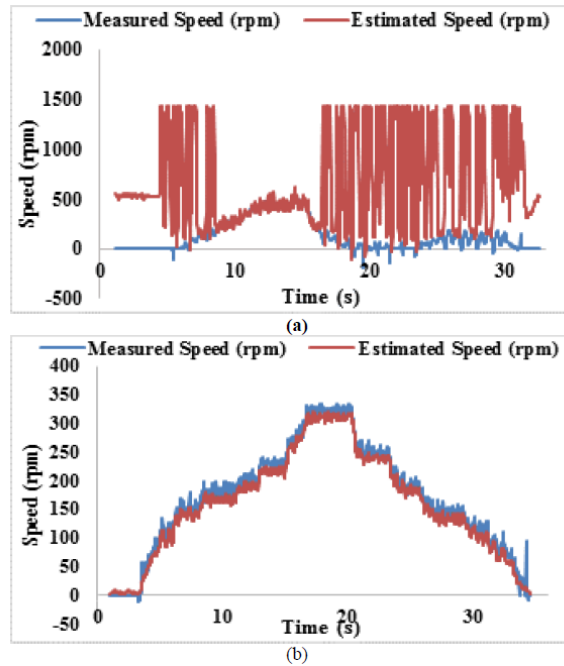


Figure 4.21: Experimental results for sensorless performance with 50% increase in the stator resistance and applied torque command of 10 Nm. (a) Conventional Back-EMF MRAS (b) Robust Back-EMF MRAS[10].

4.4.2 Open-Phase Fault-Tolerant Control

Since their sole wearable component is a bearing, PMSMs are extremely dependable. However, problems with the motor, associated power electronics, and sensors are not completely ruled out.

The open-phase fault is a frequent problem that can occur both directly in the motor and in the connected voltage-source inverter (VSI). An open circuit in one of the machine stator windings or in one or both of the switches in one leg of the VSI might be the root of the problem. The impacted phase will thus become disconnected and cannot be used to generate torque.

In the event of an open-phase failure, a typical three-leg VSI in conjunction with a traditional three-phase PMSM results in a significant torque variation. Only one current may be managed separately during the post-fault process. A straightforward way to enable several independent current flows even during problematic operation is to connect the motor's neutral point to the center of the VSI DC-link, where the voltage usage is equal. There is a power reduction even when the number and length of available voltage vectors decrease.

Model predictive control (MPC) makes use of a model of the plant to forecast system behavior for each potential control trajectory over a given time horizon. The plant will be subjected to the optimal control trajectory, which is the one delivering the lowest value of the cost function.

Finite-control-set (FCS) MPC builds a control set using just eight voltage vectors, which are provided by the eight potential switching states of the inverter, in order to account for the discontinuous character of the VSI.

In [11], a direct torque control method built on FCS-MPC that can tolerate open-phase faults is proposed. The suggested algorithm's benefit is its limitless functioning

in both the healthy condition and post-fault operation without an increase in torque variation. The torque waveform also shows a seamless transition from the healthy condition to the postfault operation.

The suggested FCS-MPC method is based on the discrete nature of power converters, where only a limited set of possible switching states may be satisfied, depending on the potential ON/OFF configurations of the power switches. The motor model may also be used to forecast how the variables will behave in each switching state. The algorithm determines whether a fault exists before predicting the currents and back EMF to determine the future torque. This is done in order to choose the best switching state to be used. For each potential switching state, the predicted value of the torque is determined. The switching state that reduces the cost function will then be chosen.

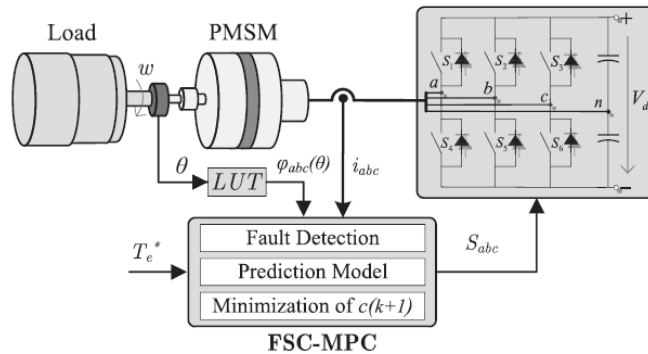


Figure 4.22: Simplified description of the system[11].

Fault Detection

The fault detection algorithm consist of comparing the current predicted in the previous sampling with the actual measured current value. So, if in the new sampling, a phase is open, there will be a noticeable difference with the current predicted in the previous sampling. The result obtained is compared with a threshold value u , which determines the phase with failure.

$$r(k) = i^p(k) - i^m(k) \quad (4.43)$$

with $r = [r_a r_b r_c]^T$, where k is the actual sample, and indices p and m stand for predicted and measured values, respectively. The output of the fault detection algorithm delivers a matrix F for the variable abc , which is 1 when the system is healthy and 0 when the system is in failure, F is a diagonal matrix 3×3 with the elements F_a, F_b and F_c in the diagonal. In this sense, when a failure occurs, the fault detection algorithm is responsible for canceling the predicted current in the failed phase. The proposed method has the advantage that it uses only the valid control variables and is also not affected by transients appearing due to the reference torque changes, since they are predicted and canceled in 4.43. On the other hand, the negative influence of the unavoidable model uncertainties on the fault detection is small and can be handled by setting the threshold to a higher value.

In order to carry out the proposed control, the torque is required to be predicted for the next step $k + 1$. thus, phase currents in a discrete time can be expressed as:

$$i(k + 1) = i(k) + T_s L^{-1} [v(k) - Ri(k) - e(k)] \quad (4.44)$$

where T_s is the sampling interval and L^{-1} is the inverse of the inductance matrix. By applying available control set the prediction of the future phase currents will be given by:

$$i^p(k + 1) = Fi^m(k) + FT_s L^{-1} [v_d(k) - Ri^m(k) - e(k)] \quad (4.45)$$

After the phase current prediction is done, the expected torque in the next sample step can be estimated as

$$T_e^p(k+1) = \phi^p(k+1)\dot{i}^p(k+1) \quad (4.46)$$

Cost Function Optimization

The main goal of the proposed algorithm is to track the torque reference with the least possible error, for which a cost function is required that selects vectors with the best control performance and minimum losses. Hence, the cost function for this proposal will be composed by the following three components.

- **Reference Torque Tracking:** The main goal of the developed FCS-MPC is the minimization of the torque error. Thus, the first cost function component represents the error between the reference torque and the expected torque as follows:

$$c_T(k+1) = (T_e^*(k+1) - T_e(k+1))^2 \quad (4.47)$$

where $T_e^*(k+1)$ is the reference torque for the next sample step.

- **Torque Sharing:** In four wire topologies, if the considered machine possesses a zero-sequence component in the back EMF, the available neutral line allows us to distribute the generated torque between the three-phase system in an optimal way to reduce copper losses.
- **Reactive Power Minimization:** In order to achieve additional loss reduction, the instantaneous reactive power of the PMSM should be kept to zero, since it does not contribute to torque generation. Thus the cost function will be extended by reactive power component c_q

$$c_q(k+1) = (\varphi_\alpha(k+1)i_\beta(k+1) - \varphi_\beta(k+1)i_\alpha(k+1))^2 \quad (4.48)$$

- **Cost Function:** Finally the cost function is defined as

$$c(k+1) = \lambda_T c_T(k+1) + \lambda_0 c_0(k+1) + \lambda_q c_q(k+1) \quad (4.49)$$

where λ_T, λ_0 and λ_q are weight coefficients, which define the importance of the objectives of the cost function.

The afflicted phase's back EMF will be deemed to be zero when a defect occurs since it has no effect on the torque generation. As a result, the $\alpha\beta$ frame's zero-sequence component of the considered back EMF increases dramatically. To spread the torque generation between the healthy phases and the neutral line as efficiently as possible, the high value of the common EMF will be employed. This results in an enhanced and pulsing zero-sequence torque and a discernible zero-sequence current. The overall torque that results, nevertheless, remains smooth. Furthermore, the results obtained in [11](Figure 4.23) show no torque oscillation at the transition from the healthy state to the postfault operation.

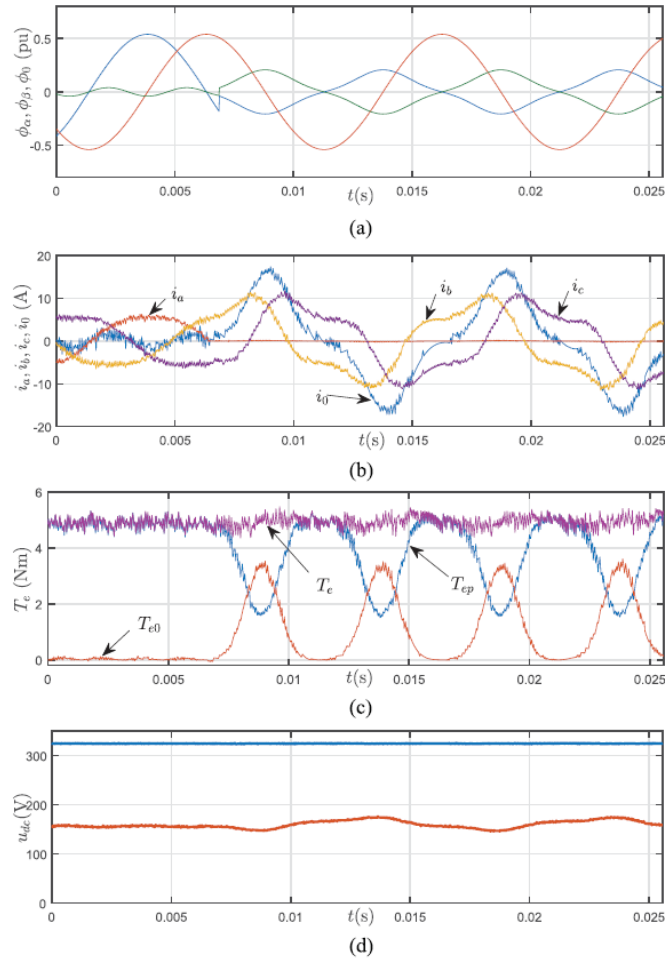


Figure 4.23: System with failure with fault detection and tolerance. (a) Waveform of the EMF (b) Measured currents (c) Electromagnetic torque (d) DC-link voltage (blue) and bottom capacitor voltage (orange)[11].

4.4.3 Intern-Turn Fault Tolerant Control

In [12] a technique that combines the Model Predictive Control (MPC) for the speed and current control loops, and an almost error-free Unscented Kalman Filter (UKF) to estimate the PMSM intern-turn fault ratio, is proposed.

Fault Diagnosis Algorithm

The first step in the UKF procedures is to extend the states with the unknown parameters such as:

$$\tilde{x}_k = \begin{bmatrix} x_c(t) \\ \gamma(t) \end{bmatrix} = [i_{sd} \quad i_{sq} \quad \omega_e \quad n_{As/c} \quad n_{Bs/c} \quad n_{Cs/c}]^T \quad (4.50)$$

where \tilde{x}_k represents the total estimated states, $\gamma(t)$ is the additional estimated parameters to the original states, $n_{As/c}$, $n_{Bs/c}$ and $n_{Cs/c}$ that are the short circuit turns ratio of the fault at the definite phase.

$$\begin{cases} \tilde{x}_{k+1} = F_k \tilde{x}_k + B_k u_k + w_k \\ \tilde{y}_k = H_k \tilde{x}_k + D_k u_k + v_k \end{cases} \quad (4.51)$$

where

$$\begin{aligned}
 F_k &= \begin{bmatrix} 1 + T_s A_c & 0 \\ 0 & I_{3 \times 3} \end{bmatrix} \\
 B_k &= \begin{bmatrix} T_s B_c \\ 0_{3 \times 3} \end{bmatrix} \\
 H_k &= C_c \\
 D_k &= D_c
 \end{aligned} \tag{4.52}$$

In order to reduce the error between the present states and the posterior ones, the UKF computes the sigma points of the posterior estimated states.

A strategy known as "softening restrictions" has been used to address the system constraints. The cost function will be:

$$j = \sum_{k=1}^{n_y} e^T(k)Q(k)e(k) + \sum_{k=0}^{n_u-1} u^T(k)R(k)u(k) + \sum_{k=0}^{n_u-1} (u(k) - \bar{u}(k))^T S(k)(u(k) - \bar{u}(k)) \tag{4.53}$$

where $\bar{u}(k)$ is the controlled input constraint with the value of $[V_{dc}/2 \quad -V_{dc}/2]^T$, and $S(k)$ is the weighting matrix.

The suggested approach is to alter the load torque, which subsequently reduces the phase current to a level equal to the increased value of the short circuit current without reducing the running speed, in order to make the machine work in the presence of the stator intern-turn defect. The electrical stress on the insulation of the windings will be reduced by the current deterioration, which also minimizes a potential rise in machine temperature. After the fault alert has been sounded, the planned corrective action will provide the operator adequate time to set up a redundant system or to move through with any alternative backup plan. As a result, the anticipated short circuit turns ratio in each of the three phases will determine how much torque degradation occurs. The relation between the load torque and the $n_{s/c}$ can be expressed as:

$$T_l^* = T_l - W n_{s/cA} - W n_{s/cB} - W n_{s/cC} \tag{4.54}$$

$$W = \frac{T_l}{n_{s/c}^*} - \frac{3pp\lambda(I'_{Lpeak} - I_{Lpeak})}{2n_{s/c}^*} \tag{4.55}$$

where T_l^* is the calculated reference load torque to the MPC controller after existence of the fault, $n_{s/c}^*$ is the maximum applicable value of short circuit turns ratio that machine could withstand, I_{Lpeak} is the peak value of the instantaneous load current at the torque T_l in the healthy state and I'_{Lpeak} is the peak value of the total instantaneous current consumed by the machine in case of short circuit turns ratio equal to $n_{s/c}^*$

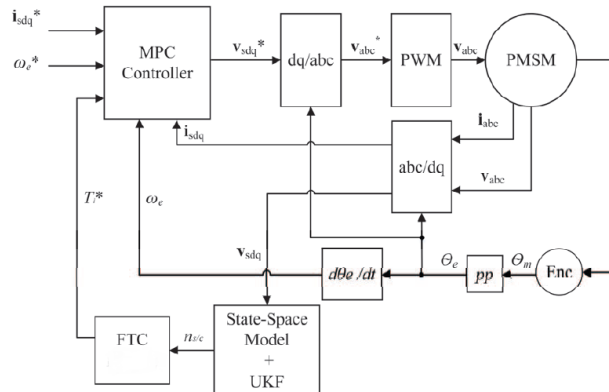
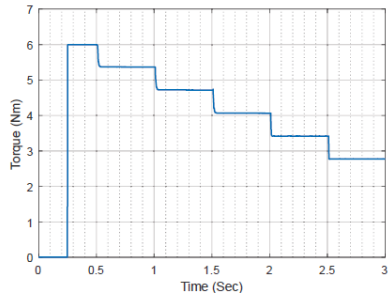
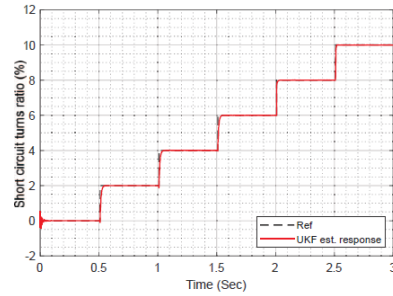


Figure 4.24: Proposed strategy for PMSM[12].

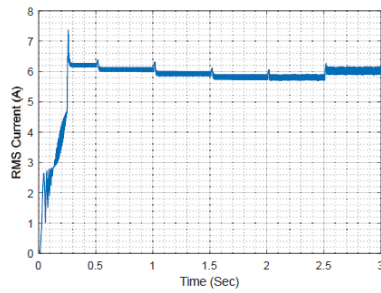
Before the protection system initiates an isolating step, it's critical to find the fault's presence. As the projected short circuit turns ratio rises, the torque begins to fall. However, despite a rise in the defect, the machine's overall current consumption stays mostly unchanged. In addition, the speed is kept constant in all fault circumstances. When a higher fault severity is encountered, a minor hiccup is seen in the speed. Keeping the motor operating at a lower torque in the presence of the defect is acceptable practice even though the motor torque is deteriorated. Results obtained in [12] are shown in Figure 4.25.



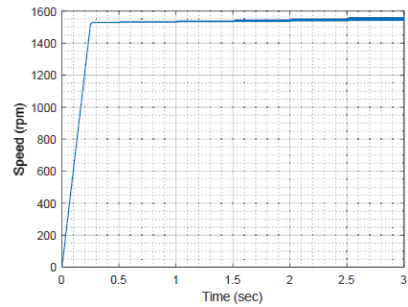
(a) Load torque behaviour at the gradually increase n_s/cA



(b) The UKF estimation response at the gradual increase of n_s/cA



(c) The total machine RMS current after the FTC action



(d) Speed response at the fault case scenario

Figure 4.25: Fault tolerant control results[12].

4.5 Control techniques evaluation

The analysis of the actual State of Art in torque control strategies for e-Motors is a necessary step to understand which one of these techniques represents the better choice to apply in our project. Following the experience of the PEIC department the first option is identified in the DFVC described in section 4.3 and in the article [9].

The DFVC presents different advantages:

- The flux weakening operation is performed straightforward without using any outer voltage regulator since the flux amplitude is controlled directly.
- Decoupled control of stator flux amplitudes (d_s -axis) and torque producing current (q_s -axis).
- The d_s -axis flux controller is insensitive to machine electric parameters variation.
- Guarantees maximum torque production under inverter current and voltage constraints, even in the deep flux weakening region with MTPV.
- The algorithm is suitable for both SM and IM motors.

And as main disadvantages:

- Torque producing current controller on q_s -axis is affected by electric parameters sensitivity.
- The d_s -axis position need to be estimated using an observer, while in FOC-based torque controller the d -axis position can be directly measured using a mechanical position transducer.

This solution is taken as benchmark, the scope of this thesis is to find and develop a valid alternative. Taking into account a compromise between performances, simplicity and what is most used by the automotive companies, FOC is identified as a good option. In particular 4D FOC is chosen.

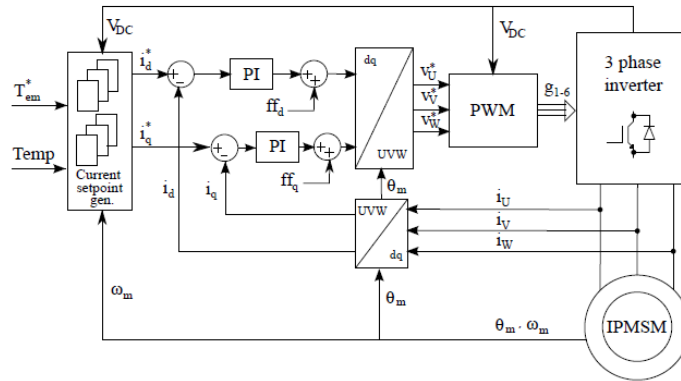


Figure 4.26: 4D FOC block scheme[5].

As can be seen from Figure 4.26 the peculiarity of this technique consist in the implementation of four dimensional LUTs that take as input not only the reference torque (T_{em}^*) and the mechanical speed (ω_m) but also the DC-link voltage (V_{dc}) and the magnets temperature ($Temp$). The solution proposed presents the following characteristics:

- Overcomes the issues due to machine electric parameters variation with temperature.
- Enables the control of the machine in the deep flux weakening region without instabilities.
- Requires several 4D-LUTs to ensure the stable operation in all the possible working points.

The drawback of this solution resides in the difficulty to elaborate precise 4D-LUTs in particular related to the uncertainty of the measure of the temperature. The temperature of the magnets and the temperature of the stator are different but they are considered the same to do not make the computation of the LUTs even more complicated adding one more dimension.

4.6 4D FOC

After the obtainment of the flux maps presented in subsection 3.1.4 the first step for the application of the 4D FOC is the elaboration of the LUTs.

4.6.1 Input signal management

To perform the 4D Field Oriented Control specific variables have to be measured:

- phase currents $\bar{i}_{abc} = [i_a, i_b, i_c]$;
- DC-link voltage;
- rotor mechanical position.

The above feedback are measured every ISR call on the digital controller. Concerning the offsets of phase currents and mechanical position, they are compensated using the conventional commissioning procedure of electric drives.

From the feedback of mechanical angle, the following action are performed:

- The electric angle of the machine θ is evaluated as pole pairs time the mechanical angle. This operation is useful only for synchronous motor in which the measured angle represents the d -axis.
- The machine speed is evaluated using a PLL whose structure is shown in Figure 4.27. It receives as inputs the mechanical angle θ_m and provides as output the instantaneous mechanical speed ω_m and its filtered value $\omega_{m, filt}$.

Usually, rather than feeding directly the PLL with the difference between measured and filtered angle, the sine approximation of this difference used. In this way, any discontinuity resulting from angle normalization is avoided. The gains of the adopted PI regulator, are designed according to the desired bandwidth ω_b and phase margin ϕ_m as follows:

$$\begin{cases} k_{p, PLL} = \frac{\omega_b \tan(\phi_m)}{\sqrt{1+\tan^2(\phi_m)}} \\ k_{i, PLL} = \frac{\omega_b^2}{\sqrt{1+\tan^2(\phi_m)}} \end{cases} \quad (4.56)$$

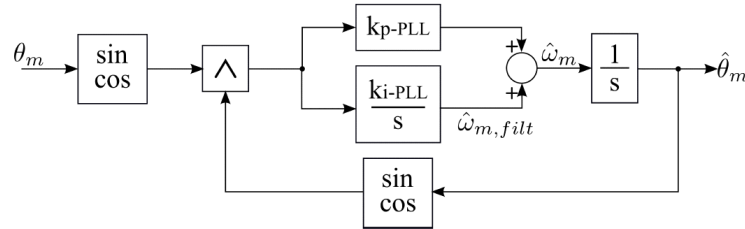


Figure 4.27: PLL scheme.

The measured DC-link voltage is filtered with a low pass filter having a high cut-off frequency in order to remove the high-frequency noise. The DC-link voltage value is one of the main input to reconstruct the stator phase voltages in phase coordinates $\bar{v}_{abc, ideal} = [v_{a, ideal}, v_{b, ideal}, v_{c, ideal}]$ from the duty-cycles $d_{abc} = [d_a, d_b, d_c]$ of the converter.

$$\begin{cases} v_{a, ideal} = \frac{V_{dc}}{3}(2d_a - d_b - d_c) \\ v_{b, ideal} = \frac{V_{dc}}{3}(2d_b - d_c - d_a) \\ v_{c, ideal} = \frac{V_{dc}}{3}(2d_c - d_a - d_b) \end{cases} \quad (4.57)$$

A subsequent compensation of inverter voltage errors is performed to obtain the actual machine phase voltage $\bar{v}_{abc, real} = [v_{a, real}, v_{b, real}, v_{c, real}]$. The phase voltage error introduced by the converter is computed using the 1D-LUT that reports the pu value of the voltage error according to the current of the considered stator phase. For each combination of DC-link voltage and switching frequency f_{sw} , a LUT should be created following the procedure proposed in [17]. The value of the voltage error of a generic phase x is evaluated as:

$$v_{x,DT} = \text{sign}(i_x)v_{x,DT_{pu}}(|i_x|)v_{dc} \quad (4.58)$$

The final value of the motor phase voltage is thus computed as:

$$\begin{cases} v_{a,real} = v_{a,ideal} - v_{a,DT} \\ v_{b,real} = v_{b,ideal} - v_{b,DT} \\ v_{c,real} = v_{c,ideal} - v_{c,DT} \end{cases} \quad (4.59)$$

Finally, the stator phase voltages and currents in stationary coordinates ($\alpha\beta$) are computed by applying the invariant amplitude Clarke transformation as:

$$\begin{bmatrix} v_\alpha \\ v_\beta \end{bmatrix} = \frac{2}{3} \begin{bmatrix} 1 & -1/2 & -1/2 \\ 0 & \sqrt{3}/2 & -\sqrt{3}/2 \end{bmatrix} \begin{bmatrix} v_a \\ v_b \\ v_c \end{bmatrix} \quad (4.60)$$

$$\begin{bmatrix} i_\alpha \\ i_\beta \end{bmatrix} = \frac{2}{3} \begin{bmatrix} 1 & -1/2 & -1/2 \\ 0 & \sqrt{3}/2 & -\sqrt{3}/2 \end{bmatrix} \begin{bmatrix} i_a \\ i_b \\ i_c \end{bmatrix} \quad (4.61)$$

4.6.2 Current set point generation

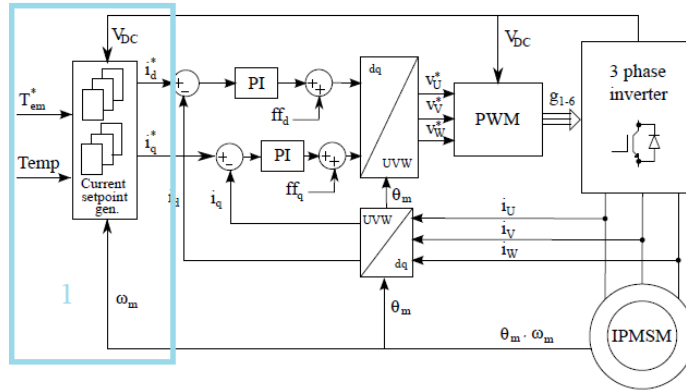


Figure 4.28: 4D FOC block scheme part 1[5].

The LUTs are elaborated using the plug-and-play method described in article [4] and previously summarized in subsection 4.2.1, dividing the computation method into the four stages:

- MTPA
- MTPV
- Maximum Current Limit
- Two-Dimensional Reference Look-up Table

4.6.3 Control Maps

The MTPA and the MTPV, together with the Direct Flux Map, are the base data needed to generate the machine Control Maps. This maps are used to define the references of the control algorithm. The control solutions selected, the LUT-based FOC, require 4D maps that represents the behaviour of the machine in all the working point of interest for the application.

The Control Maps are 2D Currents Control Maps that stores the i_d, i_q currents data as a function of torque and mechanical speed. For each combination of DC link and magnet temperature different (id,iq) maps must be generated. The ranges chosen are:

- $DC - link = 250V - 500V$ with 50V step
- $Temp = -50^\circ C - 200^\circ C$ with 50°C step

With a total of $6 \times 6 = 36$ 2D maps. Interpolating these maps together for the exact value of the DC-link and temperature we obtain two 4D maps, one for the i_d component and one for the i_q component.

The effect of the temperature on the magnet flux is taken into account with the manual application in the Matlab code of a coefficient δ_{F_d} on the d -axis of the flux corresponding to 0.12% of the magnets flux for each degree in excess with respect to the room temperature $T_s = 25^\circ C$.

```
err_Fd = (-0.12/100) * (Ts - 25);
Fm = interp2(Id, Iq, Fd, 0, 0);
delta_Fd = err_Fd * Fm;
Fd = Fd + delta_Fd;
```

The first operation that must be performed is the generation of the iso-torque profiles with respect to the dq current values. The mesh-grid of currents, the Torque Map and the number of desired torque levels are provided as input to the

`contourc`

Matlab function and the set of (i_d, i_q) points corresponding to different torque levels, are obtained. By calling with $(i_{d,cm}, i_{q,cm})$ the mesh-grid of the dq currents, the following actions are performed:

- Computation of the current amplitude;
- (dq) flux components from the Direct Map;
- Computation of the flux amplitude map;

It is highlighted how all the aforementioned maps are computed without applying any limitation, thus making necessary their elaboration to be properly implemented in the control algorithm.

Application of constraints

In the following, it is reported the step-by-step procedure required to compute the currents LUTs implemented in the motor control algorithm following what previously discussed in subsection 4.2.2 and developed in [5].

- **Working quadrant**

The choice of working quadrant comes from adopted convention. For synchronous motors having PM in the rotor, the "PM-style" convention has been applied.

The first boundary to be applied consist of removing the not-operative quadrants from the direct maps. For example, if considering the IPM motor, all the points with positive d -axis current are ruled out. In addition, only the motoring operating region has been considered due to the symmetric behaviour of the flux maps along the q -axis.

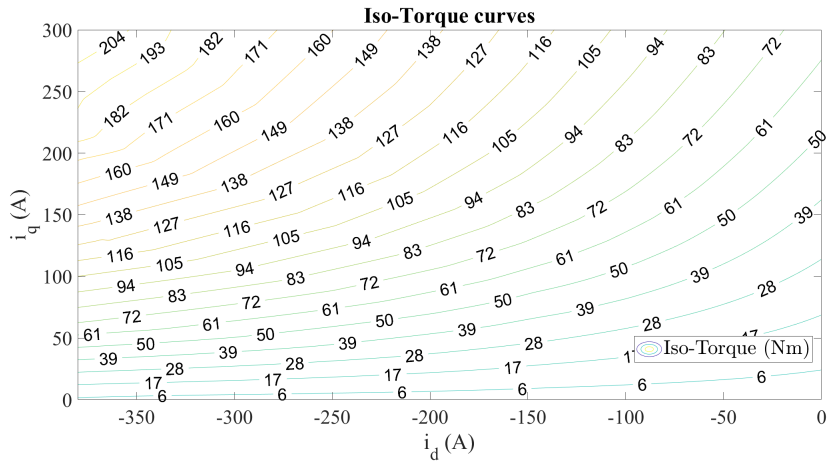


Figure 4.29: Current map computation: selection of the working quadrant.

• **Current Limit**

The second limit to apply consist of the Current Limit (CL). This limit can represents either the current limit of the power converter or the overload limit of the machine. Given the current amplitude map all the dq points that leads to overcome the current limit I_{max} are ruled out.

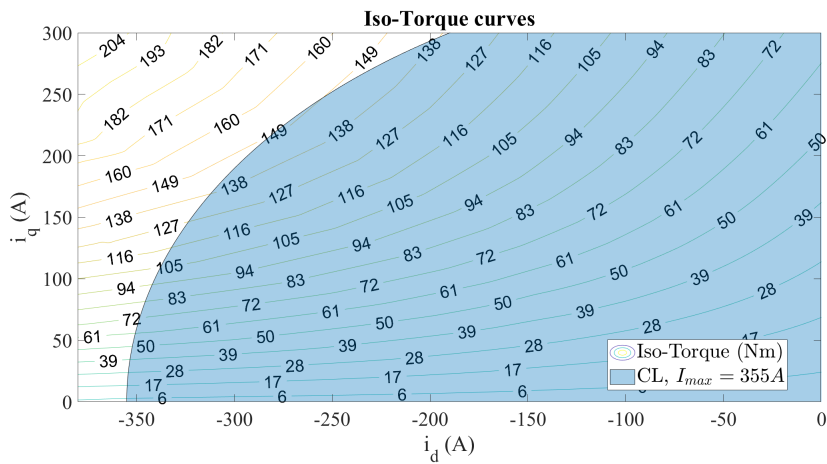


Figure 4.30: Current map computation: application of the current limit.

• **MTPA Limit**

The MTPA locus is used to limit the current amplitude to a well defined value for each torque value. To apply the MTPA limit, the current amplitude maps is needed. Only the points with current amplitude lower than one along $I_{s,MTPA}$ are considerate, while the others must be ruled out from the maps.

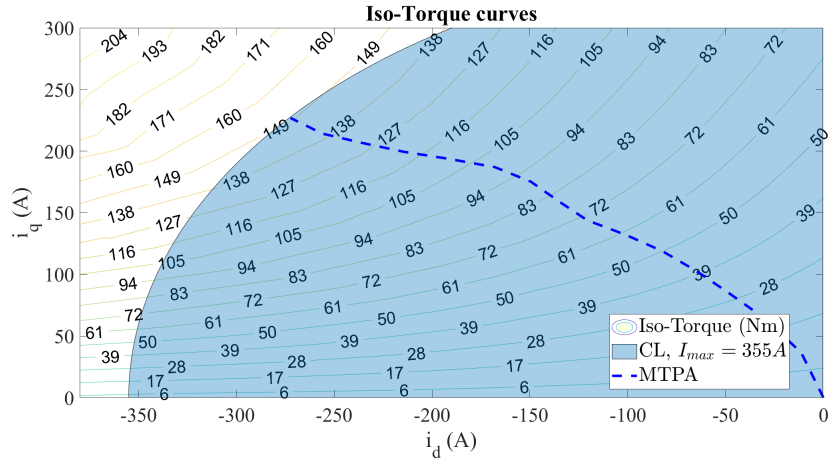


Figure 4.31: Current map computation: application of the MTPA limit.

• **MTPV Limit**

All the point beyond the MTPV locus must be ruled out to avoid the machine pull-out. In other words, all the points with the d -axis current lower than the MTPV profile are ruled from the maps.

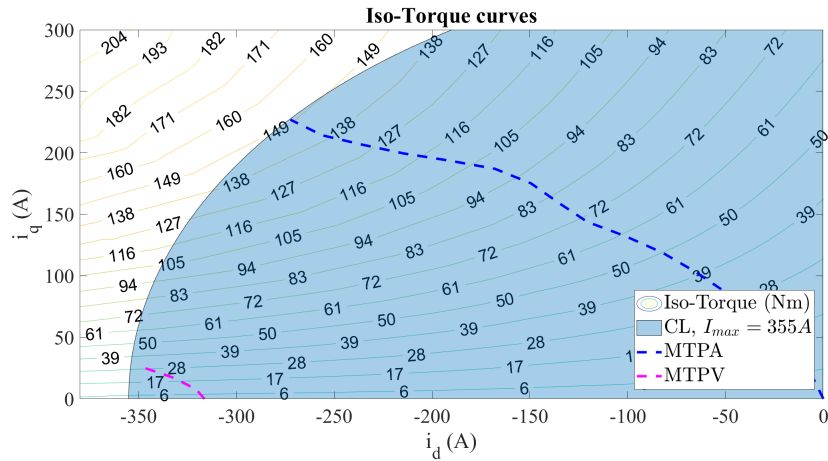
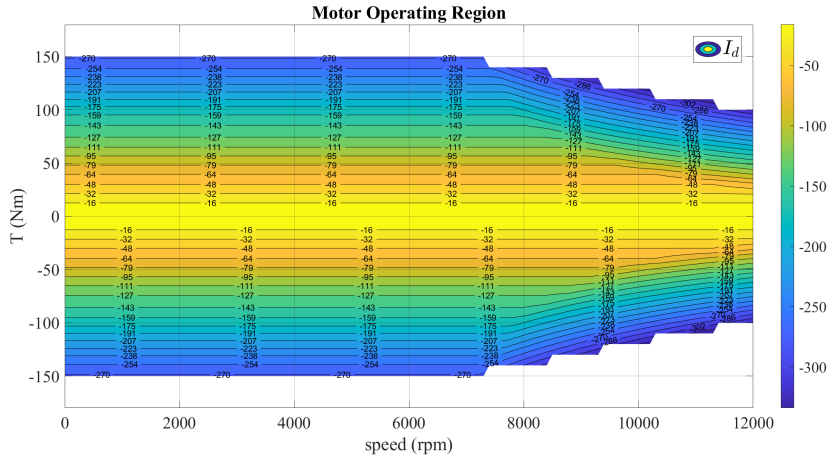


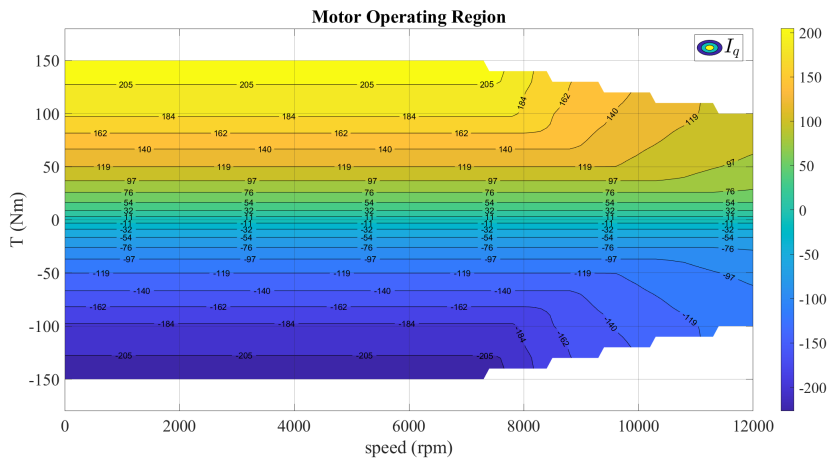
Figure 4.32: Current map computation: application of the MTPV limit.

Finally, after the application of all the constraints, the un-normalized control maps are obtained and they are shown in Figure 4.33. The scale of color represents the value of current in d and q -axes to obtain the desired torque at the speed requested. I_d is independent from the sign of the torque, that influence only I_q , and depends only on the torque amplitude. The torque profile follows the limit applied. The maximum torque is available before the base speed that represents the MTPA region with the CL applied, constant torque is guaranteed. After the base speed, it is no more possible to guarantee a constant torque. The maximum torque available become dependent from the speed. T_{max} is derived following the CL curve and then the MTPV one to ensure the stability.

At this stage, it is advisable to evaluate and store the maximum torque T_{max} that can be produced for each speed with the speed range has been discretized. This operation is necessary because the maximum torque value is needed to reconstruct the maps in the control code after their normalization.



(a) I_d map



(b) I_q map

Figure 4.33: Currents Non-normalized current Maps of IPM.

Map Normalization

Since the interpolation input of the dq -currents maps of Figure 4.33 consist of torque and mechanical speed, it is necessary to express the dq -currents maps as a function of these two variables. However the dq -currents maps obtained after applying the constraints of CL, MTPA, and MTPV are not defined on a regular torque-speed domain, hindering its implementation on the motor control algorithm.

- **Speed Normalization**

For each torque level all the torque-speed curves are sorted with increasing monotonic speed amplitudes, thus getting minimum and maximum values rpm_{min} and rpm_{max} , for each torque level.

Therefore, considering all the dq current values of each torque values, they are expressed as a function of the pu flux amplitude as follow:

- All the current amplitudes that belong to the considered torque level are computed in pu according to the minimum and maximum limits corresponding to that torque level. The pu speed vector is computed as follows:

$$rpm_{norm}(i) = \frac{rpm_{cm}(i) - rpm_{min}(i)}{rpm_{max}(i) - rpm_{min}(i)} \quad (4.62)$$

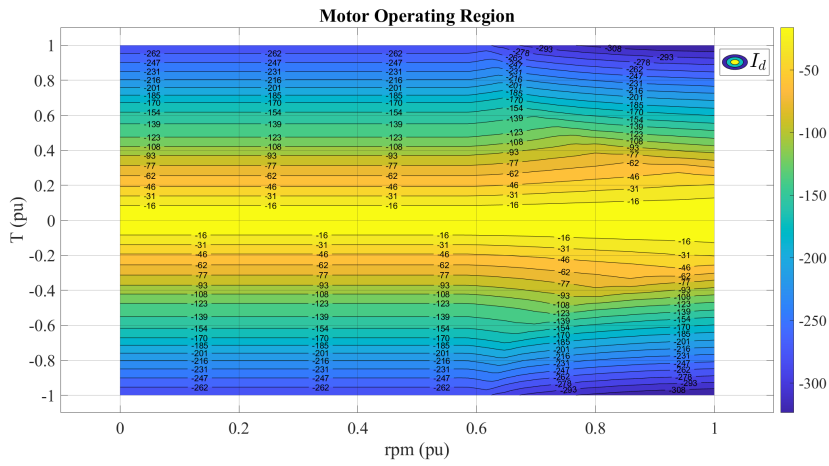
where rpm_{max} and rpm_{min} are the maximum and minimum speed for the torque level i .

• Torque normalization

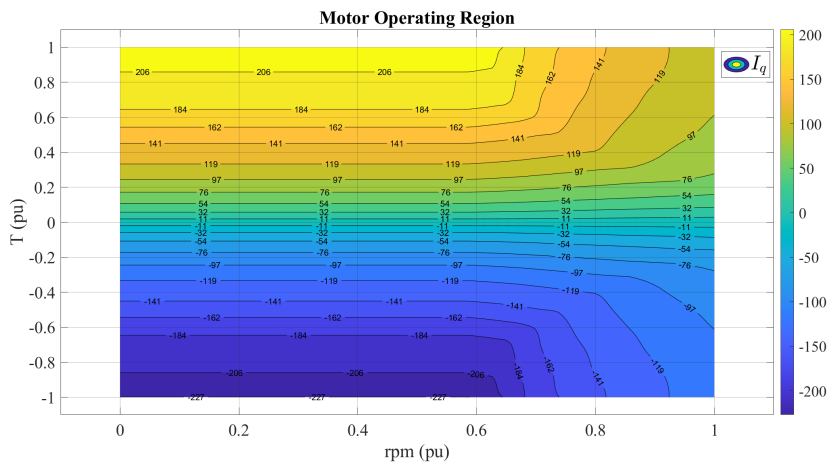
Since it is not convenient to have only one axis of the map in pu also the torque-axis is normalized in pu considering T_{max} as 1 pu. Therefore, by calling with $T_{e,cm}$ the vector of the torque levels, it can be normalized as:

$$T_{norm} = \frac{T_{e,cm}}{T_{max}} \tag{4.63}$$

After torque normalization the dq current maps are finally obtained and ready to be implemented in the motor control algorithm since this map is defined on a regular domain. The resultin normalized maps are shown in Figure 4.34.



(a) I_d control map



(b) I_q control map

Figure 4.34: Currents Control Maps of IPM - Speed and Torque Normalization.

4.6.4 PI Controllers

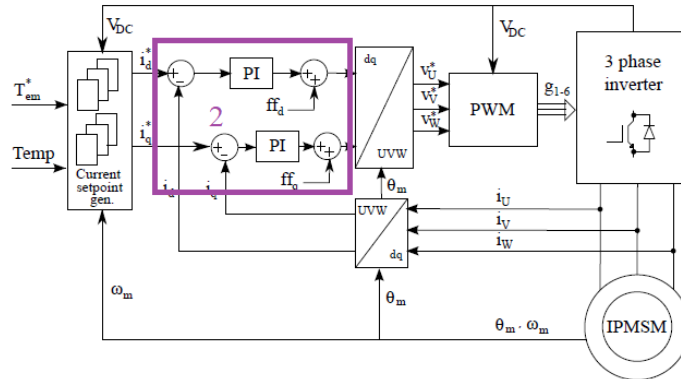


Figure 4.35: 4D FOC block scheme part 2[5].

Due to its anisotropic characteristics, the IPM motor requires a control for both d and q axis.

Once the motor model is correctly defined, the control is designed. For such design, a PI regulator with feed forward is chosen. The calibration of the PI is done through the following strategy:

$$\omega_b \ll 1/\tau_{VSI} \quad (4.64)$$

where τ_{VSI} is defined as $\tau_{VSI} = 1.5/f_{sw}$.

$$\begin{cases} k_{p,d} = l_d \omega_b \\ k_{i,d} \ll k_{p,d} \omega_b \end{cases} \quad (4.65)$$

$$\begin{cases} k_{p,q} = l_q \omega_b \\ k_{i,q} \ll k_{p,q} \omega_b \end{cases} \quad (4.66)$$

where l_d and l_q are the differential inductances and ω_b is the bandwidth of the PI regulator. According to these equation and to input data retrieved, the calibration of the FOC controller has led to the results shown in Table 4.1.

Table 4.1: PI controllers calibration

Symbol	Quantity	Unit
τ_{VSI}	125	μs
l_d	0.098	mH
l_q	0.401	mH
ω_b	4400	rad/s
$k_{p,d}$	0.431	V/A
$k_{i,d}$	189.728	V/A
$k_{p,q}$	1.764	V/A
$k_{i,q}$	776.336	V/A

In FOC control design, a particular care must be taken to select l_d and l_q , since these values are fixed in the calibration, while they are actually varying depending on the torque, and so the actual working point of the machine, required. To impose a general control strategy, l_d and l_q must be chosen such that a trade-off between linear and saturation conditions is achieved. This because the actual current control bandwidth varies as current varies and so calibrating FOC control according to the linear region will

lead to a much higher bandwidth than expected in saturation conditions, while for FOC control according to saturation region leads to a very low bandwidth when the machine works in linear region. Torque requirement usually is most of the time such that high currents that lead to saturation conditions are rarely achieved. Therefore for a proper control, it is possible to select the l_d value in the linear region, as well as l_q .

The feed-forward term is obtained by considering the known contribution of the resistance equal to $R_s \cdot i_{dq}$.

4.6.5 Voltage reference and duty cycle computation

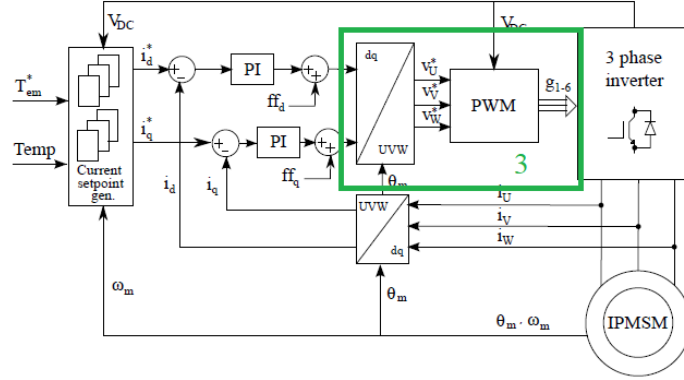


Figure 4.36: 4D FOC block scheme part 3[5].

The last step to be performed is the evaluation of the reference voltages $v_{abc}^* = [v_a^*, v_b^*, v_c^*]$ that are needed to calculate the duty cycles for the inverter. From the reference voltages in (dq) stator frame, the rotational transformation is performed to get the $(\alpha\beta)$ component and, in the end, the Clarke transformation is used to evaluate the voltages in (abc) components. The v_{abc}^* value are used in the generation of the duty cycles $d_{abc}^* = [d_a^*, d_b^*, d_c^*]$, using the chosen technique, and translated in instantaneous command to the inverter.

The input of this last block of the control structure are the output of the two controllers performing dq currents regulation: $(v_{d,out}, v_{q,out})$. However, it is necessary to understand which angle should be used for the rotational transformation from (dq) to $(\alpha\beta)$. Indeed, using the d -axis position, at time step (k) for commands that will be applied at time step $(k + 1)$ is incorrect. In addition to the execution delay of digital controller, it is also necessary to consider the delay introduced by the power converter when performing the pulse-width modulation (PWM), usually assumed as half time of the switching period.

To compensate the delay a phase advancing technique is applied. Practically, a rotational transformation that uses as angle the equivalent delay introduced is implemented. This angle is computed as:

$$\theta_{PA} = 1.5T_s\omega \quad (4.67)$$

where T_s is the switching period.

$$\begin{bmatrix} v_\alpha^* \\ v_\beta^* \end{bmatrix} = \begin{bmatrix} \cos(\theta_{PA}) & -\sin(\theta_{PA}) \\ \sin(\theta_{PA}) & \cos(\theta_{PA}) \end{bmatrix} \begin{bmatrix} v_{d,out} \\ v_{q,out} \end{bmatrix} \quad (4.68)$$

Finally, the v_{abc}^* are calculated as:

$$\begin{bmatrix} v_a^* \\ v_b^* \\ v_c^* \end{bmatrix} = \begin{bmatrix} 1 & 0 & 1 \\ -\sin(30) & \cos(30) & 1 \\ -\sin(30) & -\cos(30) & 1 \end{bmatrix} \begin{bmatrix} v_\alpha^* \\ v_\beta^* \end{bmatrix} \quad (4.69)$$

Lastly, the duty cycles that are used to define the instantaneous state of power converter must be obtained from the voltage reference in (abc) coordinates and from the DC-link voltage value. Any of the PWM techniques can be implemented. The adopted technique is the carrier-based "MinMax" modulation. The technique guarantees, in linear condition, a peak voltage output of $v_{dc}/\sqrt{3}$, that is $\sqrt{3}/2 = 0.866$ higher then the value reachable without the zero-sequence injection, equal to $v_{dc}/2$. The effect of the zero-sequence is shown in Figure 4.37.

The zero sequence voltage v_{zs} is computed as the average between the instantaneous maximum and minimum (abc) references voltages. In detail v_{abc}^* reference voltages are normalized over v_{dc} to obtain the normalized reference voltages $v_{abc,norm}^*$. The zero-sequence is thus computed as:

$$v_{zs} = -\frac{v_{max}(v_{a,norm}^*, v_{b,norm}^*, v_{c,norm}^*) + v_{min}(v_{a,norm}^*, v_{b,norm}^*, v_{c,norm}^*)}{2} \quad (4.70)$$

$$v_{zs} = -\frac{v_{mean}(v_{a,norm}^*, v_{b,norm}^*, v_{c,norm}^*)}{2} \quad (4.71)$$

Finally, the duty cycles d_{abc}^* are calculated as:

$$\begin{aligned} d_a^* &= \frac{1}{2} + v_{a,norm}^* + v_{zs} \\ d_b^* &= \frac{1}{2} + v_{b,norm}^* + v_{zs} \\ d_c^* &= \frac{1}{2} + v_{c,norm}^* + v_{zs} \end{aligned} \quad (4.72)$$

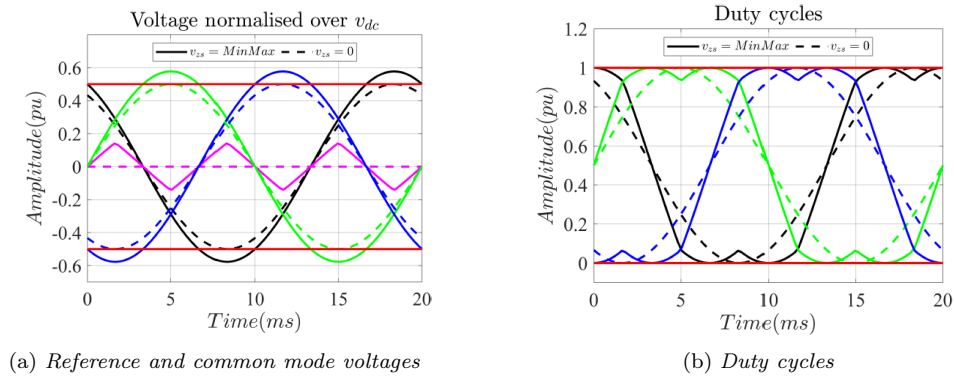


Figure 4.37: Min-Max modulation.

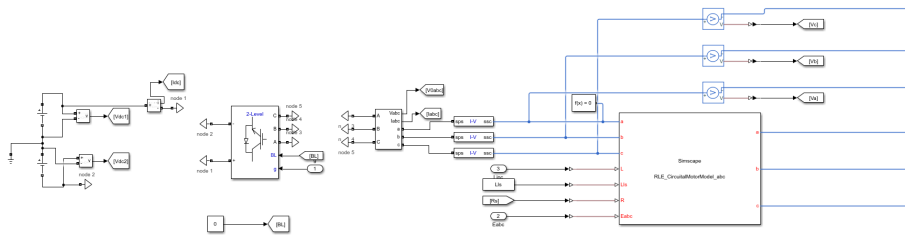
Chapter 5

Simulation Results

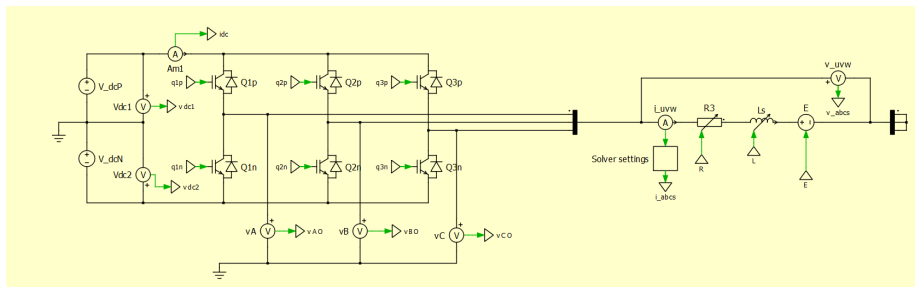
The VBR model and 4D FOC control scheme have been validated by means of simulation results. In detail, the VBR model is developed in Matlab/Simulink environment and in PLECS, taking as reference the PLECS's results to verify the correct exploitation of the Matlab/Simulink environment. Then the Matlab/Simulink VBR model is compared with the benchmark model, previously described in section 3.2, to validate it's availability in simulate synchronous motors.

The 4D FOC motor control algorithm has been totally developed in the C environment. In the first stage, the algorithm has been debugged and validated in Matlab/Simulink and PLECS (taken also in this case as benchmark) environments, thus performing the simulation validation. Secondly, the 4D FOC developed performances are compared with an existing DFVC scheme ones, that are considered the references. The results obtained permits to attest if the 4D FOC developed represents also a valid control solution for the efficient control of the e-Drive taken into account.

5.1 VBR Model Validation



(a) *Matlab/Simulink model*



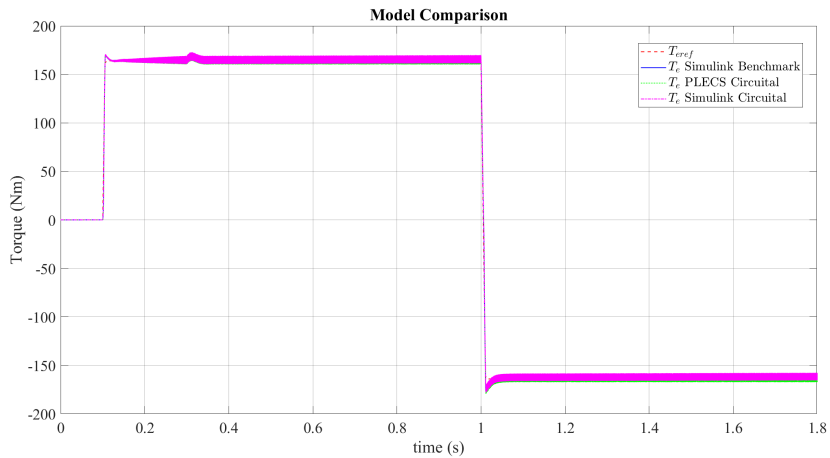
(b) *PLECS model*

Figure 5.1: VBR model in Matlab/Simulink and PLECS environment.

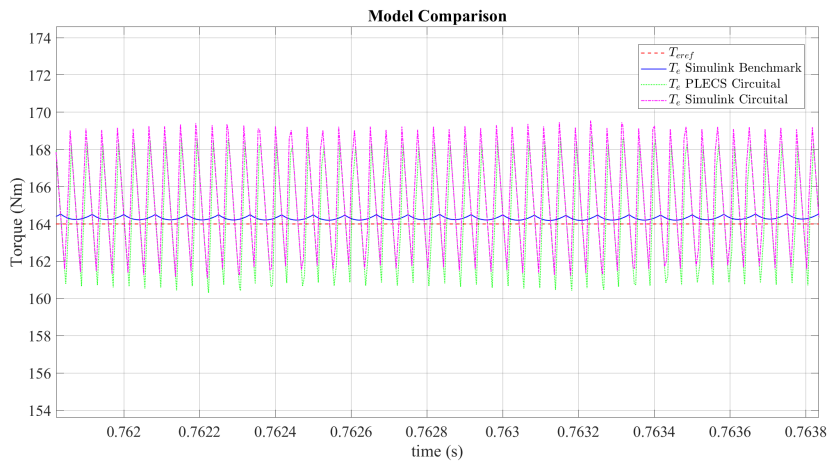
The complete model of the powertrain comprehensive of battery, inverter and e-Motor is build both in Matlab/Simulink (Figure 5.1(a)) and PLECS (Figure 5.1(b)).

To test the behaviour of the model build and of the components used, simulations with the same DFVC control algorithm, utilized in the benchmark model, are done. Also the same data, referred to the hardware testing platform defined in the preliminary stage, are used, in this way it is possible to analyse the difference between the two strategies of modelization that constitutes the only difference between the simulations.

The test chosen to validate model consist of asking as references $T^* = T_{max} = 165Nm$, $rpm^* = 2000rpm$ (so $w_m < w_{base}$), the verify the behaviour of the model at its limit as motor and then abruptly asking for $T^* = -T_{max} = -165Nm$, in order to analyze how the model react to the maximum possible torque variation with a slope of $3000 Nm/s$ and finally verify the behaviour of the model at its limit as generator. The results are shown in Figure 5.2.



(a) Max torque response as motor and as generator



(b) Zoom-in

Figure 5.2: Torque response of the bechmark model and VBR model in Simulink and PLECS.

As can be seen the models follow the reference, the main difference between them lies on the switching ripple, which is not present in the benchmark non circuital model where the switching dynamic is not simulated. It can be also noted in the Zoom-in 5.2(b) that there is a slightly difference between the Simulink and PLECS circuital model caused by the different solver adopted by the two different environment as also previously highlighted in Figure 3.11 during the block selection and evaluation of the e-Motor (3.3.2).

This simulation result makes possible to affirm that the VBR model developed is consistent from what expected by the benchmark model and also the component chosen for the Simulink model results coherent with the PLECS reference as another confirm.

From now on all the simulations reported are carried out on the Matlab/Simulink VBR model.

5.2 4D FOC validation

5.2.1 Control Algorithm

The 4D FOC algorithm has been implemented on a user-made state machine in order to guarantee a proper initialization of all control variables. A schematic view of the implemented state machine is shown in Figure 5.3.

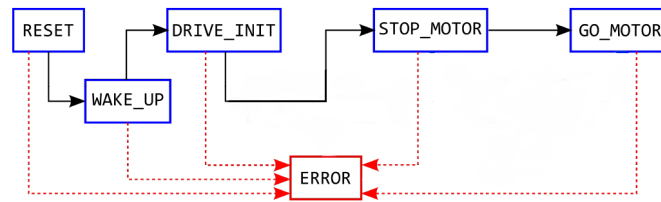


Figure 5.3: Implemented state machine.

According to Figure 5.3 the state machine is structured in seven states as reported in the following. To move from one state to another one, several human-to-machine interface (HMI) buttons are use.

- **RESET**: in this state the PWM is disabled and the duty cycles are initialized at their default value ($d_a=d_b=d_c=0.5$). If the HMI button **START** is pressed, the state machine move to **WAKE_UP**.
- **WAKE_UP**: in this state the dc voltage is checked to evaluate that this has reached a proper value. When the DC-link voltage has reached a specific threshold, the state machine automatically moves to the state **DRIVE_INIT**.
- **DRIVE_INIT**: in this state the offset of the current sensor is evaluated in order to be properly compensated while the control code is running. When the offset have been evaluated, the state machine automatically move to the state **STOP_MOTOR**.
- **STOP_MOTOR**: in this state, the motor control algorithm is ready to be started. Therefore, all the control variables are properly initialized and until the HMI button **GO** is pressed, the state machine remains in this state. The state machine moves to the state **GO_MOTOR**.
- **GO_MOTOR**: in this state the 4D FOC scheme is operated. To stop the motor control algorithm, it is necessary to press the HMI button **Err**. In this way, the state machines moves to the state **ERROR**.
- **ERROR**: this state is called when the protection system of the drive detect a fault (e.g., overcurrent) or when the HMI button **Err** is presse. In this state the PWM is disabled and the duty cycles are reset to thei default value. TO come back to the state **RESET**, it is necessary to press the HMI button **Reset**.

The writing of the code requires the discrete time form of all the blocks needed to implement the 4D FOC. In the digital control, time is ruled by the switching frequency f_{sw} . To better understand the discrete form of an equation, a basic example is provided.

Let's consider the integral of a generic function $x(t)$ defined in the continuous time domain:

$$y(t) = \int x(t)dt \quad (5.1)$$

Moving in Laplace domain the equation becomes:

$$y(s) = \frac{x(s)}{s} \quad (5.2)$$

Finally, by moving to the discrete time domain, 5.2 becomes:

$$\begin{aligned} y(k) &= y(k-1) + T_s \cdot x(k) \\ y(k) &= +T_s \cdot x(k) \end{aligned} \quad (5.3)$$

5.2.2 Input Signals Elaborations

The feedback signals of the motor control algorithm are: phase currents, DC-link voltage and rotor mechanical position. This feedback must be elaborated in order to be properly used in the control algorithm.

The implemented C-code for elaborating the input signals is reported in the following:

1. *Acquisition of currents $U(0:2)$, voltage $U(3)$ and mechanical position $U(4)$*

```
input.ch0 = U(0);
input.ch1 = U(1);
input.ch2 = U(2);
vdc = U(3);
theta_mec = U(4);
```

2. *Removing offset of current channels evaluated in DRIVE_INIT state*

```
iabc.a = input.ch0 - offset_in.ch0;
iabc.b = input.ch1 - offset_in.ch1;
iabc.c = input.ch2 - offset_in.ch2;
```

3. *Input Data Elaboration*

- (a) *Electric angle*

```
SinCos(&theta_mec, &sc_theta_mec);
theta_elt = theta_mec * pp - theta_off;
SinCos(&theta_elt, &sc_theta_elt);
```

- (b) *Speed computation using PLL*

```
pll(sc_theta_mec, &pll_theta_mech);
```

- (c) *dc link voltage filtering*

```
vdc = low_pass_filter(vdc,vdc_filt,double_pi*500.0*Ts);
vdc_filt = vdc;
```

- (d) *Phase voltages*

```
vabc.a=(vdc*one_over_three)*(2.0*duty.a-duty.b-duty.c);
vabc.b=(vdc*one_over_three)*(2.0*duty.b-duty.c-duty.a);
vabc.c=(vdc*one_over_three)*(2.0*duty.c-duty.b-duty.a);
```

4. Rotation to obtain $\alpha\beta$ variables

```
DirectClarke(&vabc, &vaplhabeta);
DirectClarke(&iabc, &ialphabeta);
```

5.2.3 4D FOC Control: control blocks implemented in the state GO_MOTOR

In the following is reported the implementation of the control modules actively operated in the state GO_MOTOR.

1. Current set point generation

(a) Definition of the extremes of interpolation

```
nm = wm_filt*rad2rpm;
index_nm_ceil = ceil(nm/nm_step);
index_nm_floor = floor(nm/nm_step);
nm_ceil = index_nm_ceil*nm_step;
nm_floor = index_nm_floor*nm_step;
Vdc_floor = floor(vdc_filt/vdc_step)*vdc_step;
Vdc_ceil = ceil(vdc_filt/vdc_step)*vdc_step;
Ts_floor = floor(Ts/Ts_step)*Ts_step;
Ts_ceil = ceil(Ts/Ts_step)*Ts_step;
```

(b) Maximum Torque definition and reading of LUTs

These part of the code is repeated for every combination of Vdc_floor(Ts_floor), Vdc_floor(Ts_ceil), Vdc_ceil(Ts_floor), Vdc_ceil(Ts_ceil).

Only one example is reported.

```
if (Vdc_floor==250){
if (Ts_floor==50){

Tmax1=Tmax_250V_m50C[index_nm1];
Tmax2=Tmax_250V_m50C[index_nm2];
if (Tmax1!=Tmax2){
Tmax=Tmax2+((Tmax1-Tmax2)/(nm_ceil-nm_floor))*(nm-nm_floor);
if (fabs(Te_ref)>Tmax){
if (Te_ref>0){
Te_ref=Tmax;
}
if (Te_ref<0){
Te_ref=-Tmax;
}
}
}

ref1.d=read_two_dim_lut(&Id_250V_m50C[0][0],nm/nmax,Te_ref/Tmax1,DN,INV_DN,
DT,INV_DT,N_MAX,N_MIN,T_MAX,T_MIN,NPOINTS_N);
ref1.q=read_two_dim_lut(&Iq_250V_m50C[0][0],nm/nmax,Te_ref/Tmax1,DN,INV_DN
```

```
,DT,INV_DT,N_MAX,N_MIN,T_MAX,T_MIN,NPOINTS_N);

ref2.d=read_two_dim_lut(&Id_250V_m50C[0][0],nm/nmax,Te_ref/Tmax2,DN,INV_DN,
,DT,INV_DT,N_MAX,N_MIN,T_MAX,T_MIN,NPOINTS_N);
ref2.q=read_two_dim_lut(&Iq_250V_m50C[0][0],nm/nmax,Te_ref/Tmax2,DN,INV_DN,
,DT,INV_DT,N_MAX,N_MIN,T_MAX,T_MIN,NPOINTS_N);
if (Tmax1==Tmax2){
Tmax=Tmax_250V_m50C[index_nm1];

    if (fabs(Te_ref)>Tmax){
        if (Te_ref>0){
Te_ref=Tmax;
        }
    if (Te_ref<0){
Te_ref=-Tmax;
        }
    }

map1.d=read_two_dim_lut(&Id_250V_m50C[0][0],nm/nmax,Te_ref/Tmax,DN,INV_DN,
,DT,INV_DT,N_MAX,N_MIN,T_MAX,T_MIN,NPOINTS_N);
map1.q=read_two_dim_lut(&Iq_250V_m50C[0][0],nm/nmax,Te_ref/Tmax,DN,INV_DN,
,DT,INV_DT,N_MAX,N_MIN,T_MAX,T_MIN,NPOINTS_N);
}
if (Tmax1!=Tmax2){
map1.d=ref2.d+((ref1.d-ref2.d)/(nm_ceil-nm_floor))*(nm-nm_floor);
map1.q=ref2.q+((ref1.q-ref2.q)/(nm_ceil-nm_floor))*(nm-nm_floor);      }
}
}
```

(c) *LUTs linear interpolation*

```
//Vdc floor
if (Ts_ceil!=Ts_floor){
mapT1.d=map1.d+((map2.d-map1.d)/(Ts_ceil-Ts_floor))*(Ts-Ts_floor);
mapT1.q=map1.q+((map2.q-map1.q)/(Ts_ceil-Ts_floor))*(Ts-Ts_floor);
}
if (Ts_ceil==Ts_floor){
mapT1.d=map1.d;
mapT1.q=map1.q;
}
//Vdc ceil
if (Ts_ceil!=Ts_floor){
mapT2.d=map3.d+((map4.d-map3.d)/(Ts_ceil-Ts_floor))*(Ts-Ts_floor);
mapT2.q=map3.q+((map4.q-map3.q)/(Ts_ceil-Ts_floor))*(Ts-Ts_floor);
}
if (Ts_ceil==Ts_floor){
mapT2.d=map3.d;
mapT2.q=map3.q;
}

if (Vdc_ceil!=Vdc_floor){
mapTV.d=mapT1.d+((mapT2.d-mapT1.d)/(Vdc_ceil-Vdc_floor))*(vdc-Vdc_floor);
mapTV.q=mapT1.q+((mapT2.q-mapT1.q)/(Vdc_ceil-Vdc_floor))*(vdc-Vdc_floor);
}
if (Vdc_ceil==Vdc_floor){
mapTV.d=mapT1.d;
}
```

```
mapTV.q=mapT1.q;
}
```

```
PI_id.ref=mapTV.d;
PI_iq.ref=mapTV.q;
```

2. PI regulators

```
// Current control
fb=700;
wb=2*pi*fb;
zeta=0.2;

PI_id.kp=wb*LdRated;
PI_id.ki=PI_id.kp*wb/10;

PI_iq.kp=wb*LqRated;
PI_iq.ki=PI_iq.kp*wb/10;

// PI_d regulator

PI_id.lim=vdc/(sqrt(3));
PI_id.fbk=idq.d;
PI_id.err=PI_id.ref-PI_id.fbk;
PI_id.prop=PI_id.err*PI_id.kp;
PI_id.ffw=Rs*PI_id.ref*0.0;
PI_id.prop=PI_id.prop+PI_id.ffw;
if(PI_id.prop>PI_id.lim){
PI_id.prop=PI_id.lim;
}
if(PI_id.prop<-PI_id.lim){
PI_id.prop=-PI_id.lim;
}
PI_id.intg=PI_id.err*PI_id.ki*Tsw+PI_id.intg;
if(PI_id.intg>(PI_id.lim-PI_id.prop)){
PI_id.intg=PI_id.lim-PI_id.prop;
}
if(PI_id.intg<-(PI_id.lim+PI_id.prop)){
PI_id.intg=-(PI_id.lim+PI_id.prop);
}

PI_id.out=PI_id.prop+PI_id.intg;

// PI_q regulator

if (PI_id.out*PI_id.out<(vdc*vdc)/3){
PI_iq.lim=sqrt((vdc*vdc)/3-PI_id.out*PI_id.out);
}
if (PI_id.out*PI_id.out>(vdc*vdc)/3){
PI_iq.lim=0.0;
}
PI_iq.fbk=idq.q;
PI_iq.err=PI_iq.ref-PI_iq.fbk;
PI_iq.prop=PI_iq.err*PI_iq.kp;
```

```

PI_iq.ffw=Rs*PI_iq.ref*0.0;
PI_iq.prop=PI_iq.prop+PI_iq.ffw;
if(PI_iq.prop>PI_iq.lim){
PI_iq.prop=PI_iq.lim;
}
if(PI_iq.prop<-PI_iq.lim){
PI_iq.prop=-PI_iq.lim;
}
PI_iq.intg=PI_iq.err*PI_iq.ki*Tsw+PI_iq.intg;
if(PI_iq.intg>(PI_iq.lim-PI_iq.prop)){
PI_iq.intg=PI_iq.lim-PI_iq.prop;
}
if(PI_iq.intg<-(PI_iq.lim+PI_iq.prop)){
PI_iq.intg=-(PI_iq.lim+PI_iq.prop);
}

PI_iq.out=PI_iq.prop+PI_iq.intg;

```

3. Phase Advancing of Voltage References and Inverse Rotation

```

theta_pa=1.5*Tsw*wm_filt*pp;
SinCos(&theta_pa,&sincos_theta_pa);

vRefdq.d=PI_id.out*sincos_theta_pa.cos-PI_iq.out*sincos_theta_pa.sin;
vRefdq.q=PI_id.out*sincos_theta_pa.sin+PI_iq.out*sincos_theta_pa.cos;

inverse_rot(vRefdq,sincos_theta,&vRefalphabeta);
InverseClarke00(&vRefalphabeta,&vRefabc);

```

5.3 Matlab-Simulink simulation

The main machine parameters are reported in Table 5.1.

Table 5.1: Motor and Inverter parameters.

Name	Symbol	Quantity	Unit
Motor			
Pole Pairs	pp	5	-
Stator Resistance	R_s	0.01	Ω
Stator Leakage Inductance	L_{ls}	0.003	mH
Maximum Torque	T_{max}	165	Nm
Inverter			
Switching Frequency	f_{sw}	12	kHz
Dead Time	t_{DT}	2	μs
DC-link voltage	v_{dc}	400	V

5.3.1 Maximum Torque per Speed (MTPS)

The maximum torque per speed profile in both motoring and generator operations has been tested. The maximum torque level has been requested from 0 rpm to the maximum speed of 12000 rpm. In motoring operation the simulation results are shown in Figure

5.4. It is noted how the 4D FOC scheme is able to guarantee the maximum torque production in MTPA and FW with MTPV operation.

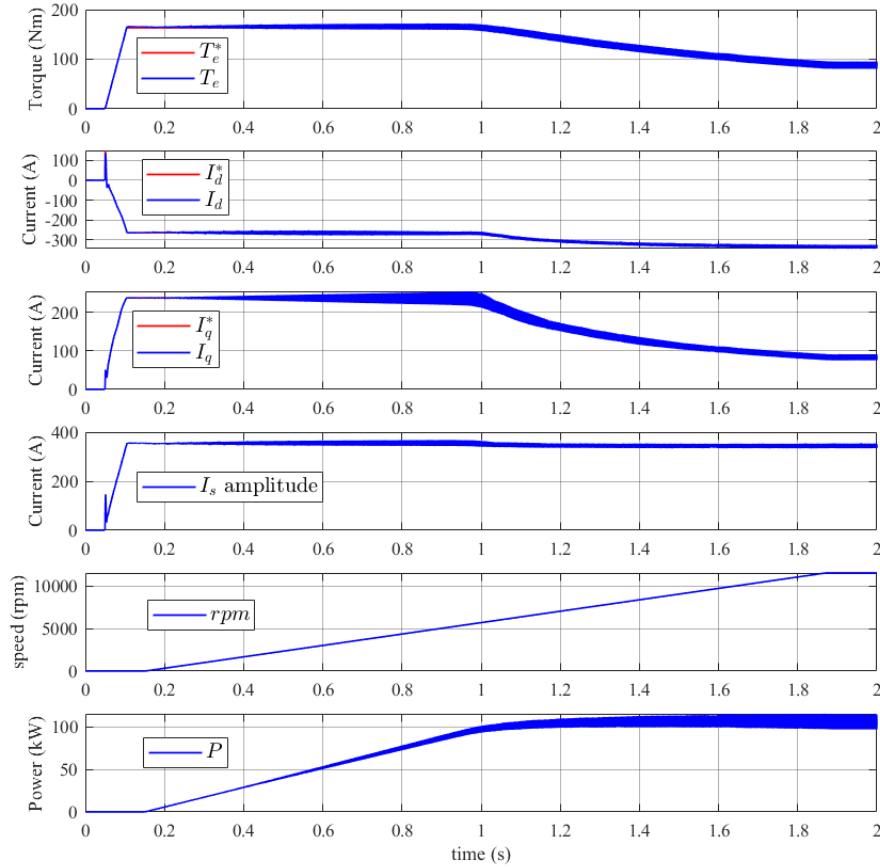


Figure 5.4: MTPS in motoring operation at rated parameters, $V_{dc} = 400V$ $T_s = 25^\circ\text{C}$.

where P stands for the mechanical power.

As soon as the state GO_MOTOR is operated the torque reference has been set to the maximum torque level T_{max} . It is noted how the amplitude of the phase currents reach their maximum value of 355A, corresponding to the last point of the MTPA profile and CL. The speed increase up to the maximum value of 12000 rpm, with a slope of 10000 rpm/s.

It is noted the outstanding torque controllability in the full speed range. In addition, when the MTPV operation is performed, it is noted how the current amplitude decreases to follow the MTPV profile.

The maximum torque per speed in generator operation is shown in Figure 5.5. All the consideration made for the torque-speed profile in motoring are still valid. The only difference is that the torque reference is negative.

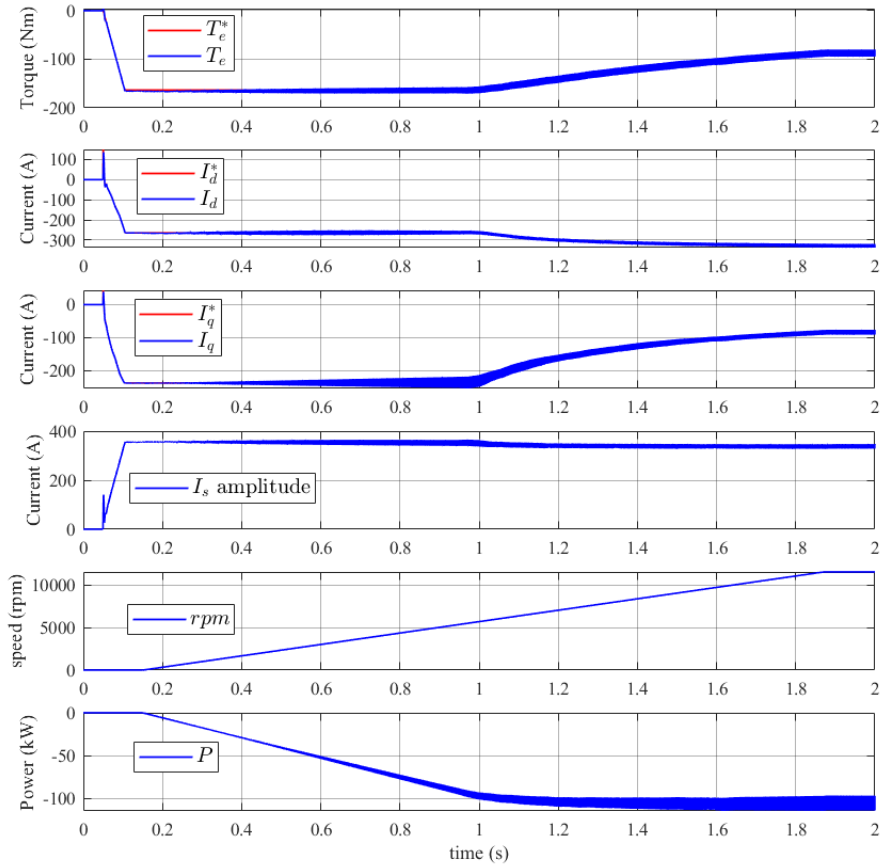


Figure 5.5: MTPS in generator operation at rated parameters, $V_{dc} = 400V$ $T_s=25^\circ C$.

One of the main advantages about the 4D FOC control scheme is the capability to overcome the issues due to machine electric parameters variation with temperature and also unconcerned to the variation of the DC-link voltage. So it is interesting to analyze the MTPS behaviour at different temperatures and different DC-link voltages.

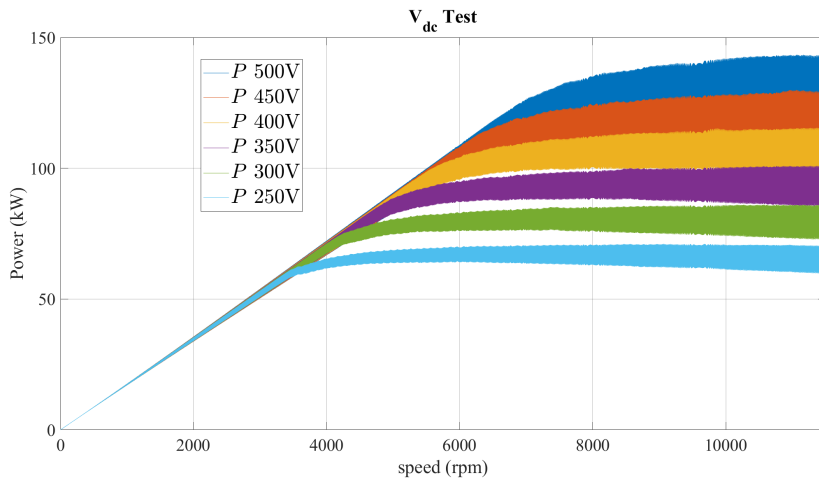
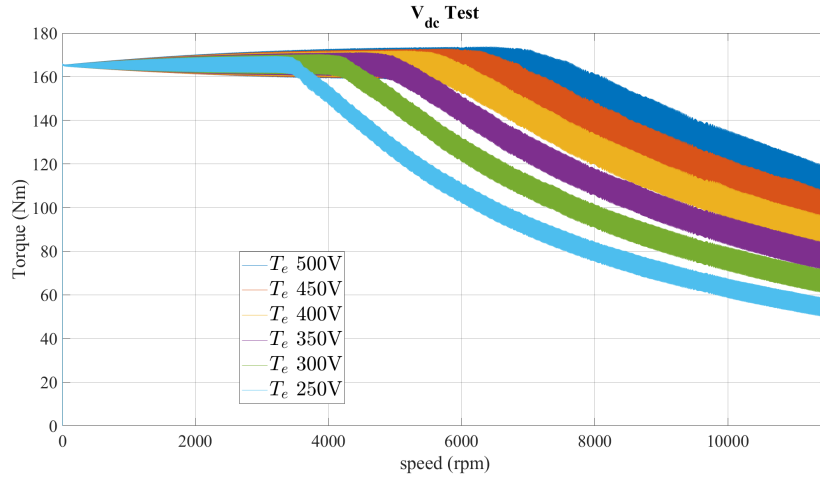
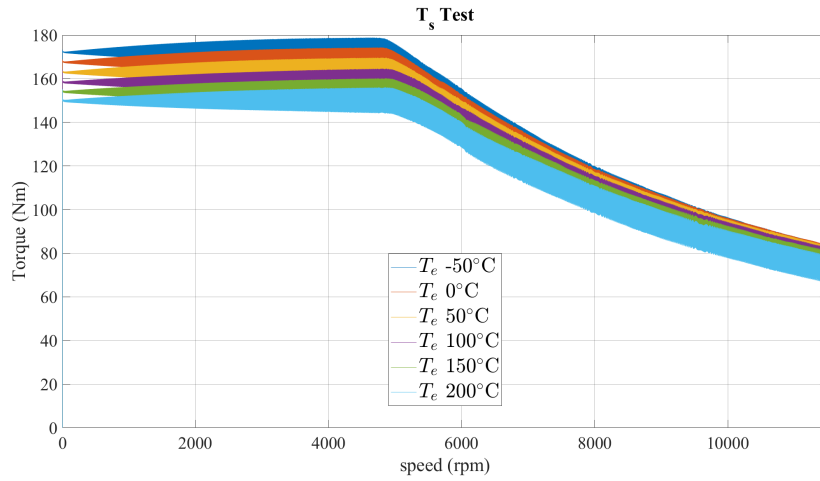


Figure 5.6: MTPS power evaluation for different DC-link voltages.



(a) $V_{dc}=(250V,300V,350V,400V,450V,500V)$
 $T_s=25^\circ C$



(b) $V_{dc}=400V$
 $T_s=(-50^\circ C,0^\circ C,50^\circ C,100^\circ C,150^\circ C,200^\circ C)$

Figure 5.7: MTPS evaluation for different DC-link voltages and different temperature of the magnets.

The results obtained confirm a good behaviour of the FOC control also in flux-weakening region. In figure 5.7(a) we can analyse how the increase of the DC-link voltage correspond to an extension of the MTPA region increasing the power available, as can be seen in Figure 5.6. Nevertheless the increase of the DC-link voltage cause a visible augment of the torque ripple. In figure 5.7(b) are presented the different behaviour due to the variation of the temperature of the magnets. In this simulations we assume that the temperature of the magnets is the same of the stator, so its change have two principal effects:

- Variation of the stator resistance \rightarrow correspond to an alteration in the maximum current of the motor and so the maximum torque available.
- Variation of the PM flux available \rightarrow correspond to an alteration in the starting point of the flux weakening region.

5.3.2 Stress Test

To demonstrate the high dynamic performance of 4D FOC torque controller, a square torque reference is imposed to the machine with a frequency of 10 Hz and a slew-rate of

3000 Nm/s, acting at a fixed speed of 2000 rpm, to be sure to be in the MTPA region. In this way, the dynamic performance controllability is proved at its maximum torque variation.

The evolution of the variable is the following, shown in Figure 5.8.

- The current amplitude is always positive and its value changes instantaneously only when reference torque is reversed.
- The mechanical power P , has the same sign of torque. Like for torque, its maximum and minimum values involves the maximum power per speed profile.

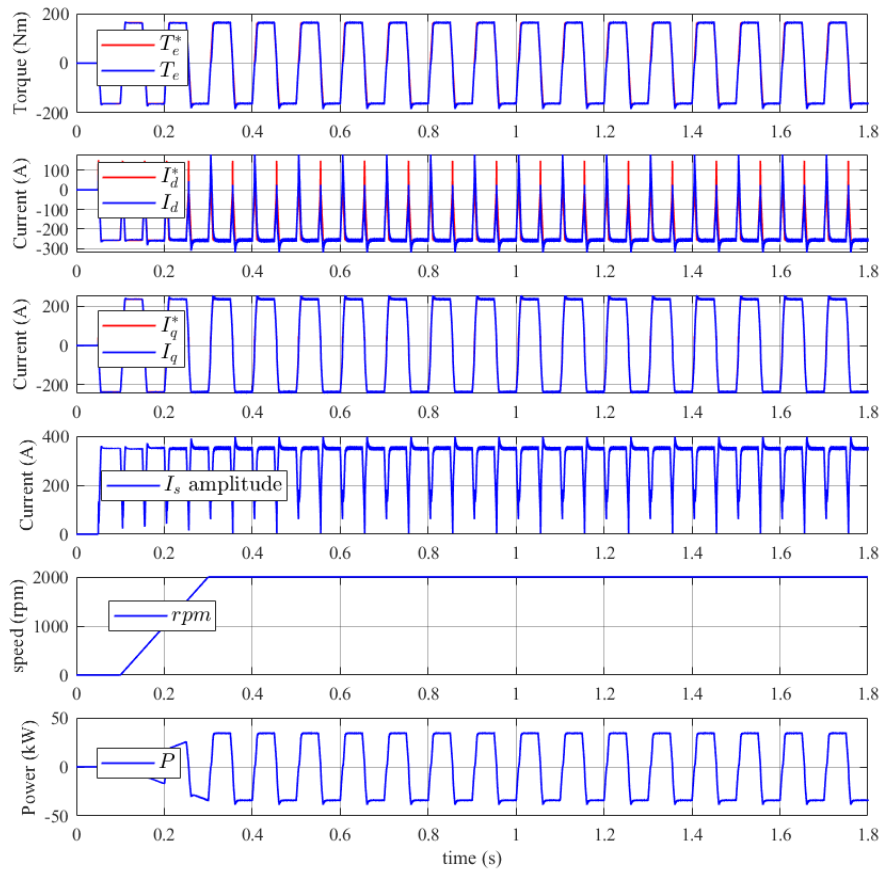


Figure 5.8: Square wave reference test at rated parameters, $V_{dc} = 400V$ $T_s=25^\circ C$.

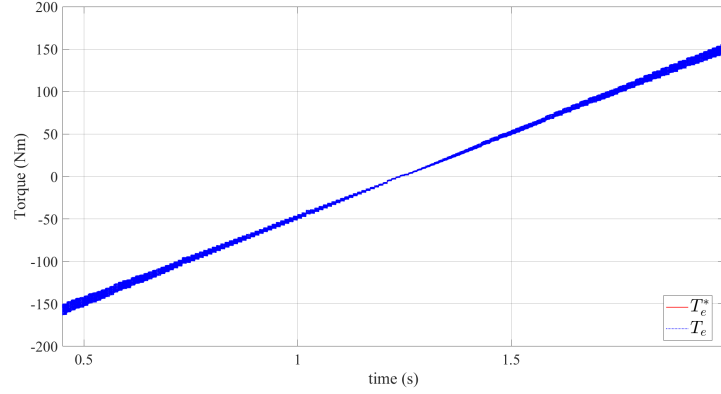
The square wave torque reference test represents the most stressfull operating condition of an e-Drive as consists of the alternating motor-generator operation at the theoretical torque limit of the machine.

It is noted the very good torque controllability while performing this stress test. In addition, it is highlighted how the torque reference is changed so fastly, such to hinder that the torque reaches its steady state value, nevertheless it is reached in all the speed range considered.

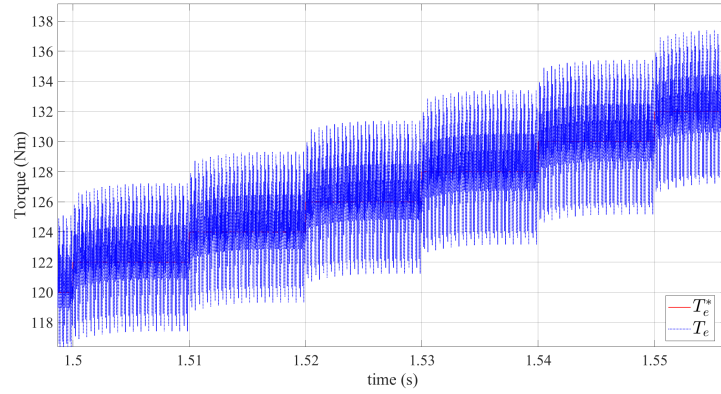
5.3.3 Accuracy Test

At the speed of 2000 rpm, a stair of reference torque values is applied and whose limits correspond to the maximum torque of the machine T_{max} . It is noted how the actual

torque is able to follow the reference in all its values with a ripple proportional to the absolute value of the torque requested. As can be seen in Figure 5.9(b) the ripple remains in an acceptable range of about 3% of the requested torque.



(a) Torque profile



(b) Zoom-in

Figure 5.9: Torque accuracy test, $V_{dc} = 400V$, $T_s = 25^\circ C$, 2000 rpm.

5.4 4D FOC vs DFVC

Assured that the 4D FOC can be a viable control scheme for the control of the powertrain taken into account, a performance comparison with the DFVC benchmark scheme is done. So we repeat the same test done previously only for the 4D FOC, also for the DFVC.

5.4.1 MTPS

The starting point is the evaluation of the MTPS for different temperature. The extreme of the magnets temperatures ($T_s = -50^\circ C$, $T_s = 200^\circ C$) are considered also than the rated one ($V_{dc} = 400V$, $T_s = 25^\circ C$).

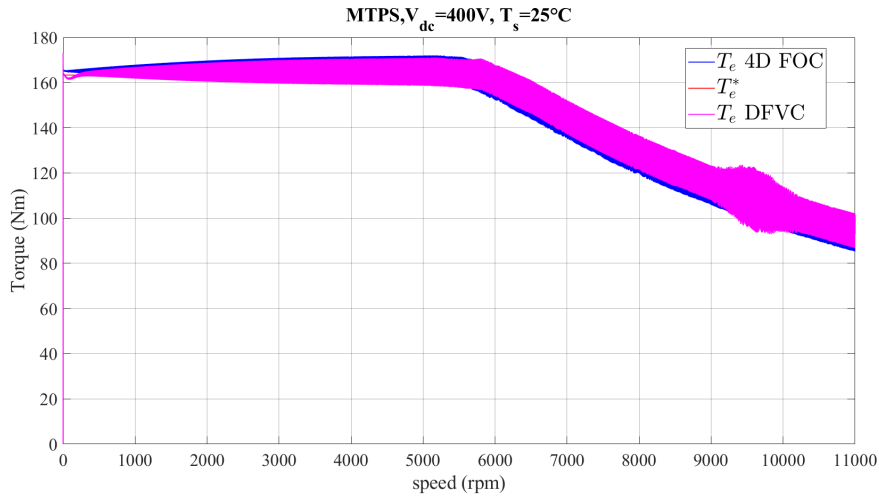
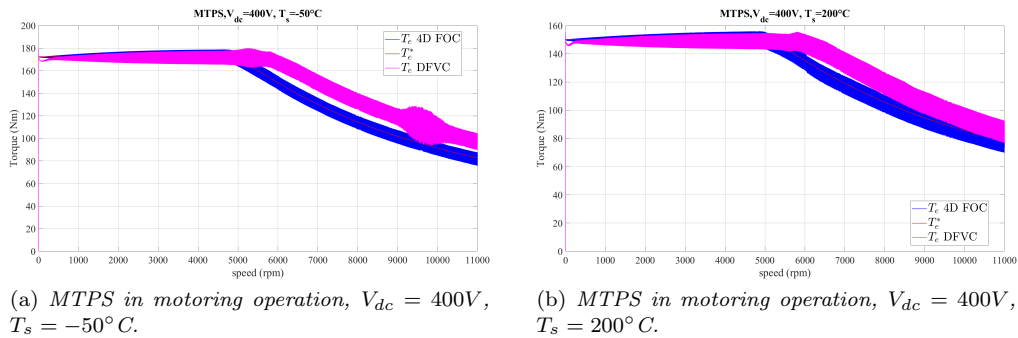


Figure 5.10: MTPS in motoring operation at rated parameters, $V_{dc} = 400V$ $T_s = 25^\circ C$.

Figure 5.10 show how for the rated parameters, at room temperature, both control techniques are able to efficiently follow the reference and they have almost the same behaviour. In contrary when the temperature differs from the rated one, whether it is less or greater, the DFVC is not able to follow the reference in the flux weakening region. Simulation results in Figure 5.11 attest how the 4D FOC control scheme is the only one that overcomes the issues due to machine electric parameters variation with temperature. It is important to highlight that in the development of the DFVC used in the simulations no attempt was made to implement a function that takes into account the temperature variation. So no general conclusion on the capability to follow the required torque at different temperatures of the DFVC scheme control can be drawn.



(a) MTPS in motoring operation, $V_{dc} = 400V$, $T_s = -50^\circ C$.

(b) MTPS in motoring operation, $V_{dc} = 400V$, $T_s = 200^\circ C$.

Figure 5.11: MTPS comparison in motoring operation at temperatures different from the room one.

5.4.2 Stress Test

Simulation results of the stress test comparison are reported in Figure 5.12 and a focus on the torque behaviour is visible in Figure 5.13.

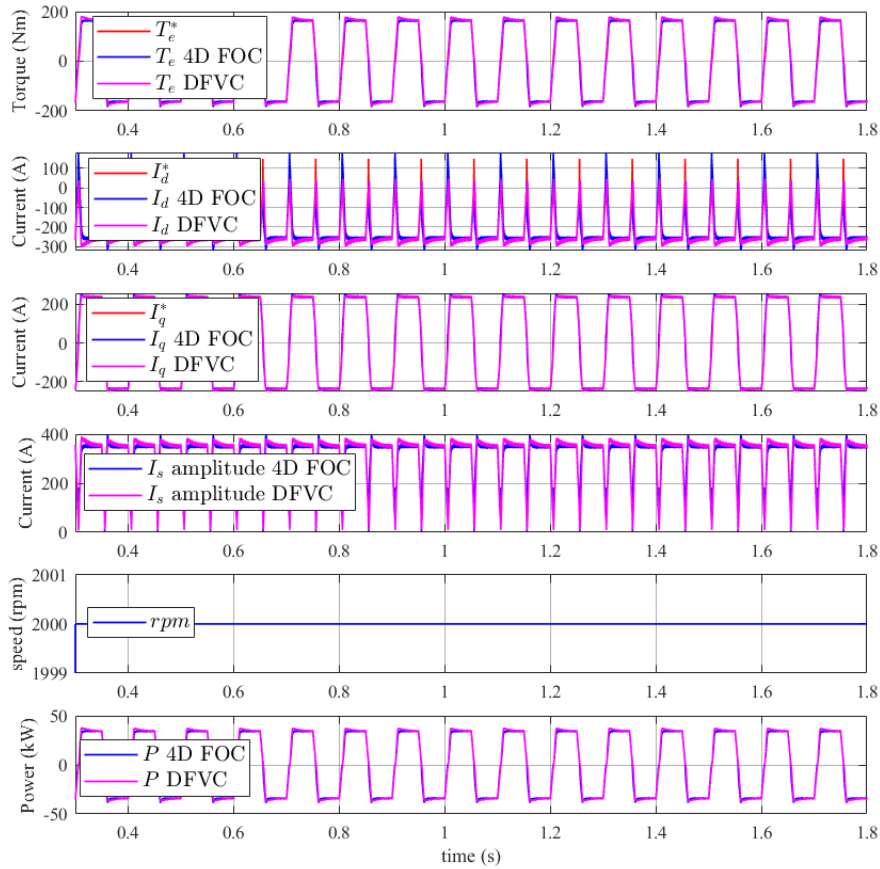


Figure 5.12: Square wave reference test comparison at rated parameters, $V_{dc} = 400V$, $T_s = 25^\circ C$.

Figure 5.12 shows that both control solutions are able to follow the torque reference and they have almost exactly the same behaviour in term of current distribution in the dq -axis. Figure 5.13 highlight that the DFVC has the same overshoot during the transition between motor and generator and vice versa. The 4D FOC presents a higher overshoot with respect to DFVC when the transition is from motor to generator and an almost absent one when the transition is from generator to motor.

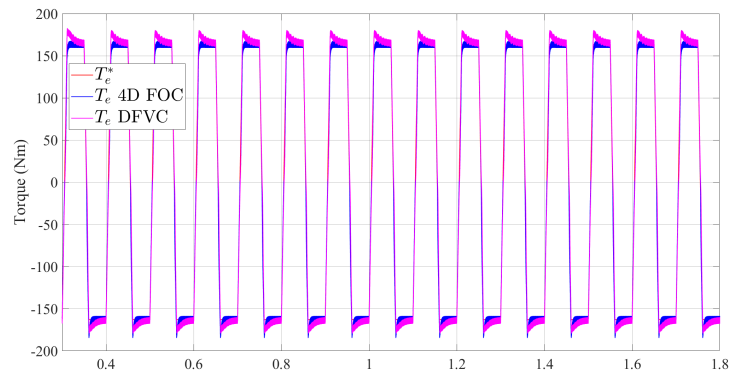


Figure 5.13: Square wave torque reference test 4D FOC vs DFVC.

5.4.3 Accuracy Test

Figure 5.14 shows the comparison between the accuracy tests of 4D FOC and DFVC control schemes. As can be noted DFVC results to have a better accuracy consistent in a visible reduced ripple respect to the 4D FOC's one.

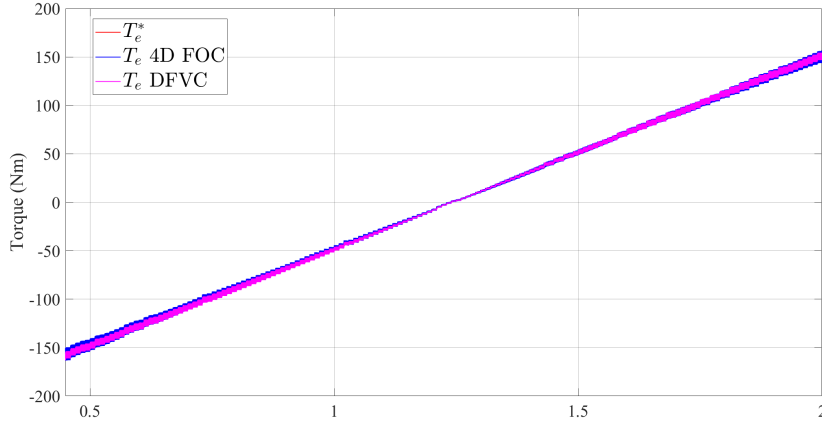


Figure 5.14: Torque accuracy test comparison, $V_{dc} = 400V$, $T_s = 25^\circ C$, 2000 rpm.

5.5 Fault Tolerance Analysis

As previously discussed, one of the main advantages of VBR circuit model of the e-Drive developed is the possibility to simulate some fault cases. The research for fault tolerant techniques is outside the scope of this thesis, is presented only the analysis of the behaviour of the control in a faulty stage.

5.5.1 Currents unbalance

The first fault situation analyzed regards the possibility that the MCU receives the three phase currents unbalanced. This can be caused by a fault of the current sensor or any error in the transmission of data between the current sensor and the MCU itself. The situation taken into account in the simulation contemplate an unbalance of $+2\%$ in favor of the a phase. In Figure 5.15 we analyze the behaviour of the two control techniques when the MTPS is requested.

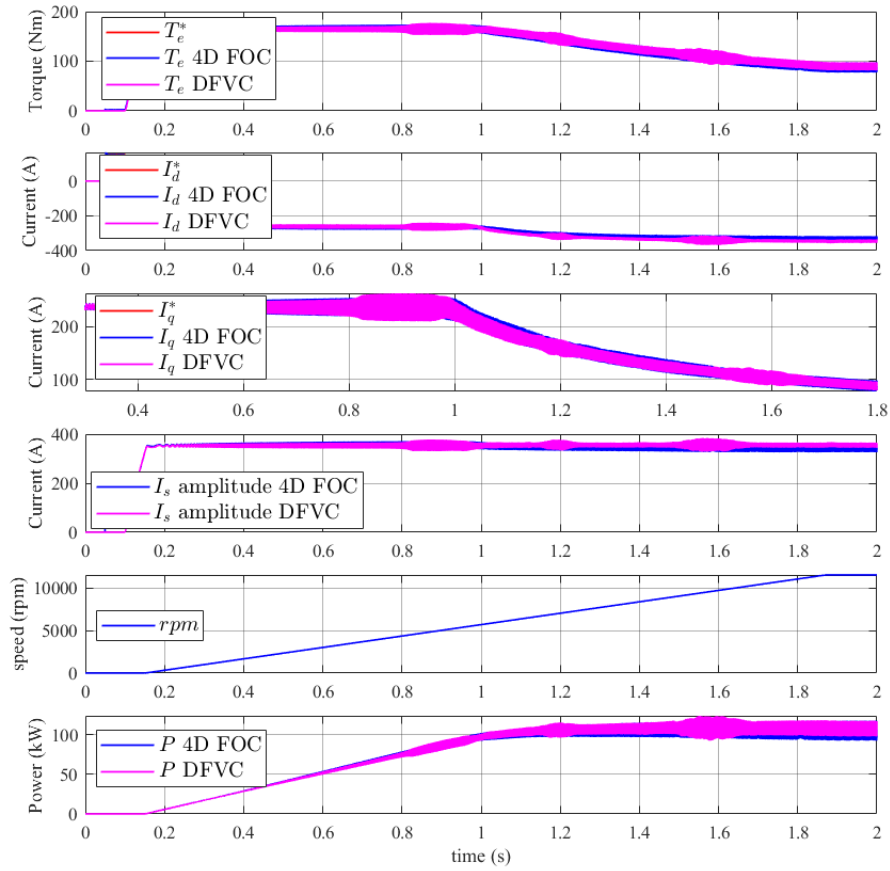
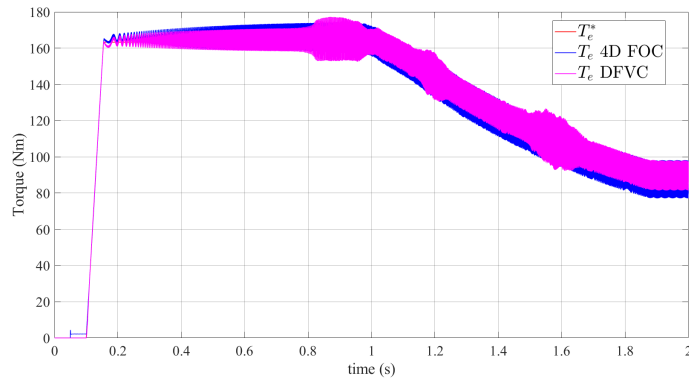


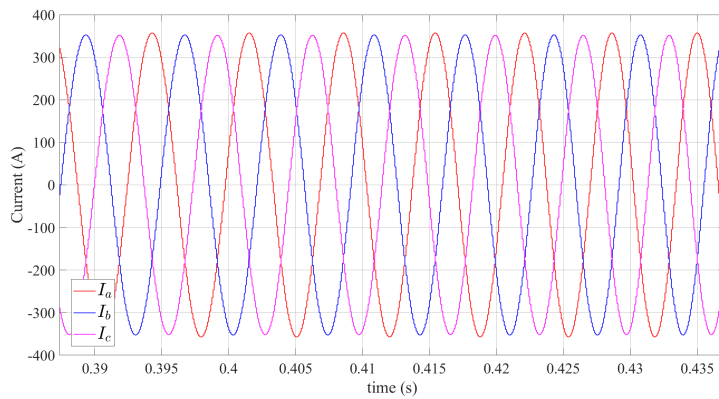
Figure 5.15: Currents unbalance simulation results.

As can be seen in Figure 5.16(a) both controls are able to follow the torque reference despite the error in the currents evaluation. Relevant errors are visible only for low mechanical speed. In general the performances of the two controls are comparable of when no error occurs.

In Figure 5.16(b) are shown the currents signals seen by the MCU. The I_a signal, as anticipated, is slightly greater than the other two.



(a) Torque profile



(b) Current signals seen by the MCU

Figure 5.16: Currents unbalance simulation results.

5.5.2 Open gate Fault

The second fault situation analyzed is the one related with the inverter fault. The idea is to simulate the failure of transmission of one of the gate commands. The simulation has been done considering that the upper switch of a phase of the inverter stop receiving a gate command at the instant 0.4 s.

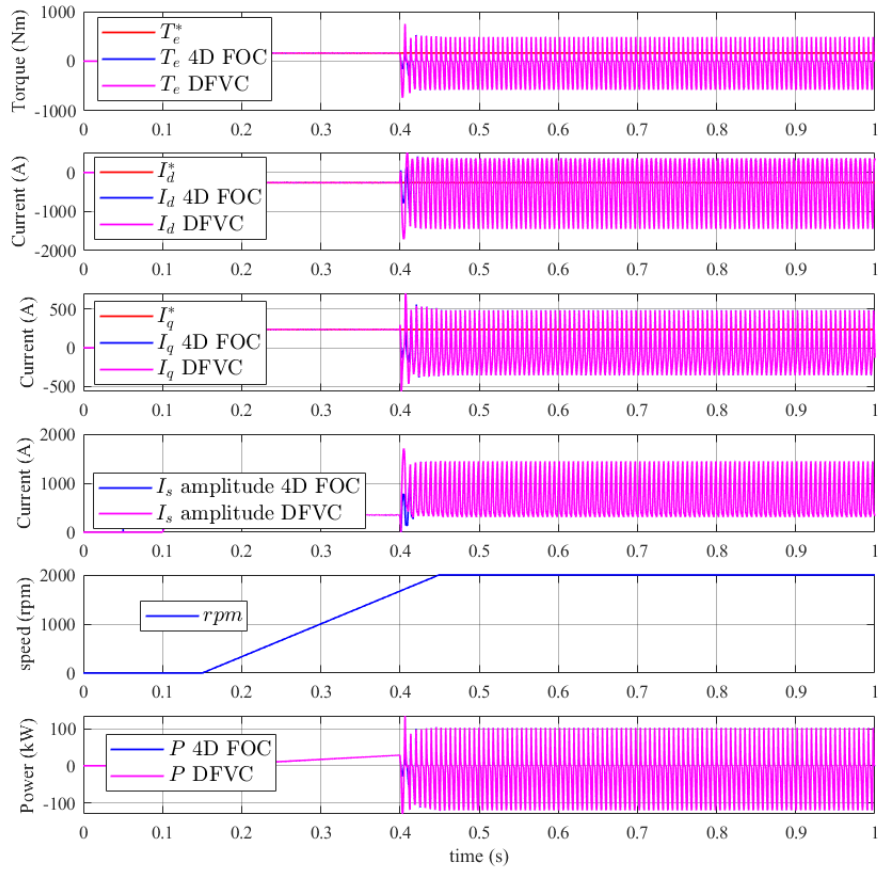


Figure 5.17: Open gate fault simulation results.

Figure 5.17 shows that both the 4D FOC and the DFVC completely lose the control of the e-Drive at the instant the gate command stop working. That happens because the current amplitude becomes uncontrolled and overcomes the protection limit. So the control goes in the ERROR state and then tries to restart working going in the RESET state and after in the DRIVE_INIT state but that doesn't result enough to regain control of the current, the state machine goes back to ERROR and restart this cycle that never ends.

The absence of a gate command results to be a critical error that the control is not able to overcome and so can be dangerous for the damaging of the e-Drive.

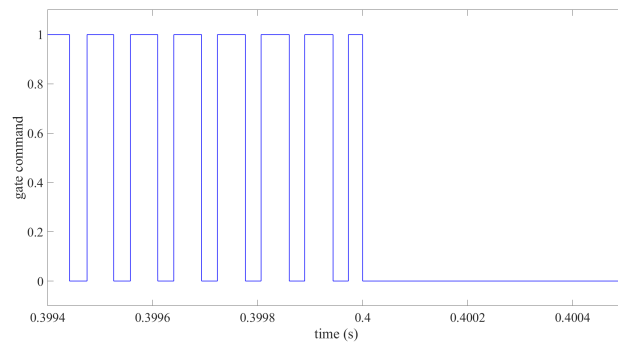


Figure 5.18: Gate signal behaviour.

Chapter 6

Conclusion

This thesis dealt with different problematics, all concerning the most efficient control of e-Drives for electrical vehicles. The electric traction system has been successfully modelled in the simulation environment Simulink. Existing blocks are employed to model the energy storage and the converter. On the other hand, a new circuit model for the electrical machine is introduced from the theoretical point of view and correctly modelled with a specific Simulink block. This motor modelling has great potentialities in the simulation environment thanks to its high adaptability and flexibility. Future developments could concern the implementation of other electrical machine dynamics such the losses aspect. Furthermore only comparison test with a non-circuital, discrete time average model in a simulation environment are done in the context of this thesis. The comparison and test with a real electric traction system is strictly necessary to give a solid validity to this simulation model.

A deep analysis of the state of art about torque control for e-Drives for electrical vehicles is conducted to allow a proper choice of the best technique to be implemented to follow the requirement proposed by Punch Torino in the research contract of which this thesis is part. DFVC is the solution proposed and developed by the PEIC department of Politecnico di Torino. My personal contribution stands in the realization of a valid alternative to DFVC that I found in the 4D FOC control scheme. The motor control is satisfactorily implemented in the C-language. It is tested in Simulink and PLECS environments, highlighting its feasibility and validity. Also peculiar characteristics are shown like the capability to overcome the issues due to machine electric parameters variation with temperature. The greatest drawback resides in the difficulties in the elaboration of the 4D LUTs. Nevertheless LUTs computation is an offline operation that guarantees a fast and efficient online response of the control.

In conclusion the whole system developed with the powertrain circuital model and the control represents a valid simulation environment and also a strong base for future development in the optic of Fault Tolerance thanks to the circuital characteristics of the e-Motor model generated. In this thesis the simple analysis of some faulty situation is reported, no control solutions able to overcome them are researched. The 4D FOC control scheme developed due to its simplicity, flexibility and reliability can be the starting point in this field.

Chapter 7

Bibliography

- [1] L. Zhong, M. F. Rahman, W. Y. Hu, and K. W. Lim, "*Analysis of Direct Torque Control in Permanent Magnet Synchronous Motor Drives*", IEEE Transactions on power electronics, VOL 12, No 3, May 1997.
- [2] Domenico Casadei, Giovanni Serra, Andrea Stefani, Angelo Tani, and Luca Zarri, "*DTC Drives for Wide Speed Range Applications Using a Robust Flux-Weakening Algorithm*", IEEE Transactions on power electronics, VOL 54, No 5, October 2007.
- [3] Yuttana Kumusuwan, Suttichai Premrudeepreechacharn, Hamid A. Toliyat, "*Modified direct torque control method for induction motor drives based on amplitude and angle control of stator flux*", Electric Power System Research 78(2008) 1712-1718.
- [4] Hafiz Asad Ali Awan, Seppo E. Saarakkala, Marko Hinkkanen, Zhanfeng Song, "*Optimal Torque Control of Synchronous Motor Drives: Plug-and-Play Method*", 2017 IEEE Energy Conversion Congress and Exposition (ECCE).
- [5] E. Trancho, E. Ibarra, C. Salazar, I. Lopez, A. Diaz de Guerenu, A. Pena, Tecnalia, "*IPMSM Torque Control Strategies based on LUTs and VCT feedback for Robust Control under Machine Parameter Variations*", IECON 2016 - 42nd Annual Conference of the IEEE Industrial Electronics Society.
- [6] Bon-Ho Bae, Nitin Patel, and Steven Schulz, Seung-Ki Sul, "*New Field Weakening Technique for High Saliency Interior Permanent, Magnet Motor* ", 38th IAS Annual Meeting on Conference Record of the Industry Applications Conference, 2003.
- [7] Sarayut Amornwongpeeti, Oleh Kiselychnyk, Jihong Wang, Nastaran Shatti, Nirav Shah, Michail Soumelidis, Nastaran Shatti, Nirav Shah, "*Adaptive Torque Control of IPMSM Motor Drives for Electric Vehicles*", 2017 IEEE 26th International Symposium on Industrial Electronics (ISIE).
- [8] E. Trancho, E. Ibarra, A. Arias, I. Kortabarria, J. Jurgens, L. Marengo, A. Fricassè, J. V. Gragger "*PM-Assisted Synchronous Reluctance Machine Flux Weakening Control for EV and HEV Applications*", IEEE Transactions on Industrial Electronics, VOL. 65, No.4, April 2018.
- [9] G. Pellegrino, R. Bojoi, P. Guglielmi, "*Unified Direct-Flux Vector Control for AC Motor Drives*", IEEE Transactions on Industry Applications Year: 2011 | Volume: 47.
- [10] Ehsan Dehghan-Azad, Shady Gadoue, David Atkinson, and Peter Barrass, "*Sensorless Torque-Controlled Induction Motor Drive for EV applications*", 2006 India International Conference on Power Electronics.

- [11] Aleksej Kiselev, Guillermo R. Catuogno, Alexander Kuznietsov, and Roberto Leidhold, "*Finite-Control-Set MPC for open-phase fault-tolerant control of PM synchronous motor drives*", IEEE Transactions on power electronics, VOL 67, No 6, June 2020.
- [12] Ahmed Aboelhassan, Waseem El Sayed, Ahmed Hebala, Michael Galea, Serhiy Bozhko, "*Fault Tolerant Control Strategy Based on Model Predictive Control and Unscented Kalman Filter for Permanent Magnet Synchronous Motor*", 2021 IEEE 16th Conference on Industrial Electronics and Applications (ICIEA).
- [13] Eric Armando, Paolo Guglielmi, Gianmario Pellegrino, Radu Bojoi, "*Flux Linkage Maps Identification of Synchronous AC Motors Under Controlled Thermal Conditions*", 2017 IEEE International Electric Machines and Drives Conference (IEMDC).
- [14] E. Armando, M. Pastorelli, K. Lang, R. Bojoi, "*Efficiency and Loss Mapping of AC Motors using Advanced Testing Tools*", 2016 XXII International Conference on Electrical Machines (ICEM).
- [15] Eric Armando, Paolo Guglielmi, Gianmario Pellegrino, Radu Bojoi, Michele Pastorelli, "*Experimental Identification of the Magnetic Model of Synchronous Machines*", IEEE Transactions on industry applications, VOL 49, No 5, September/October 2013.
- [16] Eric Armando, Paolo Guglielmi, Gianmario Pellegrino, Alfredo Vagati, Michele Pastorelli, "*Accurate Modeling and Performance Analysis of IPM-PMASR Motors*", IEEE Transactions on industry applications, VOL 45, No 1, January/February 2009.
- [17] E. Armando, P. Guglielmi, G. Pellegrino, R. Bojoi, S.G. Rosu, "*Self-Commissioning of Inverter Nonlinear Effects in AC Drives*", 2en IEEE Energycon Conference and Exhibition, 2012 / Advances in Energy Conversion Symp.
- [18] Eric Armando, Paolo Guglielmi, Gianmario Pellegrino, Radu Bojoi, "*Self-Commissioning Algorithm for Inverter Nonlinearity Compensation in Sensorless Induction Motor Drives*", IEEE Transactions on industry applications, VOL 46, No 4, July/August 2010.
- [19] Francesco Cupertino, Paolo Guglielmi, Gianmario Pellegrino, Radu Bojoi, "*Accurate Inverter Error Compensation and Related Self-Commissioning Scheme in Sensorless Induction Motor Drives*", IEEE Transactions on industry applications, VOL 46, No 5, September/October 2010.
- [20] Dong-Choon Lee, G-Myoung Lee, "*A Novel Overmodulation Technique for Space-Vector PWM Inverters*", IEEE Transactions on power electronics, VOL 13, No 6, November 1998.
- [21] Zammit Daniel, Spiteri Staines Cyril, Apap Maurice, "*Compensation Techniques for Non-Linearities in H-Bridge Inverters*", Elsevier Journal of Electrical System and Information Technology,10/01/2016.
- [22] Yinye Yang, Kamran Arshad-Ali, Joel Roelevel, Ali Emadi, "*State of Art Electrified Powertrains-Hybrid, Plug-in, and Electric Vehicles*", International Journal of Powertrains, VOL 5, No 1, 2016.
- [23] Matthew Liam De Klerk, Akshay Kumar Saha, "*A Comprehensive Review of Advanced Traction Motor Control Techniques Suitable for Electric Vehicle Applications*", IEEE Access, VOL 9, September 6 2021.
- [24] Paul Krause, Oleg Wasynczuk, Scott D. Sudhoff, Steven Pekarek, "*Analysis of Electric Machinery and Drive Systems*", Wiley-IEEE Press, 2013

- [25] Radu Bojoi, *Slides of "Electrical Technologies for eMobility"*, Mechatronic Engineering, Politecnico di Torino, Dipartimento di Energia "G.Ferraris", 2021
- [26] *Math Works Documentation*, <https://it.mathworks.com/help/physmod/simscape/ref/>

Appendix A

C-Functions

In the following, the ancillary C-functions required by 4D FOC scheme are reported.

SinCos

```
void SinCos (float *angle, Xsc *sincos_theta){
(*angle) = angle_normalization((*angle));
sincos_theta->sin = sin((*angle));
sincos_theta->cos = cos((*angle));
}
```

DirectClarke

```
void DirectClarke00 (Xabc *Abc, Xalphabeta *AlphaBeta) {
AlphaBeta->alpha = two_over_three * (Abc->a - sin30 * Abc->b - sin30 * Abc->c);
AlphaBeta->beta = two_over_three * (cos30 * Abc->b - cos30 * Abc->c);
}
```

Low pass filter

```
float low_pass_filter (float x_unfilt, float x_filt_old, float kf_lpf) {
float x_filt;
x_filt = (1.0 - kf_lpf) * x_filt_old + kf_lpf * x_unfilt;
return x_filt;
}
```

A.1 Interpolation of 2D LUT

- The inputs are: the memory index of the first element of the matrix storing the LUT (P), the actual value of variables from which the output depends (x, y), the steps and extremes of the inputs ($Dx, invDx, Dy, inDy, Xmin, Xmax, Ymin, Ymax$), and the number of the points along a line of the matrix ($Npointx$).
- The input value is saturated between the minimum and maximum values in both directions.
- The exact position (rx, ry) of the inputs value (x, y) is evaluated as distance from the origin of the matrix ($Xmin, Ymin$), that corresponds to the position pointed initially by the pointer.

Also the integer part of the distance (ix, iy) that are closer to lower coordinates of the point are obtained from the exact position.

The difference between the exact and integer positions is the deficit of the exact input values from the closer lower coordinates that exist in the matrix.

- The value of the pointer is updated to the lower coordinate of the closer existing point in the matrix. The square interpolation is performed here, between this point and the following, along x direction, obtaining V1.
- The value of the pointer is updated to the upper coordinate, incrementing the index of the number of element in each line (`Npointx`). The square interpolation is performed here, between this point and the following one, again along x direction, obtaining V2.
- Finally, the output of the function is the interpolation between the two interpolated values, that produce V.

The equivalent C-code is reported in the following.

```
float read_two_dim_lut(float *P, float x, float y, float Dx, float invDx,
float Dy, float invDy, float Xmax, float Xmin, float Ymax , float Ymin,
int Npointx) {

    // output
    float V;

    // temp variables
    float ix, iy;
    float rx, ry;
    float V1, V2;
    int delta;

    // inputs limitations
    if (x > Xmax)
        x = Xmax - 0.001 * Dx;
    if (x < Xmin)
        x = Xmin + 0.001 * Dx;
    if (y > Ymax)
        y = Ymax - 0.001 * Dy;
    if (y < Ymin)
        y = Ymin + 0.001 * Dy;

    // initial position
    rx = (x - Xmin) * invDx;
    ry = ((y - Ymin) * invDy) + 1;

    // int indexes
    ix = floor(rx);
    iy = floor(ry);

    // interpolation deficits
    rx = rx - ix;
    ry = ry - iy;

    // first point
    delta = ix + ((iy - 1) * Npointx);
    P = P + delta;

    // square interpolation
    V1 = *P + ((*P + 1) - *P) * rx;
    P = P + Npointx;
    V2 = *P + ((*P + 1) - *P) * rx;
}
```

```
// inperpolated value
V = V1 + ((V2 - V1) * ry);

// exit
return V;
}
```

A.2 Phase Locked Loop

The inputs of the functions are the sine and cosine of the input angle of interest. The function calculates the sine and cosine of the PLL angle evaluated at the previous step ($k-1$), that are compared with the ones in input. From the outer product the error is evaluated and given to a PI regulator that produces a speed as output. From the speed, the PLL angle is obtained and normalized between $[-180:180]$. The equivalent C-code is reported in the following.

```
void pll(Xscsc_theta, Xpll *pll_var){
SinCos(&(pll_var->theta), &sc_theta_pll);
pll_var->err =sc_theta.sin * sc_theta_pll.cos -sc_theta.cos * sc_theta_pll.sin;
pll_var->prop =pll_var->kp * pll_var->err;
pll_var->acc =pll_var->ki * pll_var->err;
pll_var->omega_filt +=pll_var->acc * Ts;
pll_var->omega_unfilt =pll_var->prop +pll_var->omega_filt;
pll_var->theta +=pll_var->omega_unfilt * Ts;
pll_var->theta =angle_normalization (pll_var->theta);
}
```